# Exploring stellar magnetic activities with Bayesian inference

**Kai Ikuta**

Department of Astronomy

Kyoto University

This dissertation is submitted for the degree of

*Doctor of Science*

December 2020

# Abstract

Starspots are apparent manifestations of stellar magnetic activity on the surface, and can be ubiquitously observed on various types of stars. For active young stars, cool stars (M, K, G, F-dwarfs), and RS CVn-type stars, starspots have been extensively studied through ground-based observations. With the advent of unprecedented precision and long-term photometry by the *Kepler* space telescope, photometric brightness modulations ascribed to spots have facilitated studies of starspot properties. Then, there are some components to elucidate stellar magnetic activities analogous to solar ones: the latitudinal spot distribution; the spot emergence and decay rates; and the stellar differential rotation. Starspot have been also investigated in association with flare properties. In particular, superflare properties on solar-type stars have been also unveiled by the statistical analysis of the *Kepler* data and the individual spectroscopic observations. Then, to decipher the stellar and spot properties from photometric brightness modulations ascribed to spots, light curve analyses and starspot modelings of the spotted stars have been employed. At that time, the light curve is constituted many parameters: especially, the number of spots can play an important role in measuring the emergence and decay rates.

Therefore, for the purpose of deducing stellar and spot properties from the light curves, we implement a computational code for starspot modeling. It is implemented with an adaptive parallel tempering (PT) algorithm and an importance sampling algorithm for parameter estimation and determining the number of spots as statistical model selection in the Bayesian framework. The PT algorithm enables to explore the multidimensional parameter space readily. First, to evaluate the performance of the code, we revisit synthetic light curves emulating *Kepler* data of spotted stars. As a result, stellar and spot parameters are uniquely deduced, and the number of spots is correctly determined. The spot emergence and decay rates can be estimated with error less than an order of magnitude, considering the difference of the number of

spots. Second, we conduct starspot modeling for *TESS* light curves of renowned flare M-dwarfs, AU Microscopii, YZ Canis Minoris, and EV Lacertae, which are concurrently performed spectroscopic observations. As a preliminary result, the spot latitudinal distributions are almost consistent with the results obtained by an other analysis of the photometry and by Zeeman Doppler Imaging techniques.

Our study enables to investigate stellar and spot properties in detail utilizing the sophisticated statistical technique and to approach how superflare stars have magnetic activities.

# Acknowledgements

# Table of contents

# List of figures

# List of tables

# Chapter 1

# General Introduction

The purpose of this thesis is to explore stellar magnetic activities of spotted stars by utilizing prevalent methods of Bayesian inference. First, Section 1.1 briefly describes fundamental sunspot and starspot properties associated with solar and stellar flares, and denotes methods of light curve inversions as starspot mapping. Second, Section 1.2 introduces a fundamental Bayesian framework, on which our studies in Section 2 and 3 are based. Lastly, Section 1.3 specifies the purpose of this thesis.

## 1.1 Spot as a trace of magnetic activities

### 1.1.1 Sunspot

The Sun have been observed as the only star visible with spatial resolutions. Large amounts of data have been collected since Galileo Galilei started to observe sunspots on the Sun with his telescope in the beginning of 17th century. Hale (1908) revealed there are magnetic fields in sunspots. Then, the sunspot is one of the observable manifestations to elucidate solar magnetic activities. The sunspot usually exists in an active region with strong magnetic fields on the Sun and is darker than the vicinity due to the suppressed convection by the magnetic fluxes: the typical temperatures of the sunspot and photosphere are 4000 K and 6000 K, respectively. The active region is a cross-section of emerged magnetic fluxes, which are transported from the deep convection zone by the dynamo mechanism (e.g., Parker 1955; Toriumi and Wang 2019). It typically takes hours to days for a sunspot to emerge, and weeks to months to decay. The typical size of a sunspot is up to 0.1% of the solar hemisphere, and

smaller sunspots more frequently appear than larger ones. Figure 1.1 exhibits example images of the Sun (Toriumi and Wang 2019). In the southern hemisphere, there is a large sunspot group (top left), in which the magnetic field intensely concentrates (top middle), and the bright loop structure can be clearly observed in EUV image (top right). In addition, active regions are composed of a number of magnetic elements with opposite polarities (bottoms). This fact suggests the magnetic fields of sunspots are connected from the internal convection zone.
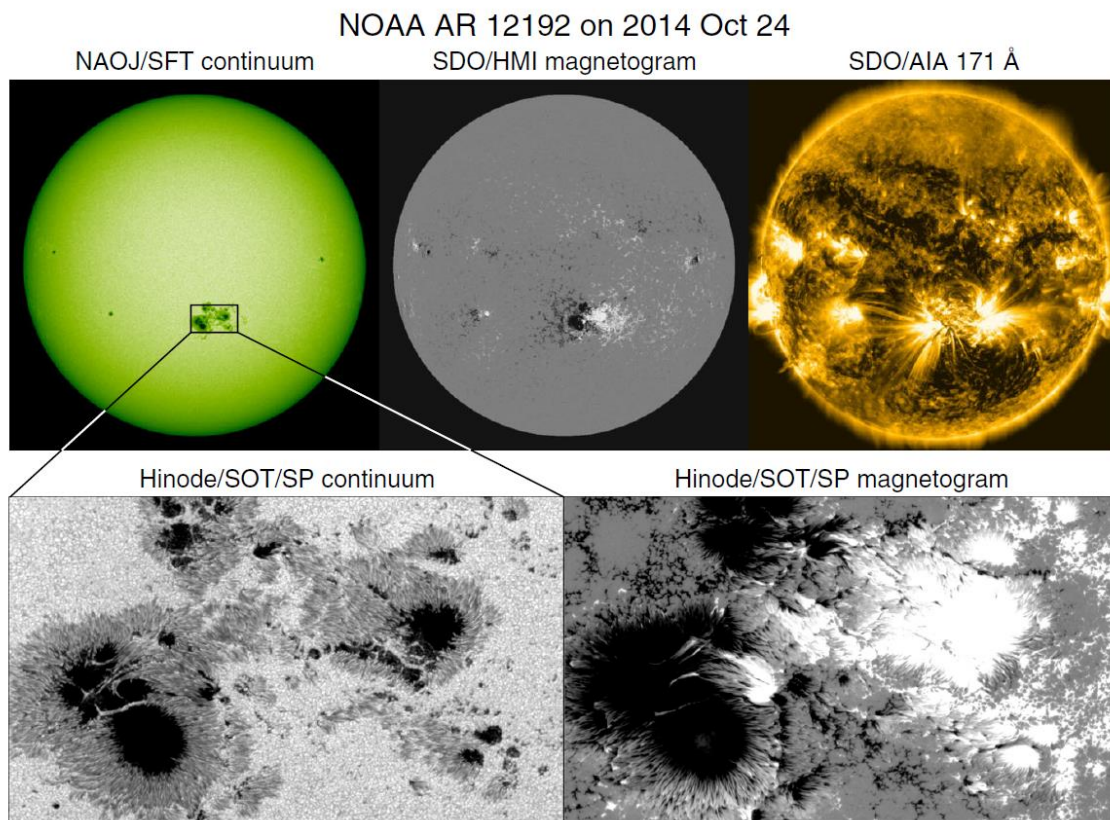


Figure 1.1: Example images of huge flare-productive AR NOAA 12192 (Active Region numbered 12192 by National Oceanic and Atmospheric Administration) appeared in October 2014 (Toriumi and Wang 2019): (top left) continuum image shows a large sunspot group in the southern hemisphere (the Solar Flare Telescope in National Astronomical Observatory of Japan); (top middle) magnetrogram shows strongly concentrated magnetic field (Helioseismic and Magnetic Imager in Solar Dynamics Observatory, SDO); (top right) EUV image shows the bright loop structure (Atmospheric Imaging Assembly in SDO); and (bottoms) active regions are composed of a number of magnetic elements with opposite polarities (Solar Optical Telescopes of Hinode).

The number of sunspots varies with the 11-year solar activity cycle (for a review, Hathaway 2015). The spots appear at higher latitudes up to 40°, and the latitude drifts lower to the equator throughout the cycle (Spörer's law: Carrington 1858). The behavior is illustrated in the top panel of Figure 1.2 by the Maunder butterfly diagram. In each bipolar active region, the preceding spot tends to appear closer to the equator than the following spot (Joy's rule: Hale et al. 1919). Moreover, for each cycle, the bipolar active regions are aligned in the east to west with opposite preceding magnetic polarities on the opposite hemispheres (Hale's polarity rule). The bottom panel of Figure 1.2 also illustrates that the polarities of the preceding spots alternate between consecutive cycles (Hale-Nicholson rule: Hale and Nicholson 1925).
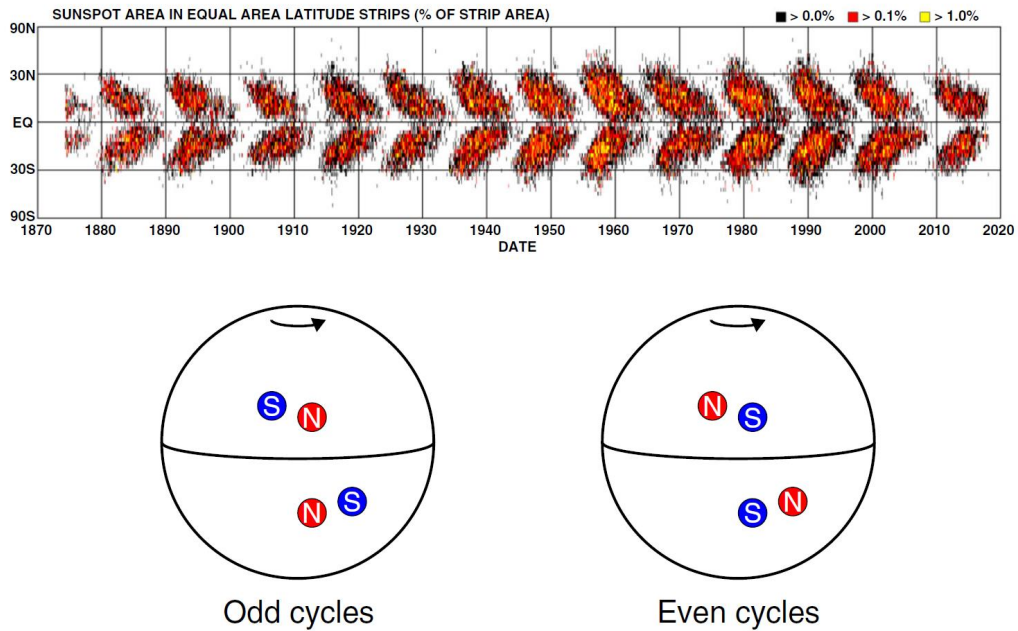


Figure 1.2: (top) The solar butterfly diagram depicts the total spot area as a function of time and latitude. In each cycle, the latitudes of active regions drift to the equator (Spörer's law). (bottom) The bipolar active regions are aligned in the east to west with opposite preceding magnetic polarities on the opposite hemispheres, and the polarities of the preceding spots alternate between consecutive cycles (Hale-Nicholson rule).

## Correlation with solar flares

The sunspots are closely related to solar flares in terms of the solar magnetic activities. Solar flares are the most energetic explosions in the solar atmosphere and
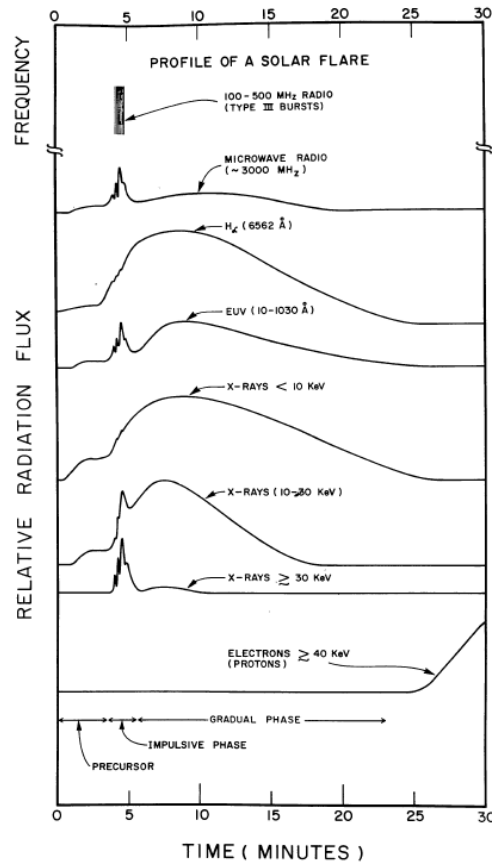
Figure 1.3: A schematic representation of a solar flare observed in the multi-wavelength and particle radiation (Kane 1974).

caused by intense releases of magnetic energy near sunspots (for reviews, Shibata and Magara 2011; Toriumi and Wang 2019). The first solar flare was observed as a white light flare by Carrington (1859), and the Carrington Flare is renowned as one of the most energetic flares (the total energy is $\sim 10^{32}$ erg). Solar flares have been observed in multi-wavelength from radio to gamma-ray, which emanate from the chromosphere to corona (Figure 1.3 from Kane 1974; Benz 2017, for a review). The typical energy and duration are $10^{29\text{-}32}$ erg and $10^{2\text{-}4}$ second, respectively. The flare activities are closely related to the size and structure (complexity): larger or more complicated sunspots are required to cause larger flares (Figure 1.4; Toriumi and Wang 2019).
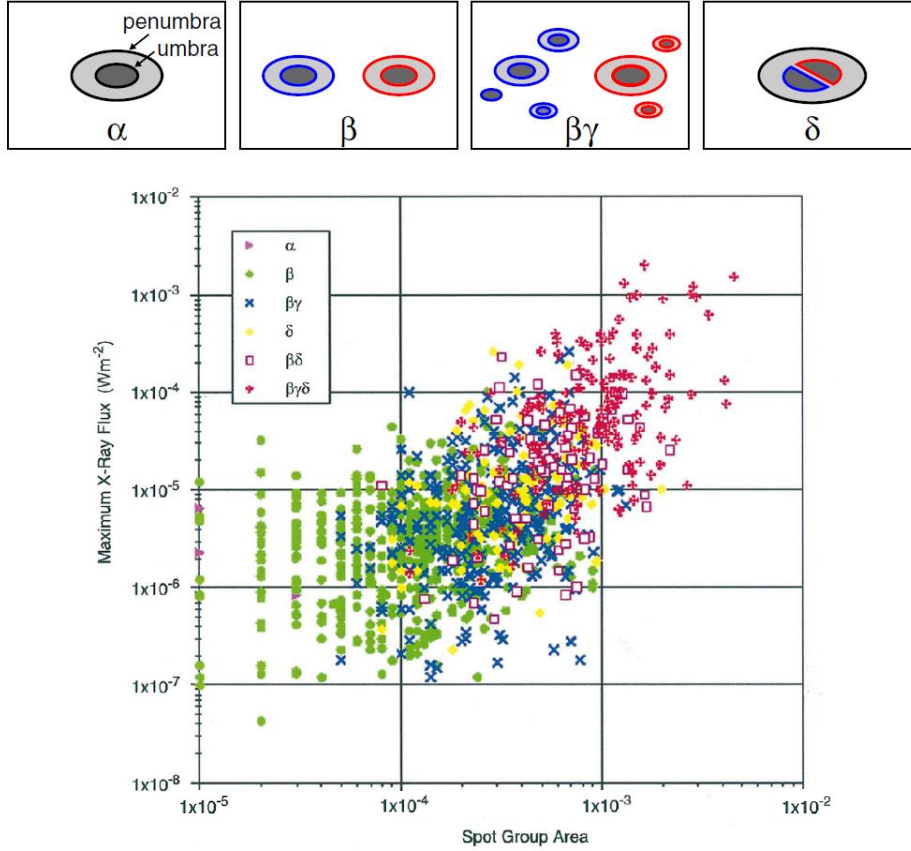
Figure 1.4: (top) Sample diagrams of the Mount Wilson Classification (Toriumi and Wang 2019). The more complicated sunspots are depicted in the more right. (bottom) The peak GOES soft X-ray flux as a function of maximum sunspot area (Sammis et al. 2000). The horizontal axis represents the fraction of the solar hemisphere, and the scale are modified from the original value in Sammis et al. (2000).

### 1.1.2 Starspot

Just as the solar magnetic activities, the phenomena of stellar ones, such as starspots on the stellar surface (for reviews, Berdyugina 2005; Strassmeier 2009) and stellar flares, have been observed with higher magnetic activities than the solar ones (for a review, Güdel 2007). The strong magnetic fields are thought to be generated by the internal dynamo mechanism (for a review, Brun and Browning 2017). In particular, the starspots are apparent manifestations of the stellar magnetic activity on the stellar surface and can be ubiquitously observed on various types of stars for active young stars, cool stars (M, G, K, F-dwarfs), and RS CVn-type stars. For instance, Figure 1.5 depicts a comparison of the Sun and EK Draconis (HD 129333) as a young solar-type

star (G-dwarf) and the internal magnetic fields reproduced with a mean-field dynamo simulation (see Strassmeier 2009, for details). It is suggested that a large spot on EK Dra locates at higher latitudes than solar one. This result is based on Doppler Imaging technique, which reproduces the spot distribution on the surface by spectroscopic observations (e.g., Strassmeier 1999). In addition, Zeeman Doppler Imaging technique have enabled to map the polarity of magnetic fields on the surface by polarimetric observations (e.g., Morin et al. 2008). These spectroscopic results have show different pictures of spots from that of the Sun, such as long-lived and large polar spots: the lifetime and size are thought to be up to 10 yr and more than 10 % of the photosphere, respectively (Figure 1.6; Strassmeier 1999).
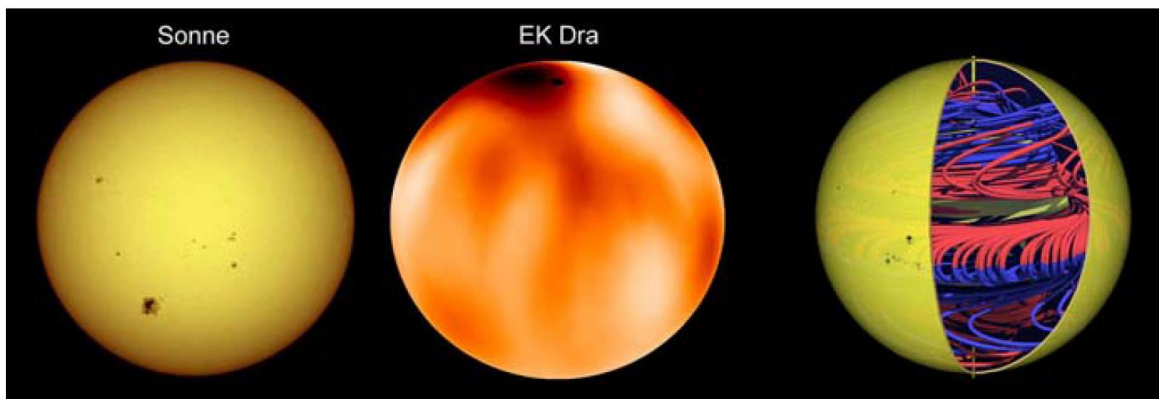


Figure 1.5: (left and middle) A comparizon of the Sun and EK Draconis (HD 129333), a young solar-type star with age of approximately 100 Myr and a rotation period ten times faster than the current Sun, reproduced with a result of Doppler Imaging (Strassmeier and Rice 1998). It is shown that large spots on EK Dra locate at higher latitudes than solar ones (single black dot indicates the position of the pole of the rotation axis). (right) Dipole-like magnetic fields are produced with a boundary-layer mean-field dynamo simulation. Individual flux tubes may reach the stellar surface and emerge as bipolar spot groups.

Heretofore, the starspots have been also extensively studied through ground-based observations since spots modulates the photometric brightness along with the stellar rotations (e.g., Strassmeier et al. 1994; Henry et al. 1995). With the advent of unprecedented precision and long-term photometry by the *CoRoT* (*Convection, Rotation and planetary Transits*) satellite (Auvergne et al. 2009) and *Kepler* space telescope (Koch et al. 2010), photometric brightness modulations ascribed to spots have facilitated long-term and statistical studies of stellar properties (e.g., Basri et al. 2010). The
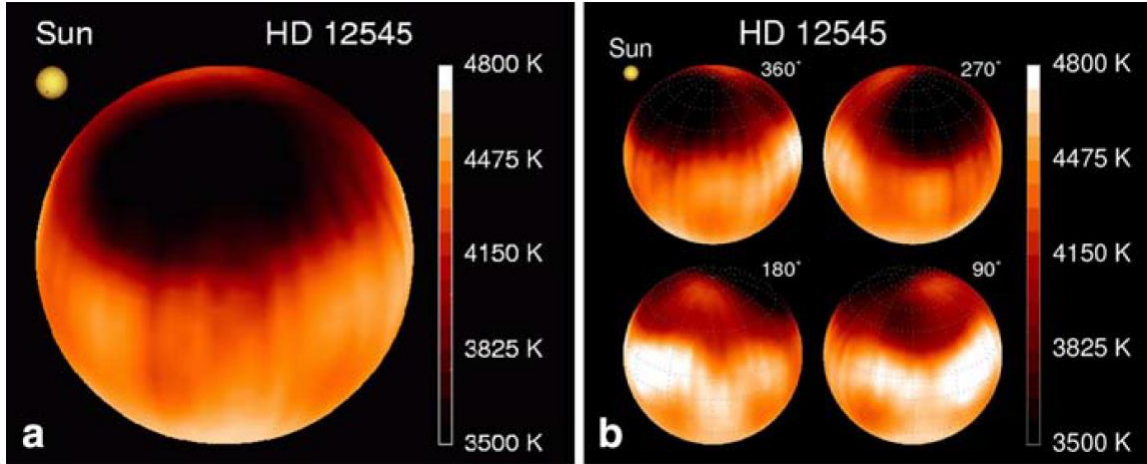
Figure 1.6: (a) The image of a large starspot near the pole of a active K-type giant star, XX Tri (HD12545), reproduced with the result of Doppler Imaging as a contour of the surface temperature (Strassmeier 1999). The spot is approximately $10^4$ times larger than the sunspot in Figure 1.5, and the temperature of the spot is approximately 1300 K cooler than that of the photosphere. (b) The phase change of the spot location with time.

modulations allow us to measure the rotation period of many main-sequence stars (McQuillan et al. 2014) and the stellar differential rotation (e.g., Reinhold et al. 2013; Arkhypov et al. 2018). Such photometric modulations are also associated with the indices of stellar magnetic activities, comparing those of the Sun (e.g., Basri et al. 2013; Basri 2018; Basri and Nguyen 2018). In addition, multiple transiting exoplanet occultations enable to investigate the latitudinal and size distributions of spots (Morris et al. 2017) and to measure temporal evolutions of spots (Davenport 2015; Namekata et al. 2020), which are also able to be measured by the rotational brightness modulations (e.g, Giles et al. 2017; Namekata et al. 2019). Namekata et al. (2020) compares the results independently obtained by the exoplanet occultations, the rotational brightness modulations represented as local mimima, and the light curve modeling based on Section 2. It is significant to measure the temporal evolutions of spots because of the relation with the following issues: solar flares tend to be driven by emerging sunspots (Toriumi and Wang 2019), and superflares could occur on solar-type stars (Maehara

et al. 2012) because large spots can cause superflares (Shibata et al. 2013); measuring magnetic diffusion of the convection zone reflects to constrain theoretical stellar dynamo simulation (e.g., Bradshaw and Hartigan 2014).

Moreover, Namekata et al. (2020) found that there are from four to six spots on the surface of the exoplanet-hosting solar-type star Kepler-17 using the transiting exoplanet occultation (the longitudinal resolution $\sim 20°$), whereas two local minima appear during an equatorial rotation. They showed that the light curve modulations are actually the superposition of many spots, and the emergence and decay rates estimated from the rotational modulations are found to be somewhat underestimated by the effect of the superposition. They showed the number of spots on the stellar surface can play an important role in measuring the emergence and decay rates. Figure 1.7 exhibits a comparison of the results obtained by the exoplanet occultations and the local minima and represents the different numbers of spots on the surface in the methods. Several studies have also investigated how the number of spots is related to light curves (e.g., Eker 1994; Notsu et al. 2013b; Morris et al. 2017; Basri and Nguyen 2018; Basri 2018). Namekata et al. (2020) also showed the emergence and decay rates of starspots can be explained by an extension of those of sunspots.

## Correlation with stellar flares

Stellar flares, analogous to the solar flares, are observed in multi-wavelength on other active stars, such as young stars (e.g., Benz and Güdel 2010), M-dwarfs (e.g., Osten et al. 2016), and RS-CVn stars (e.g., Walter and Bowyer 1981). In particular, superflares are also observed with the total energy of $10^{33\text{-}38}$ erg larger than largest solar one ($\sim 10^{32}$ erg) and the duration of a few hours much longer than typical solar one: Figure 1.8 exhibits the typical light curve of a superflare on an active M-dwarf AD Leonis (Gliese 388) (Hawley and Pettersen 1991). These stars rotate fast approximately with the period of a few days and frequently exhibit flares due to their high magnetic activities.

Superflares are also reported on solar-type stars with magnetic activities comparable that of the Sun, and they rotate slowly with the period of longer than 10 days (Schaefer et al. 2000). *Kepler* also facilitated statistical studies of superflares on the solar-type stars because a number of main sequence stars ($\sim 160000$) were observed with unprecedented precision and long-term photometry (e.g., Basri et al. 2010). Then,
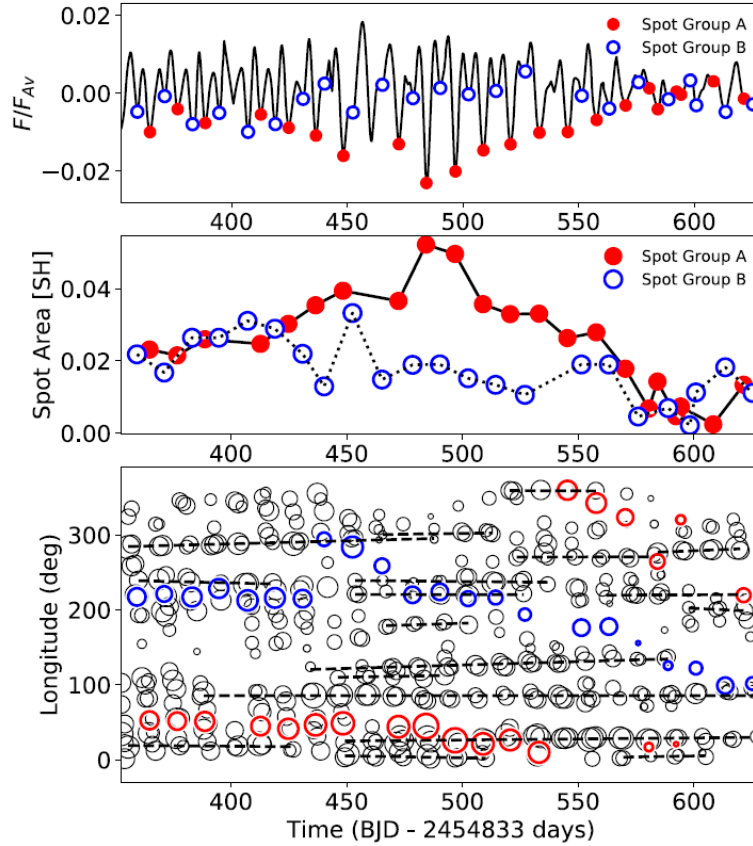
Figure 1.7: (top) The normalized light curve (relative flux) of a solar-type star Kepler-17, which hosts a exoplanet,in *Kepler* quarter 4-6 (black) and the local minima in the light curve identified as each of spot group (red and blue). (middle) The temporal variations of the spot area. (bottom) Comparison of the spot longitudinal distributions obtained by the transiting exoplanet occultation (black) and the local minima (red and blue).

many superflares are reported on many solar-type stars, including a few Sun-like stars (analogous to the Sun on the temperature from 5600 to 6000 K and rotation period over 20 days), and also on F, K, M-dwarfs and subgiants (Figure 1.9 from Maehara et al. 2012, 2017; Shibayama et al. 2013; Karoff et al. 2016; Notsu et al. 2019; Okamoto et al. 2020). The total energy of the superflares on the solar-type stars ranges from $10^{33}$ (the detection limit of flares) to $10^{36}$ erg. Similar to solar flares, the superflares are also caused by starspots modulating the photometry (Notsu et al. 2013b; Maehara et al. 2017), and this fact is confirmed by the follow-up spectroscopic observations (Notsu et al. 2013a, 2015a,b, 2019; Nogami et al. 2014). Figure 1.10 represents the
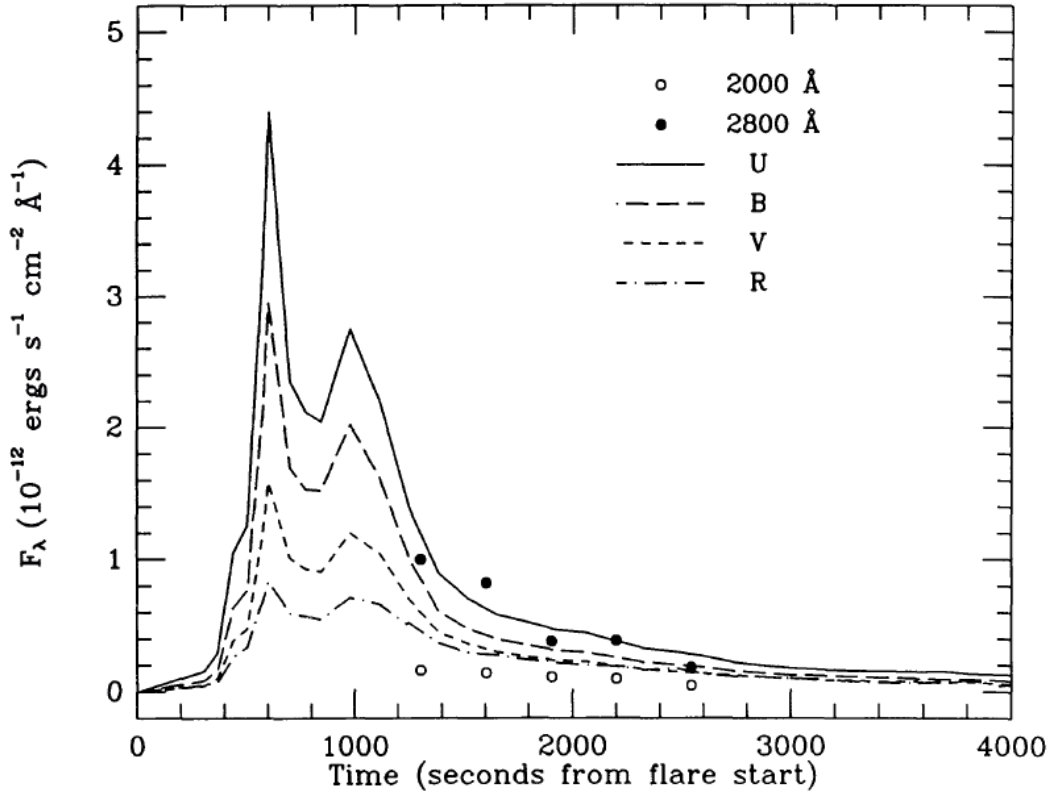
Figure 1.8: The light curve of a superflare on an active M-dwarf AD Leonis (Hawley and Pettersen 1991). The superflare continued for more than 4 hr. The continuum flux are measured in two ultraviolet wavelengths and the monochromatic $U$, $B$, $V$, and $R$.

relation between the flare energy and spot area (Okamoto et al. 2020). Therefore, it is significant to investigate how starspots on the superflare stars are.

### 1.1.3 Light curve inversion as starspot mapping

Light curve inversion or starspot mapping (hereinafter, referred to as starspot modeling) have phenomenologically been employed to decipher the distribution of the surface properties that account for changes of a photometry. In general, these technique are divided into two categories of surface integration technique and analytical model technique. The surface integration divides the stellar surface into a pixel grid and integrates over the contributions of all surface elements (e.g., Savanov and Strassmeier 2008) by means like the maximum entropy method (Lanza et al. 2010). The analytical model utilizes equations to calculate the loss of light ascribed to spots on the stellar
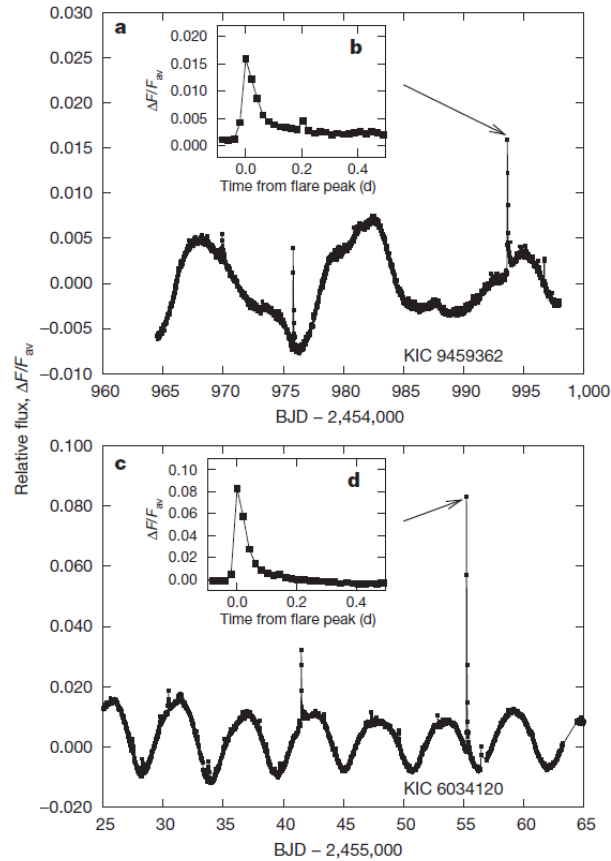
Figure 1.9: Light curves of superflares on two solar-type stars (Maehara et al. 2012): (a) The light curve of a superflare on KIC9459362 with the duration of 3.9 hr and total energy of $5.6 \times 10^{34}$ erg; (b) Enlarged light curve of the superflare in Figure (a); (c) Same as (a) but for KIC6034120 with those of 5.4 h and $3.0 \times 10^{35}$ erg; and (d) Enlarged light curve of the superflare in Figure (c).
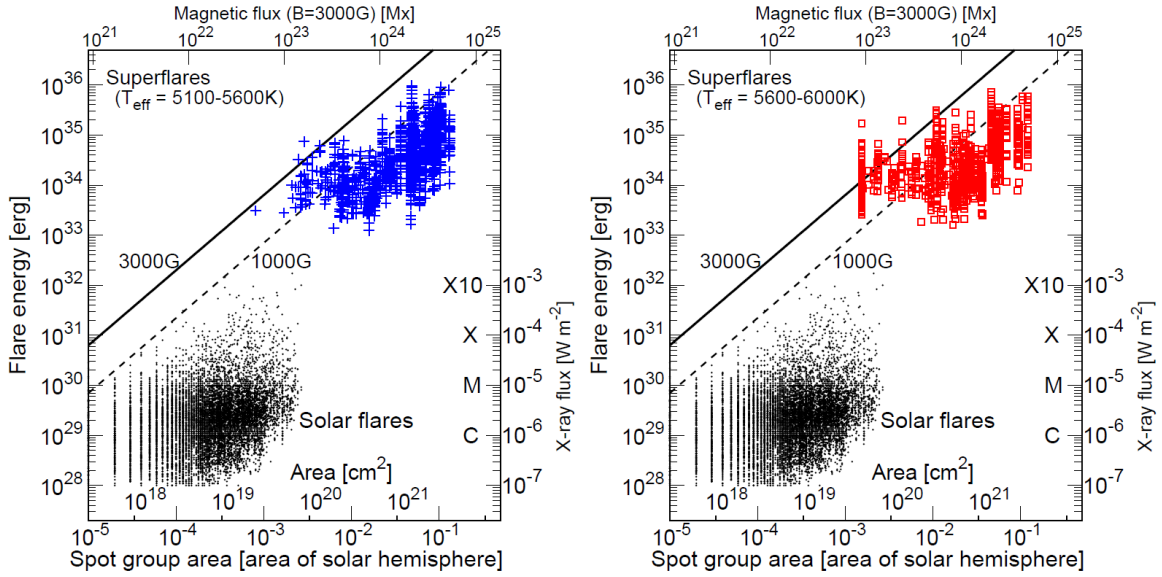
Figure 1.10: Flare energy versus spot area for solar flares and stellar superflares (Okamoto et al. 2020). The superflares are detected in all the data of *Kepler* prime mission ( ∼ 1500 days from 2009 to 2013). Left and right panels represent the superflares on solar-type stars with the effective temperature of 5100-5600 K and 5600-6000 K, respectively. Each flare energy is calculated from the photometric brightness of the flare under an assumption of black-body radiation (e.g., Shibayama et al. 2013). Each spot area is deduced from a function of the amplitude of the modulation, spot temperature (from a formula of stellar temperature Maehara et al. 2017), stellar radius, and the stellar temperature (from *Gaia* Data Release 2; Berger et al. 2018).The diagonal line represent the upper limit of flare energy, assumed the value of the magnetic flux (e.g., Shibayama et al. 2013).

surface (e.g., Strassmeier and Bopp 1992; Mosser et al. 2009), especially on the basis of Bayesian inference (Croll 2006; Croll et al. 2006; Walker et al. 2007; Frasca et al. 2011; Lanza et al. 2014; Almenara et al. 2018), which is introduced in Section 1.2. As denoted in Walkowicz et al. (2013), the analytical model has an advantage over the surface integration in that the results from it are sensitive to the resolution of the modeled star. The surface integration is capable of modeling spots with any shape while the analytical model typically require the spot shape to be simple, such as circular spots.

The analytic model also typically have fewer parameters, whereas more complex model as the surface integration tend to have many parameters. Therefore, although the surface integration can attain to be fitted across an entire light curve in better

than the analytic model, in some sense the inherent degeneracies and uncertainties are hidden within the number of parameters available to adjust the model of the surface integration. The analytic model has a particular benefit for the exploration of parameter degeneracies presented in this thesis in that certain parameters are well defined in the analytic model. However, it is difficult to use the surface integration to explore the relative effects of any of these parameters individually because it is not so well defined in the case of a continuous surface distribution.

The starspot modeling are complementary to spectroscopic mapping techniques, such as the Zeeman Doppler Imaging, which yields a spectroscopic constraint on the stellar inclination unobtainable only from the photometry. Althogh the Zeeman Doppler Imaging is only suited to rapidly rotating stars for which the magnetic field is strong enough to produce a detectable circular polarization signal (e.g., Morin et al. 2008), the starspot modeling can be effective to slowly rotating stars, including Sun-like stars (the rotation period is longer than 10 days), only if sufficient long-term data (a few stellar rotations) obtained by *Kepler* and *Transiting Exoplanet Survey Satellite* (*TESS*). As the Zeeman Doppler Imaging is effectively incentive to cool spots, due to the polarization signal being dominated by bright magnetic features (faculae and plage), we note that the mapping by Zeeman Doppler Imaging are not directly comparable to the result from the starspot modeling.

## 1.2  Bayesian inference

Our study is based on Bayesian inference for inverse problem to deduce stellar and spot properties. In this Section, we consistently elaborate Bayesian approaches mainly described in the instructive book by Gregory (2005b). Bayesian probability is the quantitative measure of our state of knowledge defined to satisfy axioms of the probability theory. Such a probability may not be the same everyone, and hence is some times called subjective probability. The advantage to adopt such a definition of probability extends the idea of probability beyond the frequentist sense.

### 1.2.1  Bayes' theorem

Followed by the definitions of a joint probability of $X$ and $Y$ as

$$p(X,Y) = p(X|Y)p(Y) = p(Y|X)p(X), \tag{1.1}$$

Bayes' theorem under a prior information $Z$ asserts

$$p(X|Y,Z) = \frac{p(Y|X,Z)p(X|Z)}{p(Y|Z)}. \tag{1.2}$$

Marginalizing both sides of $X$, the numerator as a normalization constant denotes

$$p(Y|Z) = \int p(Y|X,Z)p(X|Z)\,dX. \tag{1.3}$$

In particular, given $Y$ is data $\mathcal{D}$, $X$ is an explanatory parameter $\theta$ under a certain assumed model (hypothesis such as how many parameters $\theta$ there are) $M$ replaced for $Z$, The Bayes' theorem is deformed to

$$p(\theta|\mathcal{D},M) = \frac{p(\mathcal{D}|\theta,M)p(\theta|M)}{p(\mathcal{D}|M)}, \tag{1.4}$$

where

$$p(\mathcal{D}|M) = \int p(\mathcal{D}|\theta,M)p(\theta|M)\,d\theta. \tag{1.5}$$

Then, each term of the probability in Equation 1.4 and 1.5 implies as follows:

$p(\theta|\mathcal{D},M)$: Posterior distribution

The probability of parameter $\theta$ after data are updated to the prior knowledge. Shortly, Bayesian inference is procedure of how information from the data into $p(\theta|M)$ to obtain the posterior are incorporated.

$p(\theta|M)$ : Prior distribution

The probability of parameter $\theta$ evaluated by only prior knowledge. That represents our state of knowledge before data are obtained.

$p(\mathcal{D}|\theta, M)$ : Likelihood function

The probability of data $\mathcal{D}$ under parameter $\theta$.

$p(\mathcal{D}|M)$ : Model evidence (Marginalized likelihood)

Normalization constant evaluated as marginalized likelihood with $\theta$. This value is to be used for model selection elaborated in Section 1.2.3.

### 1.2.2    Parameter estimation: Markov Chain Monte Carlo (MCMC)

In astronomical context, we need to estimate values of parameters $\theta$ assuming a certain model $M$. In this case, all the normalization constants can be neglected, as long as they do not depend on the parameter to be evaluated. However, integration of parameters $\theta$ becomes intractable in multidimensional case. Thereby, we give an introduction to Markov Chain Monte Carlo (MCMC) algorithm (Foreman-Mackey et al. 2013; Sharma 2017; Hogg and Foreman-Mackey 2018), that is one of approximating methods to execute parameter estimation. We intend to obtain posterior for model parameters $p(\theta|\mathcal{D})$. In MCMC algorithm, we use a random sample to generate a Markov chain (a sample only depends on the previous one) in the parameter space. Reiterative samples $\theta$ in the chain follow posterior, if they are generated by formulated algorithm below.

### Metropolis-Hastings algorithm

The chain of samples with required property can be obtained by the following procedures, namely Metropolis-Hastings algorithm (Metropolis et al. 1953; Hastings 1970). We generate the sample $\theta_{i+1}$ from the previous sample $\theta_i$ in two steps:

1. Candidate sample $\theta_c$ for $\theta_{i+1}$ is randomly proposed with appropriate probability distribution namely proposal distribution $q(\theta_c; \theta_i)$. If symmetric distribution as $q(\theta_c; \theta_i) = q(\theta_i; \theta_c)$ is selected, this algorithm reduces to simple Metropolis algorithm.

2. Proposed sample is accepted with a probability of $r$ : $\theta_{i+1}$ updates $\theta_c$ if accepted, or retain $\theta_i$ if not. Acceptance probability $r$ is formulated as

$$r(\theta_c, \theta_i) = \min[1, \frac{p(\theta_c|\mathcal{D})q(\theta_i; \theta_c)}{p(\theta_i|\mathcal{D})q(\theta_c; \theta_i)}] = \min[1, \frac{p(\mathcal{D}|\theta_c)p(\theta_c)q(\theta_i; \theta_c)}{p(\mathcal{D}|\theta_i)p(\theta_i)q(\theta_c; \theta_i)}], \quad (1.6)$$

where the last equality is followed by equation (1.2) as Bayes' theorem.

We note that remarkable advantage of Metropolis-Hastings algorithm is that posterior distribution for parameter $\theta$ can be obtained without computing integration of equation (1.4) as normalization constant.

## Remarks

Markov chain generated by Metropolis-Hastings algorithm requires the following three properties to converge to a stationary distribution $\pi(\theta)$: (i) Irreducible, the chain can eventually reach any state of non-zero probability from any starting point; (ii) Aperiodic; (iii) Positive recurrent, stationary distribution $\pi(\theta)$ exists such that if initial value $\theta_0$ is generated from $\pi(\theta)$, then all subsequent iterative samples will also follow $\pi(\theta)$. The chain generated by Metropolis-Hastings algorithm satisfies the third property, and converges to the stationary distribution which is actually equivalent to posterior distribution. Equation (1.6) derives from the detailed balance equation:

$$p(\theta_i|\mathcal{D})p_{\text{tr}}(\theta_{i+1}|\theta_i) = p(\theta_i|\mathcal{D})q(\theta_{i+1}; \theta_i)r(\theta_{i+1}, \theta_i) \quad (1.7)$$

$$= \min[p(\theta_i|\mathcal{D})q(\theta_{i+1}; \theta_i), p(\theta_{i+1}|\mathcal{D})q(\theta_i; \theta_{i+1})] \quad (1.8)$$

$$= p(\theta_{i+1}|\mathcal{D})q(\theta_i; \theta_{i+1})r(\theta_i, \theta_{i+1}) \quad (1.9)$$

$$= p(\theta_{i+1}|\mathcal{D})p_{\text{tr}}(\theta_i|\theta_{i+1}), \quad (1.10)$$

where $p_{\text{tr}}(\theta_{i+1}|\theta_i)$ denotes the transition probability from $\theta_i$ to $\theta_{i+1}$, being equivalent to a product of proposal distribution $q(\theta_{i+1}; \theta_i)$ and acceptance probability $r(\theta_{i+1}, \theta_i)$.

Marginalizing both sides over $\theta_i$, the posterior distribution of $\theta_{i+1}$ is obtained:

$$\int p(\theta_i|\mathcal{D})p_{\text{tr}}(\theta_{i+1}|\theta_i)d\theta_i = p(\theta_{i+1}|\mathcal{D})\int p_{\text{tr}}(\theta_i|\theta_{i+1})d\theta_i = p(\theta_{i+1}|\mathcal{D}) \tag{1.11}$$

This implies that if $\theta_i$ is sampled from posterior distribution $p(\theta|\mathcal{D})$, $\theta_{i+1}$ also follows it. In other words, $p(\theta|\mathcal{D})$ is namely stationary distribution of the chain.

## Convergence diagnostics

The number of iterations on MCMC is determined by whether MCMC converges. For the purpose of MCMC convergence check, we briefly introduce convergence diagnostics based on Gelman and Rubin (1992) and Brooks and Gelman (1998). $n$ is the number of iterations, and $m$ is the number of chains.

$$\text{Within-chain variance}: \ W = \frac{1}{m}\Sigma_{j=1}^m \frac{1}{n-1}\Sigma_{i=1}^n(\theta_{i,j} - \overline{\theta}_j)^2 \equiv \frac{1}{m}\Sigma_{j=1}^m W_j \tag{1.12}$$

$$\text{Between-chain variance}: \ B = \frac{1}{m-1}\Sigma_{j=1}^m(\overline{\theta}_j - \overline{\theta})^2, \ \ \overline{\theta} \equiv \frac{1}{m}\Sigma_{j=1}^m\overline{\theta}_j \tag{1.13}$$

$$\text{Total variance}: \ V = \frac{n-1}{n}W + \frac{m+1}{m}B \tag{1.14}$$

$$\hat{R}^2 = \frac{V}{W} = \frac{n-1}{n} + \frac{m+1}{m}\frac{B}{W} \tag{1.15}$$

When $\hat{R}^2 < 1.1$, MCMC adequately converged. During the iterations, Mean and Variance are sequentially updated as

$$\overline{\theta_j}^{(n)} = \overline{\theta_j}^{(n-1)} + \frac{1}{n}(\theta_{n,j} - \overline{\theta_j}^{(n-1)}) \tag{1.16}$$

$$W_j^{(n)} = \frac{n-2}{n-1}W_j^{(n-1)} + \frac{1}{n}(\theta_{n,j} - \overline{\theta_j}^{(n-1)})^2 \tag{1.17}$$

## 1.2.3   Model selection

The purpose of model selection is to determine the best model that describes observed data (see Kass and Raftery 1995, for details). In Bayesian inference, this is enabled by computing quantitative measure of validity for each model. Here, the

probability that a certain model $M_i$ is correct given data $\mathcal{D}$ is needed to be evaluated:

$$p(M_i|\mathcal{D}) = \frac{p(\mathcal{D}|M_i)p(M_i)}{p(\mathcal{D})}, \tag{1.18}$$

where model evidence $p(\mathcal{D}|M_i)$ is given by integrating shown in equation 1.4. Competing models are usually compared as follows. The plausibility of the model $i$ relative to the model $j$ is often evaluated by odds ratio:

$$\mathcal{O}_{i,j} = \frac{p(M_i|\mathcal{D})}{p(M_j|\mathcal{D})} = \frac{p(\mathcal{D}|M_i)}{p(\mathcal{D}|M_j)}\frac{p(M_i)}{p(M_j)}. \tag{1.19}$$

We note that this ratio can be computed without the normalization $p(\mathcal{D})$. In particular, if the models $M_i$ and $M_j$ are equally plausible, odds ratios reduces to the ratio of model evidences, namely Bayes factor.

$$\mathcal{B}_{i,j} = \frac{p(\mathcal{D}|M_i)}{p(\mathcal{D}|M_j)} = \frac{\mathcal{Z}_i}{\mathcal{Z}_j}. \tag{1.20}$$

## 1.3   Purpose of this thesis

In the past decade, *Kepler* space telescope facilitated long-term and statistical studies of stellar magnetic activities thanks to the unprecedented precision and long-term photometry. Then, starspot properties have been investigated as a signature of the stellar magnetic activities and are associated with flare properties. In particular, superflare properties on solar-type stars have been unveiled by the statistical analysis of the *Kepler* data and the individual spectroscopic observations. It is also indispensable for the superflare stars to delve into the spot properties. Therefore, the purpose of this thesis is to approach the following problems by an advanced light curve modeling (starspot modeling):

(i)   How spots distribute on the surface of superflare stars?

(ii)   How long does a spot spend to emerge and decay?

(iii)   To what extent superflare stars have the differential rotation?

(iv)   What properties are related to superflares?

(v)   How many spots are actually on the surface?

In Section 2, to decipher the stellar and spot properties from the long-term photometric brightness modulations ascribed to spots, we implement a computational code for starspot modeling. We revisit synthetic light curves emulating *Kepler* data of spotted stars to evaluate the performance of the code. We qualitatively evaluate how stellar and spot properties can be deduced from the photometric brightness modulations toward conducting starspot modeling for photometric data obtained by *Kepler* and *Transiting Exoplanet Survey Satellite* (*TESS*).

In Section 3, we conduct starspot modeling for *TESS* light curves of renowned flare M-dwarfs, AU Microscopii, YZ Canis Minoris, and EV Lacertae. We investigate what spot properties the targets have on the surface. The targets are concurrently observed by *Seimei* 3.8m telescope at Kyoto University, which has embarked on spectroscopic observations of various targets and enables to reveal diverse astronomical phenomena, including the stellar magnetic activities.

Accompanied by an improvement of computational performance, advanced statistical methodology, such as machine learning techniques, has been developed and come into

use in astronomy. Therefore, it is actually great opportunity to deepen understandings of the stellar magnetic activities, and we intend to take full advantage of obtained data with advanced techniques. Therefore, other purpose of this thesis is to develop the techniques on processing of astronomical data.

# Chapter 2

# Starspot mapping with adaptive parallel tempering. I. Implementation of computational code (Ikuta et al. 2020, ApJ, 902, 73)

## 2.1 Introduction

In this Section, for the purpose of deducing stellar and spot properties from the photometric brightness modulations, we implement a computational code for starspot modeling. It is implemented with an adaptive parallel tempering (PT) algorithm (Hukushima and Nemoto 1996; Gregory 2005a,b; Vousden et al. 2016; Sharma 2017) and an importance sampling algorithm (e.g., Kass and Raftery 1995; Díaz et al. 2014) for parameter estimation and model selection in the Bayesian framework (see Neal 1996, 2001). The adaptive PT algorithm is based on the PT algorithm together with an adaptive algorithm (Haario et al. 2001; Andrieu and Thoms 2008; Araki and Ikeda 2013). As denoted in Section 1.1.3, starspot modeling has also been performed to decipher starspot properties on the stellar surface (e.g., Strassmeier and Bopp 1992; Savanov and Strassmeier 2008; Mosser et al. 2009), especially on the basis of Bayesian inference (Croll 2006; Croll et al. 2006; Walker et al. 2007; Frasca et al. 2011; Lanza et al. 2014; Almenara et al. 2018) using the Markov Chain Monte Carlo (MCMC) algorithm (Foreman-Mackey et al. 2013; Sharma 2017; Hogg and Foreman-Mackey 2018). Walker

et al. (2007) also implemented the PT algorithm in `StarSpotz` code (Croll 2006; Croll
et al. 2006) to explore multidimensional parameter space more efficiently. Compared
with the `StarSpotz` code (Walker et al. 2007), we adopt the more sophisticated spotted
model, including spot emergence and decay durations (Kipping 2012). Furthermore,
the number of spots on the stellar surface can play an important role in measuring
the emergence and decay rates. We determine the number of spots based on model
selection, computing the value of each model evidence by the importance sampling
algorithm.

Then, to evaluate the performance of the code, we revisit synthetic light curves
emulating *Kepler* data of spotted stars. We qualitatively evaluate how stellar and
spot properties can be deduced from the photometric brightness modulations under
appropriate assumptions toward conducting starspot modeling for photometric data
obtained by *Kepler* and *TESS*, as described in Section 3 (Ikuta et al. 2021, in
preparation, hereinafter, referred to as Paper II). The remainder of this Section is
organized as follows. In Section 2.2, we describe the algorithms based on Bayesian
inference and a numerical setup for starspot modeling. In Section 2.3, we discuss
the results of starspot modeling in terms of parameter degeneracies, determining the
number of spots, and their effects on the spot emergence and decay rates. In Section
3.4, we conclude this Section and describe future prospects to deal with real data.

## 2.2   Method

### 2.2.1   Bayesian inference: Adaptive PT algorithm

According to Bayes' theorem, the posterior distribution equals a product of the
likelihood and the prior distribution normalized by the model evidence $\mathcal{Z}$:

$$p(\theta|\mathcal{D}, M) = \frac{p(\mathcal{D}|\theta, M)p(\theta|M)}{\mathcal{Z}} \tag{2.1}$$

and

$$\mathcal{Z} = p(\mathcal{D}|M) = \int p(\mathcal{D}|\theta, M)p(\theta|M)d\theta, \tag{2.2}$$

where $\theta$, $\mathcal{D}$, and $M$ denote modeled parameters, observed data, and the assumed
model, respectively. In Bayesian inference, we compute the posterior distribution
of the modeled parameters $\theta$. However, in multidimensional cases of more than

several parameters, it becomes extremely difficult to compute Equation 2.2 as the normalization constant of the posterior distribution. In such cases, we usually use the Monte Carlo method as an approximation of inference sampling. In particular, for deducing the posterior distribution of such multidimensional parameters, the Markov Chain Monte Carlo (MCMC) algorithm has extensively been used in an astronomical context (Ford 2005, 2006; Foreman-Mackey et al. 2013; Nelson et al. 2014; Sharma 2017; Hogg and Foreman-Mackey 2018). Especially in the case of starspot modeling of photometric data, the MCMC algorithm has been applied to photometric data obtained by *Microvariability and Oscillations of Stars* (*MOST*) (`StarSpotz`; Croll 2006; Croll et al. 2006; Walker et al. 2007) and *Kepler* data (Frasca et al. 2011; Fröhlich et al. 2012; Lanza et al. 2014; Almenara et al. 2018). The MCMC algorithm can generate samples that follow the posterior distribution with a proposal distribution. However, in the case of a multimodal and multidimensional posterior distribution, the produced MCMC samples can be trapped in local maxima for so many iterations. Thus, the Parallel Tempering (PT) algorithm is occasionally implemented to circumvent this problem as in the `StarSpotz` code (Walker et al. 2007). The PT algorithm introduces auxiliary distributions with a tempering parameter $\beta_l : \pi_l(\theta) \equiv \{p(\mathcal{D}|\theta)\}^{\beta_l} p(\theta)$ ($1 = \beta_1 > \cdots > \beta_l > \cdots > 0$), where $\pi_1(\theta)$ corresponds to the posterior distribution $p(\theta|\mathcal{D})$ except the normalization constant. Hereby, $\beta_l$ tempers the multimodality of the likelihood $p(\mathcal{D}|\theta)$, and the peaks become less pronounced as $\beta_l \to 0$. It becomes easier for the corresponding Markov chain to step away from a local maximum, and chains with smaller $\beta_l$ are more readily able to explore the full parameter space.

The PT algorithm generates multiple MCMC samples from the posterior distribution and the auxiliary distributions in parallel, and exchanges the samples of two chains between a pair of adjacent chains only for some steps. This tempering implementation and the exchange process enable local maxima to be circumvented. The PT algorithm executes either transition or exchange at every iteration step with a probability $\alpha_r$ or $1 - \alpha_r$, respectively. The value of $\alpha_r$ is determined by exploiting the trial runs, and we set $\alpha_r = 0.10$. At transition steps, as specified in the MCMC algorithm, for each $l$ a proposed $\theta_l$ for the next iteration is drawn from a proposal distribution that is chosen to be a normal distribution characterized by a variance-covariance matrix $\Sigma_l$. The proposed $\theta_l$ is accepted or rejected according to the Metropolis-Hastings algorithm (Metropolis

et al. 1953; Hastings 1970). At the exchange step, a sample $\theta_l$ is randomly selected and exchanged for $\theta_{l+1}$ with probability of $\min\{(1, \pi_l(\theta_{l+1})\pi_{l+1}(\theta_l)/\pi_l(\theta_l)\pi_{l+1}(\theta_{l+1})\}$.

The performance of the PT algorithm strongly depends on the tempering parameters specifically determined by their intervals, number, and proposal parameters $\Sigma_l$. These must be selected so that each chain converges as fast as possible. They should be finely tuned by trial-and-error in test computations so far because their relation to the number of iterations until convergence has been unclear. Then, the adaptive algorithm for the Metropolis-Hastings algorithm is investigated in the statistical framework (Haario et al. 2001; Andrieu and Thoms 2008) and applied to astronomical data (Yamada et al. 2020) so that the MCMC acceptance rate in the multidimensional case approximately converges to the optimal value $= 0.25$ (Roberts et al. 1997). Furthermore, Araki and Ikeda (2013) investigate the adaptive algorithm for the PT algorithm so that the PT exchange rate between adjacent chains approximately converges to the optimal value $= 0.25$ (Roberts and Rosenthal 1998).

The adaptive algorithm adjusts the proposal parameters using past samples during iterations on the basis of the Robbins-Monro algorithm (Robbins and Monro 1951). For the adaptive Metropolis algorithm with adaptive scaling, normal proposal distribution $N(\theta_l, \sigma_l^2 \Sigma_l)$ is employed as a scale factor $\sigma_l^2$ is factored out from $\Sigma_l$, and $\Sigma_l$ are rescaled (Andrieu and Thoms 2008). At the $n$th transition step, the $l$th proposal parameters are updated as

$$\mu_{l,n+1} \leftarrow \mu_{l,n} + a_n(\theta_{l,n} - \mu_{l,n}) \tag{2.3}$$

$$\Sigma_{l,n+1} \leftarrow \Sigma_{l,n} + a_n\big((\theta_{l,n} - \mu_{l,n})(\theta_{l,n} - \mu_{l,n})^{\mathrm{T}} - \Sigma_{l,n}\big) \tag{2.4}$$

$$\sigma^2{}_{l,n+1} \leftarrow \sigma^2{}_{l,n} + a_n(FA_n - \alpha_{\mathrm{ac}}), \tag{2.5}$$

where $\mu_l$ is an auxiliary proposal parameter (expectation value of $\theta_l$), and also updated $\mu_{l,n+1} \leftarrow \theta_{l,n+1}$ when $\theta_{l,n}$ is updated to $\theta_{l,n+1}$ by being exchanged for $\theta_{l-1,n}$ or $\theta_{l+1,n}$ at the exchange step. $FA_n$ is one if the proposed sample is accepted or zero if it is rejected. $\alpha_{\mathrm{ac}} = 0.25$ is the optimal acceptance rate, which the MCMC acceptance rate should approach with the proceeding of iteration (Roberts et al. 1997). At the $n$th exchange step, the $l$th tempering parameter is updated as

$$\log \beta_{l,n+1} \leftarrow \log \beta_{l,n} - b_n(ER_{l,n} - \alpha_{\mathrm{ex}}). \tag{2.6}$$

$ER_{l,n}$ is one if parameters are exchanged or zero if not. $\alpha_{\text{ex}} = 0.25$ is the optimal exchange rate, which the PT exchange rate approaches with the proceeding of iteration (Roberts and Rosenthal 1998). The learning coefficients $a_n$ and $b_n$ converge to zero when the number of iterations $n$ approaches infinity. The details about the choice of the learning coefficients are described in Andrieu and Thoms (2008). In this study, we determined the number of iterations $N = 4 \times 10^6$ after the burn-in period $= 1 \times 10^6$ on the basis of the Gelman-Rubin convergence diagnostic (Gelman and Rubin 1992; Brooks and Gelman 1998). We set the learning coefficients $a_n = 1/(10n + N)$ and $b_n = 1/(n + N)$ so that the acceptance and exchange rates adequately approach to the moderate values, and the adaptive algorithms are executed after the burn-in period of the MCMC. In addition, we selected the number of parallelization $l = 10$ and the tempering parameters $\beta_l = \exp\{7(l-1)/2\}$ by exploiting the trial runs so that chains with small $\beta_l$ are much more easily able to transition in the full parameter space (see Vousden et al. 2016).

### 2.2.2   Importance sampling algorithm

For the purpose of determining the number of parameters as model selection, we compute model evidence (Equation 2.2) using the importance sampling algorithm along with PT transition. In Section 2.3.2, we compare the number of spots by the model evidence for the three-spot model, two-spot models, and the four-spot model. We briefly introduce the importance sampling algorithm (Kass and Raftery 1995).

Model evidence is approximated by Monte Carlo integration with $N$ samples as

$$\mathcal{Z} = \int p(\mathcal{D}|\theta, M)p(\theta|M)d\theta$$

$$\simeq \frac{1}{N}\Sigma_{n=1}^{N}p(\mathcal{D}|\theta_n, M), \tag{2.7}$$

where $\theta_n$ is drawn from $p(\theta|M)$. However, computation of the summation becomes quite inefficient if most of the likelihood $p(\mathcal{D}|\theta, M)$ have small values and the posterior distribution $p(\theta|\mathcal{D}, M)$ concentrates on a small region of the parameter space. $\mathcal{Z}$ is dominated by a few large values of the likelihood.

**26**

Starspot mapping with adaptive parallel tempering. I. Implementation of
computational code (Ikuta et al. 2020, ApJ, 902, 73)

To improve the precision of the Monte Carlo integration, the above formulation is deformed with the importance sampling function $q(\theta|M)$ as

$$\mathcal{Z} = \int p(\mathcal{D}|\theta, M)\frac{p(\theta|M)}{q(\theta|M)}q(\theta|M)d\theta$$
$$\simeq \frac{\Sigma_{n=1}^N w_n p(\mathcal{D}|\theta_n, M)}{\Sigma_{n=1}^N w_n}, \tag{2.8}$$

where $w_n = p(\theta_n|M)/q(\theta_n|M)$ and $\theta_n$ is drawn from $q(\theta|M)$. Adopting the posterior distribution $p(\theta|\mathcal{D}, M)$ as $q(\theta|M)$ since the samples can be drawn from the posterior distribution along with the PT transition, the model evidence $\mathcal{Z}$ is approximated as

$$\mathcal{Z} \simeq \left\{\frac{1}{N}\Sigma_{n=1}^N p(\mathcal{D}|\theta_n, M)^{-1}\right\}^{-1}. \tag{2.9}$$

This value converges to the precise value of the model evidence $p(\mathcal{D}|M)$ when the number of samples $N$ approaches infinity. Practically, we compute this value along with PT transition and use it for the model selection.

### 2.2.3  Analytical spotted model

According to Kipping (2012), a spotted flux at time $t$ is described by the functions $A$ and $\zeta_\pm$ of two parameters: the angular radius of the circular spot on the surface of the star as seen from the center of the star $\alpha$ and the angle between the line of sight and the line from the center of the star to the spot center $\beta$. The description summed up for the number of spots $N_{\mathrm{spot}}$ is formulated as

$$F(\boldsymbol{\alpha}, \boldsymbol{\beta}) = 1 - \sum_{j=0}^4 \left(\frac{jc_j}{j+4}\right) - \sum_{k=1}^{N_{\mathrm{spot}}} \frac{A_k}{\pi}\left[\left(\sum_{j=0}^4 \frac{4(c_j - d_j f_{\mathrm{spot}})}{j+4}\frac{\zeta_{+,k}^{(j+4)/2} - \zeta_{-,k}^{(j+4)/2}}{\zeta_{+,k}^2 - \zeta_{-,k}^2}\right)\right], \tag{2.10}$$

where

$$A_k = \begin{cases} \pi\sin^2\alpha_k\cos\beta_k & (0 < \beta_k < \pi/2 - \alpha_k) \\ \cos^{-1}[\cos\alpha_k\csc\beta_k] + \cos\beta_k\sin^2\alpha_k\cos^{-1}[-\cot\alpha_k\cot\beta_k] \\ \quad - \cos\alpha_k\sin\beta_k\sqrt{1 - \cos^2\alpha_k\csc^2\beta_k} & (\pi/2 - \alpha_k < \beta_k < \pi/2 + \alpha_k) \\ 0 & (\pi/2 + \alpha_k < \beta_k < \pi) \end{cases} \tag{2.11}$$

$$\zeta_{+,k} = \begin{cases} \cos(\beta_k + \alpha_k) & (0 < \beta_k < \pi/2 - \alpha_k) \\ 0 & (\pi/2 - \alpha_k < \beta_k < \pi) \end{cases} \tag{2.12}$$

$$\zeta_{-,k} = \begin{cases} 1 & (0 < \beta_k < \alpha_k) \\ \cos(\beta_k - \alpha_k) & (\alpha_k < \beta_k < \pi/2 + \alpha_k) \\ 0 & (\pi/2 + \alpha_k < \beta_k < \pi). \end{cases} \tag{2.13}$$

$A_k$ is the sky-projected area visible to the observer of spot $k$, and the inequalities within parentheses involving $\alpha_k$ and $\beta_k$ specify the conditions under which a spot is either fully visible on the near side of the star, partly visible, or fully invisible on the far side of the star, respectively. $c_j$, $d_j$ $(j = 0, 1, 2, 3, 4)$, and $f_{\mathrm{spot}}$ are the stellar limb-darkening coefficients, spot ones, and spot intensity relative to the photosphere, respectively. The temporal variation of $\alpha_k$ is represented by a trapezoidal function with time $t$ (Figure 1 in Kipping 2012). Then, $\alpha_k$ and $\beta_k$ relate to each spot and stellar parameter as

$$\alpha_k = \begin{cases} \alpha_{\mathrm{max},k}\{t - (t_k - \mathcal{L}_k/2 - \mathcal{I}_k)\}/\mathcal{I}_k & (t_k - \mathcal{L}_k/2 - \mathcal{I}_k < t < t_k - \mathcal{L}_k/2) \\ \alpha_{\mathrm{max},k} & (t_k - \mathcal{L}_k/2 < t < t_k + \mathcal{L}_k/2) \\ \alpha_{\mathrm{max},k}\{(t_k + \mathcal{L}_k/2 + \mathcal{E}_k) - t\}/\mathcal{E}_k & (t_k + \mathcal{L}_k/2 < t < t_k + \mathcal{L}_k/2 + \mathcal{E}_k) \\ 0 & (t < t_k - \mathcal{L}_k/2 - \mathcal{I}_k, t_k + \mathcal{L}_k/2 + \mathcal{E}_k < t), \end{cases} \tag{2.14}$$

$$\cos\beta_k = \cos i \sin\Phi_k + \sin i \cos\Phi_k \cos\{\Lambda_k + \frac{2\pi}{P(\Phi_k)}t\}, \tag{2.15}$$

and

$$P(\Phi_k) = \frac{P_{\mathrm{eq}}}{1 - \kappa \sin^2\Phi_k}, \tag{2.16}$$

where $\alpha_{\mathrm{max},k}$, $t_k$, $\mathcal{I}_k$, $\mathcal{E}_k$, and $\mathcal{L}_k$ are maximum radius, reference time (the time at the midpoint of the interval over which the spot has its maximum radius), emergence duration, decay duration, and stable duration, respectively. Each spot latitude $\Phi_k$ is assumed to be invariable, and each longitude is assumed to vary with time from the initial longitude $\Lambda_k$. The rotation period at the latitude $\Phi_k$ is characterized by equatorial period $P_{\mathrm{eq}}$ and the degree of differential rotation $\kappa$ as solar-like differential

rotation. The limb-darkening law is adopted as a quadratic term:

$$I(\mu)/I(1) = 1 - u_1(1 - \mu) - u_2(1 - \mu)^2, \tag{2.17}$$

where $\mu$ represents the cosine of the azimuthal angle. Then, the limb-darkening
coefficients are set as $c_1 = c_3 = d_1 = d_3 = 0, c_2 = d_2 = u_1 + 2u_2, c_4 = d_4 = -u_2$,
and $c_0 = d_0 = 1 - u_1 - u_2$. We adopt solar values of the limb-darkening coefficients
$c_2 = d_2 = 0.93, c_4 = d_4 = -0.23$ (Cox 2000). When applied to *Kepler* data of a
spotted star, the limb-darkening coefficients can be adopted, dependent on the stellar
parameters (Sing 2010).

Table 2.1: Two-spot-like light curve case

| Deduced parameters | Input value | Three-spot model | Two-spot model | Two-spot model with fixed $\sin i$ | Prior distribution[a] |
|---|---|---|---|---|---|
| **(Stellar parameters)** | | | | | |
| 1. Sine of inclination angle $\sin i$ | 0.8660 | $0.8346^{+0.0382}_{-0.0090}$ | $0.9951^{+0.0005}_{-0.0009}$ | 0.8660 (*fixed*) | $\mathcal{TN}(0.8660, 0.1500^2, 0.0000, 1.0000)$[b] |
| 2. Equatorial period $P_{eq}$ (day) | 25.0000 | $25.0431^{+0.0376}_{-0.0525}$ | $25.2645^{+0.0152}_{-0.1160}$ | $25.3125^{+0.0228}_{-0.0202}$ | $\mathcal{U}_{\log}(24.0000, 26.0000)$ |
| 3. Degree of differential rotation $\kappa$ | 0.1500 | $0.1941^{+0.0002}_{-0.0363}$ | $0.1097^{+0.0038}_{-0.0010}$ | $0.1642^{+0.0021}_{-0.0022}$ | $\mathcal{U}(0.0000, 0.2000)$ |
| **(Spot parameters)** | | | | | |
| 4. Relative intensity $f_{spot}$ | 0.3000 | $0.3356^{+0.0239}_{-0.0772}$ | $0.3403^{+0.0351}_{-0.0633}$ | $0.3658^{+0.0449}_{-0.0601}$ | $\mathcal{TN}(0.3000, 0.0500^2, 0.1500, 0.4500)$[c] |
| **(1st spot)** | | | | | |
| 5. Latitude $\Phi_1$ (deg) | 45.00 | $38.14^{+5.52}_{-0.18}$ | $77.29^{+0.32}_{-0.45}$ | $52.31^{+0.26}_{-0.33}$ | $\mathcal{U}(-90.00, 90.00)$ |
| 6. Initial longitude $\Lambda_1$ (deg) | -35.00 | $-34.30^{+0.69}_{-0.71}$ | $-26.30^{+0.39}_{-0.41}$ | $-26.00^{+0.39}_{-0.41}$ | $\mathcal{U}(-180.00, 180.00)$ |
| 7. Reference time $t_1$ (day) | 50.00 | $49.51^{+0.29}_{-0.33}$ | $75.81^{+0.16}_{-0.20}$ | $75.93^{+0.16}_{-0.20}$ | $\mathcal{U}(0.00, t_2)$[d] |
| 8. Maximum radius $\alpha_{\max,1}$ (deg) | 5.00 | $4.88^{+0.31}_{-0.11}$ | $12.81^{+0.29}_{-0.44}$ | $5.97^{+0.21}_{-0.28}$ | $\mathcal{U}(0.01, 15.00)$ |
| 9. Emergence duration $\mathcal{I}_1$ (day) | 70.000 | $68.917^{+0.832}_{-0.985}$ | $82.889^{+1.135}_{-1.087}$ | $80.745^{+1.352}_{-0.795}$ | $\mathcal{U}_{\log}(0.000, 200.000)$ |
| 10. Decay duration $\mathcal{E}_1$ (day) | 70.000 | $72.996^{+2.941}_{-1.845}$ | $75.709^{+0.792}_{-0.985}$ | $73.288^{+0.959}_{-0.693}$ | $\mathcal{U}_{\log}(0.000, 200.000)$ |
| 11. Stable duration $\mathcal{L}_1$ (day) | 30.000 | $29.645^{+0.530}_{-0.798}$ | $62.621^{+0.389}_{-0.462}$ | $62.315^{+0.337}_{-0.509}$ | $\mathcal{U}_{\log}(0.000, 200.000)$ |
| **(2nd spot)** | | | | | |
| 12. Latitude $\Phi_2$ (deg) | 30.00 | $25.26^{+3.60}_{-0.46}$ | $7.57^{+5.43}_{-2.69}$ | $-0.29^{+0.62}_{-0.79}$ | $\mathcal{U}(-90.00, 90.00)$ |
| 13. Initial longitude $\Lambda_2$ (deg) | -150.00 | $-151.20^{+1.49}_{-1.71}$ | $-23.30^{+1.69}_{-1.51}$ | $-22.40^{+2.19}_{-1.41}$ | $\mathcal{U}(-180.00, 180.00)$ |
| 14. Reference time $t_2$ (day) | 100.00 | $99.89^{+0.29}_{-0.24}$ | $151.95^{+0.43}_{-0.46}$ | $152.90^{+0.39}_{-0.47}$ | $\mathcal{U}(t_1, t_3)$[d,e] |
| 15. Maximum radius $\alpha_{\max,2}$ (deg) | 5.00 | $4.98^{+0.16}_{-0.21}$ | $5.06^{+0.11}_{-0.20}$ | $5.67^{+0.21}_{-0.27}$ | $\mathcal{U}(0.01, 15.00)$ |
| 16. Emergence duration $\mathcal{I}_2$ (day) | 70.000 | $70.704^{+1.450}_{-1.497}$ | $64.258^{+1.167}_{-0.944}$ | $70.520^{+0.873}_{-1.182}$ | $\mathcal{U}_{\log}(0.000, 200.000)$ |
| 17. Decay duration $\mathcal{E}_2$ (day) | 70.000 | $69.311^{+0.773}_{-0.854}$ | $49.009^{+5.633}_{-3.272}$ | $41.850^{+5.284}_{-3.237}$ | $\mathcal{U}_{\log}(0.000, 200.000)$ |
| 18. Stable duration $\mathcal{L}_2$ (day) | 30.000 | $30.472^{+0.420}_{-0.622}$ | $34.450^{+0.928}_{-0.938}$ | $35.759^{+0.635}_{-1.175}$ | $\mathcal{U}_{\log}(0.000, 200.000)$ |
| **(3rd spot)** | | | | | |
| 19. Latitude $\Phi_3$ (deg) | 15.00 | $12.27^{+2.60}_{-0.59}$ | - | - | $\mathcal{U}(-90.00, 90.00)$ |
| 20. Initial longitude $\Lambda_3$ (deg) | -25.00 | $-23.50^{+1.39}_{-1.81}$ | - | - | $\mathcal{U}(-180.00, 180.00)$ |
| 21. Reference time $t_3$ (day) | 150.00 | $150.51^{+0.39}_{-0.48}$ | - | - | $\mathcal{U}(t_2, 200.00)$[d] |
| 22. Maximum radius $\alpha_{\max,3}$ (deg) | 5.00 | $5.11^{+0.20}_{-0.19}$ | - | - | $\mathcal{U}(0.01, 15.00)$ |
| 23. Emergence duration $\mathcal{I}_3$ (day) | 70.000 | $69.082^{+1.009}_{-1.028}$ | - | - | $\mathcal{U}_{\log}(0.00, 200.000)$ |
| 24. Decay duration $\mathcal{E}_3$ (day) | 70.000 | $65.320^{+4.032}_{-4.379}$ | - | - | $\mathcal{U}_{\log}(0.00, 200.000)$ |
| 25. Stable duration $\mathcal{L}_3$ (day) | 30.000 | $31.551^{+0.445}_{-1.434}$ | - | - | $\mathcal{U}_{\log}(0.00, 200.000)$ |
| Model evidence $\log \mathcal{Z}$ | | 60257.571 | 57617.691 | 57507.414 | |

[a] Each representation of the prior distributions defined in $a \le \theta \le b$ are as follows: bounded uniform distribution $\mathcal{U}(a, b) = 1/(b - a)$; log uniform distribution $\mathcal{U}_{\log}(a, b) = \log \theta / \log(b/a)$ known as Jeffeys prior; truncated normal distribution $\mathcal{TN}(\mu, \sigma^2, a, b)$, which equals $\mathcal{N}(\mu, \sigma^2)$ normalized by its cumulative distribution.

[b] The variance value is based on currently achieved precision of spectroscopy (Notsu et al. 2019).

[c] The variance value is adopted from a formula of the spot temperature based on the Doppler imaging technique in the case of solar effective temperature (Berdyugina 2005; Maehara et al. 2017).

[d] We discern each of spot by the reference time $t_k$: if spots are not discerned, they are replaced one by one during the PT parameter transition. The number of maxima of the likelihood equals factorial of the number of spots, and the PT sampling becomes very inefficient.

[e] For the two-spot model and two-spot model with fixed $\sin i$, we set $t_3 = 200.000$ (upper limit of the interval of the light curve).

Table 2.2: One-spot-like light curve case

| Deduced parameters | Input value | Three-spot model | Two-spot model | Two-spot model with fixed $\sin i$ | Prior distribution[a] |
|---|---|---|---|---|---|
| **(Stellar parameters)** | | | | | |
| 1. Sine of inclination angle $\sin i$ | 0.8660 | $0.8976^{+0.0054}_{-0.0647}$ | $0.9874^{+0.0013}_{-0.0024}$ | 0.8660 (*fixed*) | $\mathcal{TN}(0.8660, 0.1500^2, 0.0000, 1.0000)$[b] |
| 2. Equatorial period $P_{\mathrm{eq}}$ (day) | 25.0000 | $24.9756^{+0.0550}_{-0.0748}$ | $24.4909^{+0.1400}_{-0.1002}$ | $25.0607^{+0.0251}_{-0.0526}$ | $\mathcal{U}_{\mathrm{log}}(24.0000, 26.0000)$ |
| 3. Degree of differential rotation $\kappa$ | 0.1500 | $0.1340^{+0.0426}_{-0.0075}$ | $0.0467^{+0.0041}_{-0.0057}$ | $0.0331^{+0.0028}_{-0.0020}$ | $\mathcal{U}(0.0000, 0.2000)$ |
| **(Spot parameters)** | | | | | |
| 4. Relative intensity $f_{\mathrm{spot}}$ | 0.3000 | $0.3050^{+0.0487}_{-0.0336}$ | $0.2974^{+0.0767}_{-0.0152}$ | $0.3518^{+0.0486}_{-0.0609}$ | $\mathcal{TN}(0.3000, 0.0500^2, 0.1500, 0.4500)$[c] |
| (1st spot) | | | | | |
| 5. Latitude $\Phi_1$ (deg) | 45.00 | $48.28^{+2.20}_{-7.76}$ | $75.92^{+0.35}_{-0.72}$ | $55.38^{+0.22}_{-0.28}$ | $\mathcal{U}(-90.00, 90.00)$ |
| 6. Initial longitude $\Lambda_1$ (deg) | 55.00 | $54.90^{+0.69}_{-0.81}$ | $32.40^{+0.39}_{-0.51}$ | $32.60^{+0.49}_{-0.41}$ | $\mathcal{U}(-180.00, 180.00)$ |
| 7. Reference time $t_1$ (day) | 50.00 | $50.21^{+0.42}_{-0.52}$ | $83.86^{+0.13}_{-0.23}$ | $83.95^{+0.19}_{-0.18}$ | $\mathcal{U}(0.00, t_2)$[d] |
| 8. Maximum radius $\alpha_{\mathrm{max},1}$ (deg) | 5.00 | $5.06^{+0.40}_{-0.17}$ | $11.34^{+0.30}_{-0.54}$ | $6.09^{+0.32}_{-0.20}$ | $\mathcal{U}(0.01, 15.00)$ |
| 9. Emergence duration $\mathcal{I}_1$ (day) | 70.000 | $67.235^{+2.591}_{-3.003}$ | $104.731^{+1.222}_{-0.847}$ | $101.301^{+1.131}_{-0.847}$ | $\mathcal{U}_{\mathrm{log}}(0.000, 200.000)$ |
| 10. Decay duration $\mathcal{E}_1$ (day) | 70.000 | $69.930^{+4.191}_{-4.629}$ | $72.010^{+0.956}_{-1.975}$ | $67.904^{+1.130}_{-1.484}$ | $\mathcal{U}_{\mathrm{log}}(0.000, 200.000)$ |
| 11. Stable duration $\mathcal{L}_1$ (day) | 30.000 | $30.624^{+0.754}_{-0.940}$ | $61.412^{+0.400}_{-0.392}$ | $62.004^{+0.354}_{-0.426}$ | $\mathcal{U}_{\mathrm{log}}(0.000, 200.000)$ |
| (2nd spot) | | | | | |
| 12. Latitude $\Phi_2$ (deg) | 30.00 | $34.08^{+1.61}_{-6.15}$ | $45.43^{+2.24}_{-2.82}$ | $17.13^{+0.99}_{-1.00}$ | $\mathcal{U}(-90.00, 90.00)$ |
| 13. Initial longitude $\Lambda_2$ (deg) | 75.00 | $77.90^{+2.59}_{-2.21}$ | $-65.60^{+3.29}_{-2.51}$ | $-61.30^{+2.59}_{-3.51}$ | $\mathcal{U}(-180.00, 180.00)$ |
| 14. Reference time $t_2$ (day) | 100.00 | $100.68^{+0.46}_{-0.56}$ | $150.44^{+1.28}_{-0.93}$ | $150.95^{+0.93}_{-1.40}$ | $\mathcal{U}(t_1, t_3)$[d,e] |
| 15. Maximum radius $\alpha_{\mathrm{max},2}$ (deg) | 5.00 | $5.05^{+0.17}_{-0.14}$ | $5.57^{+0.30}_{-0.14}$ | $4.99^{+0.21}_{-0.22}$ | $\mathcal{U}(0.01, 15.00)$ |
| 16. Emergence duration $\mathcal{I}_2$ (day) | 70.000 | $66.746^{+3.542}_{-2.173}$ | $39.158^{+0.775}_{-0.940}$ | $38.637^{+0.867}_{-0.852}$ | $\mathcal{U}_{\mathrm{log}}(0.000, 200.000)$ |
| 17. Decay duration $\mathcal{E}_2$ (day) | 70.000 | $69.651^{+1.272}_{-1.767}$ | $100.786^{+6.404}_{-17.922}$ | $97.018^{+8.629}_{-16.458}$ | $\mathcal{U}_{\mathrm{log}}(0.000, 200.000)$ |
| 18. Stable duration $\mathcal{L}_2$ (day) | 30.000 | $30.963^{+0.755}_{-0.764}$ | $25.394^{+1.430}_{-3.138}$ | $24.693^{+1.856}_{-3.006}$ | $\mathcal{U}_{\mathrm{log}}(0.000, 200.000)$ |
| (3rd spot) | | | | | |
| 19. Latitude $\Phi_3$ (deg) | 15.00 | $15.98^{+1.64}_{-3.22}$ | - | - | $\mathcal{U}(-90.00, 90.00)$ |
| 20. Initial longitude $\Lambda_3$ (deg) | -50.00 | $-54.00^{+4.49}_{-2.21}$ | - | - | $\mathcal{U}(-180.00, 180.00)$ |
| 21. Reference time $t_3$ (day) | 150.00 | $149.90^{+0.86}_{-1.37}$ | - | - | $\mathcal{U}(t_2, 200.00)$[d] |
| 22. Maximum radius $\alpha_{\mathrm{max},3}$ (deg) | 5.00 | $5.04^{+0.15}_{-0.18}$ | - | - | $\mathcal{U}(0.01, 15.00)$ |
| 23. Emergence duration $\mathcal{I}_3$ (day) | 70.000 | $70.000^{+3.545}_{-5.136}$ | - | - | $\mathcal{U}_{\mathrm{log}}(0.00, 200.000)$ |
| 24. Decay duration $\mathcal{E}_3$ (day) | 70.000 | $71.902^{+15.202}_{-6.103}$ | - | - | $\mathcal{U}_{\mathrm{log}}(0.00, 200.000)$ |
| 25. Stable duration $\mathcal{L}_3$ (day) | 30.000 | $29.131^{+1.662}_{-3.178}$ | - | - | $\mathcal{U}_{\mathrm{log}}(0.00, 200.000)$ |
| Model evidence $\log \mathcal{Z}$ | | 60307.348 | 59406.380 | 59355.393 | |

[a] Each representation of the prior distributions defined in $a \leq \theta \leq b$ are as follows: bounded uniform distribution $\mathcal{U}(a, b) = 1/(b - a)$; log uniform distribution $\mathcal{U}_{\mathrm{log}}(a, b) = \log \theta / \log(b/a)$ known as Jeffeys prior; truncated normal distribution $\mathcal{TN}(\mu, \sigma^2, a, b)$, which equals $\mathcal{N}(\mu, \sigma^2)$ normalized by its cumulative distribution.

[b] The variance value is based on currently achieved precision of spectroscopy (Notsu et al. 2019).

[c] The variance value is adopted from a formula of the spot temperature based on the Doppler imaging technique in the case of solar effective temperature (Berdyugina 2005; Maehara et al. 2017).

[d] We discern each of spot by the reference time $t_k$: if spots are not discerned, they are replaced one by one during the PT parameter transition. The number of maxima of the likelihood equals factorial of the number of spots, and the PT sampling becomes very inefficient.

[e] For the two-spot model and two-spot model with fixed $\sin i$, we set $t_3 = 200.000$ (upper limit of the interval of the light curve).

## 2.2.4 Numerical setup

We employ a normal likelihood function as

$$p(\mathcal{D}|\theta) = \prod_i \frac{1}{\sqrt{2\pi\sigma_i^2}} \exp\left[-\frac{\left(F_{\mathrm{obs},i} - F_{\mathrm{mod},i}(\theta)\right)^2}{2\sigma_i^2}\right] \tag{2.18}$$

and

$$F_{\mathrm{mod},i}(\theta) = F(\boldsymbol{\alpha}_i, \boldsymbol{\beta}_i)/F_{\mathrm{ave}} - 1, \tag{2.19}$$

where $\sigma_i$, $F_{\mathrm{obs},i}$, $F_{\mathrm{mod},i}(\theta)$, and $F_{\mathrm{ave}}$ are photometric error, relative flux scaled as Equation 2.19 for synthetic data emulated as observation, relative model flux characterized by parameters $\theta$ at the time $t_i$, and the average of $F(\boldsymbol{\alpha}_i, \boldsymbol{\beta}_i)$, respectively.

In Table 2.1 and 2.2, deduced parameters $\theta$ are denoted as the stellar and spot parameters: sine of inclination angle $\sin i$; equatorial rotation period $P_{\mathrm{eq}}$ (day); degree of differential rotation $\kappa$; relative intensity $f_{\mathrm{spot}}$; latitude $\Lambda_k$ (deg); longitude $\Phi_k$ (deg); reference time $t_k$ (day); maximum radius $\alpha_{\mathrm{max},k}$ (deg); emergence duration $\mathcal{I}_k$ (day); decay duration $\mathcal{E}_k$ (day); and stable duration $\mathcal{L}_k$ (day). As each prior distribution, we selected truncated uniform, log-uniform (Jeffery's prior), and normal distributions; it is shown that there are degeneracies between the inclination angle $i$ and each spot latitude $\Phi$, and between the spot intensity $f_{\mathrm{spot}}$ and each spot size $\alpha$ (Eker 1996; Walkowicz et al. 2013). Each spot is discerned by the range of the reference time $t_k$ so that the spots are not replaced one by one during the PT parameter transition as denoted in Table 2.1 and 2.2. Furthermore, in the case of $\sin i \sim 1$, there are degeneracies between each spot latitude $\Phi$ and each spot size $\alpha$ (see Figure 1 Namekata et al. 2020). In other words, similar light curves can be generated by either a large spot at high latitude or a small spot at low latitude. Whether each spot exists on the northern or southern hemisphere is also indiscernible. Therefore, we constrain the inclination angle and spot intensity as truncated normal distributions under the currently achieved precision (Maehara et al. 2017; Notsu et al. 2019).

### 2.2.5   Synthetic light curves toward *Kepler* data

Hereafter, for the purpose of modeling *Kepler* data of spotted stars, we produced two synthetic light curves with three spots for approximately two *Kepler* quarters ($\sim 200$ days) so that they have quasiperiodic modulations ascribed to the spots. These light curves are generated with the spotted model (Kipping 2012) in addition to random error ($\sim 10\%$ of modulation amplitude), emulating most faint *Kepler* stars and assuming spot-dominated stars (Montet et al. 2017). The input values to produce the light curves are listed in Tables 2.1 and 2.2. Assuming the inclination angle of a star is randomly distributed in real data, the expectation value equals 1 (rad) (Gray 2008). Then, the values of the inclination angle are set 60 (deg), and each value of the spot latitudes are determined to be less than the value of the inclination angle so that the spots can be visible and invisible by the stellar rotation. We note that it is difficult to

deduce the parameters of always visible spots at higher latitudes than the inclination angle. Each value of the spot longitudes is determined so that the light curves have two or one local minimum during one equatorial rotation period by adjusting the values of longitude. Hereinafter, we call each of the light curves two-spot-like or one-spot-like, respectively. In 45° and 30° cases of the inclination angle, we also produced such light curves and optimized them as well as the 60-deg case. Thereby, we ascertained the accuracies of the deduced parameters are almost the same as that of the 60° case by exploiting the test runs. This is because the accuracy of the posterior distribution of the inclination angle depends on its variance of the prior distribution, and this reflects the deduced accuracies of other parameters with degeneracies with the inclination angle. Although the stellar continuum level is unknown due to some effects such as polar spots (e.g., Basri 2018), it is assumed to be invariant for the interval of the light curves because large spots are suggested to live for a few hundred days (Giles et al. 2017).

## 2.3 Results and Discussion

We optimize two-spot-like and one-spot-like light curves by three-spot model, two-spot model, and two-spot model with fixed inclination angle $\sin i$. In each case, unimodal posterior distributions are deduced. In the three-spot model, the modes approximately equal the input values producing the light curves. In the two-spot model, deduced posterior distributions have a mode of large spot radius at high latitude with higher inclination angle than the mode of the truncated normal prior distribution. Thus, the light curves are also optimized by the two-spot model with fixed $\sin i$. Table 2.1 and 2.2 show the modes of the deduced posterior distributions, their credible regions, and the model evidence for each model, together with the input values and their prior distributions for each of the parameters. Figure 2.1, 2.2, 2.3 and 2.4, 2.5, 2.6 show the results of the two-spot-like case and one-spot-like case, respectively: (a) the light curve produced with the input values of the parameters (gray), that were reproduced with each mode of the deduced unimodal posterior distribution (red), and their residuals (black); and (b) the temporal radius variation of each spot produced with the input values of the parameters (gray), and those for the three-spot model, two-spot model, and two-spot model with fixed $\sin i$ (red, blue, and green), respectively.

The inclination angle, degree of differential rotation, relative intensity, latitude, and radius have degeneracies between any of them. Their joint posterior distributions are delineated in Figure 2.7, 2.8, and 2.9 for the two-spot-like case and Figure 2.10, 2.11, and 2.12 for the one-spot-like case generated using open software `corner` (Foreman-Mackey 2016). The calculated spots on the stellar surface and the light curves are visualized in Figure 2.13 and 2.14. We discuss each degeneracy between the parameters in Section 2.3.1, model selection determining the number of spots in Section 2.3.2, and the effects on estimating spot lifetime in Section 2.3.3.

## 2.3.1 Degeneracy between parameters

**Inclination angle vs Spot latitude**

Inclination and each spot latitude are not uniquely deduced under uniform prior distributions due to the degeneracies (Eker 1996; Walkowicz et al. 2013). Therefore, the sine of the inclination angle is constrained as a truncated normal prior distribution with the center equivalent to the input value ($= \sin 60°$) and with the variance ($= 0.15^2$) based on currently achieved precision of spectroscopy (Tables 2.1 and 2.2) (Notsu et al. 2013a, 2015a,b, 2019; Nogami et al. 2014). Then, posterior distributions of the inclination angle and spot latitudes are unimodally and adequately deduced from the photometric light curve. We note that the posterior distributions of the inclination angle deduced from the light curve is likely to have a higher accuracy than that would be deduced from real data.

**Spot relative intensity vs Spot radius**

Spot relative intensity and each spot size are not uniquely deduced under the uniform prior distributions due to the degeneracies (Walkowicz et al. 2013). Therefore, the spot relative intensity is constrained as a normal prior distribution with the center equivalent to the input value ($= 0.30$) and with the variance ($= 0.05^2$) adopted from a formula of the spot temperature based on the Doppler imaging technique (Tables 2.1 and 2.2) (e.g., Berdyugina 2005). Then, the spot relative intensity and each spot radius are unimodally and adequately deduced from the photometric light curve. We note that the posterior distributions of the relative intensity deduced from the light curve is also likely to have a higher accuracy than that would be deduced from real data.

**Differential rotation vs Spot latitude**

There are degeneracies between the degree of differential rotation and the spot latitudes due to adjusting the periodicity for each spot (Equation 2.16). However, the deduction of the spot latitude depends on that of the inclination angle, and thus the degree of differential rotation is unimodally deduced from the photometric light curve only if the number of spots is more than two.

**Spot latitude vs Spot radius**

There are degeneracies between spot latitudes and the spot radii because the same modulation amplitude is generated by adjusting the parameters (see Namekata et al. 2020). However, the deduction of the spot latitude depends on that of the inclination angle, and thus the spot radius is unimodally deduced from the photometric light curve. We note that when the inclination angle becomes too small, the spots are always visible and do not significantly modulate the light curve.

## 2.3.2   Model selection: How many spots exist?

More spots are observationally indicated to exist than seen in the light curve (Morris et al. 2017; Namekata et al. 2020), whereas the light curve produced with many spots is similar to that with two spots or one spot (Eker 1994; Basri 2018). Then, we determine the number of spots based on model selection in the Bayesian framework (Kass and Raftery 1995). We compute the model evidence using the importance sampling algorithm along with the PT transition and compare each model. The values of the model evidence $\log \mathcal{Z}$ are listed in Table 2.1 and 2.2. In both cases, the three-spot model is much more decisive than the two-spot model and the two-spot model with fixed $\sin i$ by orders of magnitude: for the two-spot-like case, the evidence of the three-spot model relative to that of the two-spot model and the two-spot model with fixed $\sin i$ are $\Delta \log \mathcal{Z} = 2639.880$ and $2750.157$, respectively. For the one-spot-like one, they are $\Delta \log \mathcal{Z} = 900.968$ and $951.955$, respectively. The difference of the values of the model evidence for the two-spot-like light curve is much larger than that of the one-spot-like one because the two-spot-like one is much more informative to deduce spot properties, such as spot emergence and decay rates (Namekata et al. 2019). In addition, when optimizing light curves by the four-spot model, the PT sampling converge to the a multimodal distribution with many peaks and with degeneracies

between the parameters. For the two-spot-like case, the values of the model evidence of the four-spot model and the evidence of the three-spot model relative to that of the four-spot model are $\log \mathcal{Z} = 60257.257$ and $\Delta \log \mathcal{Z} = 0.314$, respectively. For the 1-spot-like case, they are $\log \mathcal{Z} = 60305.432$ and $\Delta \log \mathcal{Z} = 1.916$, respectively. Then, the three-spot model is preferable, and the number of spots can be correctly determined in the case of the synthetic light curve. We note that, when conducting starspot modeling of real data, spots are not completely circular, and small spots can be ignored.

### 2.3.3  Effect on estimating spot emergence and decay rates

The number of spots can directly affect measuring emergence and decay rates. For instance, when optimizing the light curve produced with three spots by the two-spot models, two spots out of three spots behave as one. Thus, we qualitatively evaluate an estimation of the spot emergence and decay rates ($\sim \alpha_{\max,k}^2/\mathcal{I}_k$, $\alpha_{\max,k}^2/\mathcal{E}_k$). Relative to the three-spot model, the two-spot model overestimates by a factor of up to 6 because the inclination angle is large and the spot is at high latitude. In the two-spot model with fixed $\sin i$, the estimates are larger than those of the three-spot model by a factor of up to 2. These values can have an error of an order of magnitude in the range of the photometic error.

## 2.4  Conclusion and future prospects

We implement a computational code for starspot modeling to deduce stellar and spot properties from photometric brightness modulations. It is implemented with an adaptive PT algorithm and an importance sampling algorithm for parameter estimation and model selection in the Bayesian framework. In this paper, for evaluating the performance of the code, we apply it to synthetic light curves emulating *Kepler* data of spotted stars. The light curves are specified in the spot parameters, such as the radii, intensities, latitudes, longitudes, and emergence/decay durations, and produced with three spots so that they have two or one local minimum during one equatorial rotation period by adjusting the values of longitude. The spots are circular with specified radii and intensities relative to the photosphere, and the stellar differential rotation coefficient is also included in the light curves. We conduct starspot modeling

for the light curves, optimizing by the three-spot model (Figure 2.1 and 2.4), two-spot model (Figure 2.2 and 2.5), and two-spot model with fixed $\sin i$ (Figure 2.3 and 2.6). The calculated spots on the stellar surface and the light curves are visualized (Figure 2.13 and 2.14). To determine the number of spots, we compare the value of the model evidence for each model. In Section 2.3, we describe the results, which can be summarized as follows:

(i) Unimodal posterior distributions are deduced in all of the models (Table 2.1 and 2.2). In the three-spot model, of course, the modes of the posterior distribution approximately equal the input values of the parameters producing the synthetic light curves. Then, the degeneracies between the parameters are eliminated by constraining the inclination angle and the relative intensity with truncated normal prior distributions (Figure 2.7-2.9 for two-spot-like case and Figure 2.10-2.12 for one-spot-like case).

(ii) The three-spot model is decisive because the model evidence is much larger than that of the two-spot model or two-spot model with fixed $\sin i$ by orders of magnitude (Table 2.1, 2.2). Optimizing light curves by the four-spot model, the PT sampling converges to a multimodal distribution with many peaks and with degeneracies between the parameters. Comparing the value of the model evidence with that of the three-spot model, the three-spot model is preferable, and the number of spots can be correctly determined in the case of the synthetic light curve.

(iii) Spot emergence and decay rates can be estimated within an error less than an order of magnitude, considering the three-spot model, two-spot model, and two-spot model with fixed $\sin i$.

In the next paper (Paper II), we intend to conduct starspot modeling for *Kepler* and *TESS* data of spotted stars. In particular, *Kepler* data include solar-type stars on which superflares are reported (Notsu et al. 2019; Okamoto et al. 2020). We note that *Kepler* data include a long-term trend and instrumental noise, and their unspotted level is unknown (e.g., Basri 2018). It is also necessary to determine the inclination angle precisely by another method, such as spectroscopic observation, when conducting starspot modeling. Then, we can investigate the connection between superflares and stellar and spot properties deduced by starspot modeling and compare the results of

measuring emergence and decay rates with those by other methods (Namekata et al. 2020). Bright spotted stars have been observed by *TESS* (Ricker et al. 2014), and superflares on hundreds of spotted solar-type stars have been reported (Tu et al. 2020; ?). Some *TESS* targets are to be simultaneously observed by the *Seimei* telescope at Kyoto University (Kurita et al. 2020) using the high dispersion spectrograph. This could allow us to obtain informative prior knowledge for conducting starspot modeling of *TESS* data.
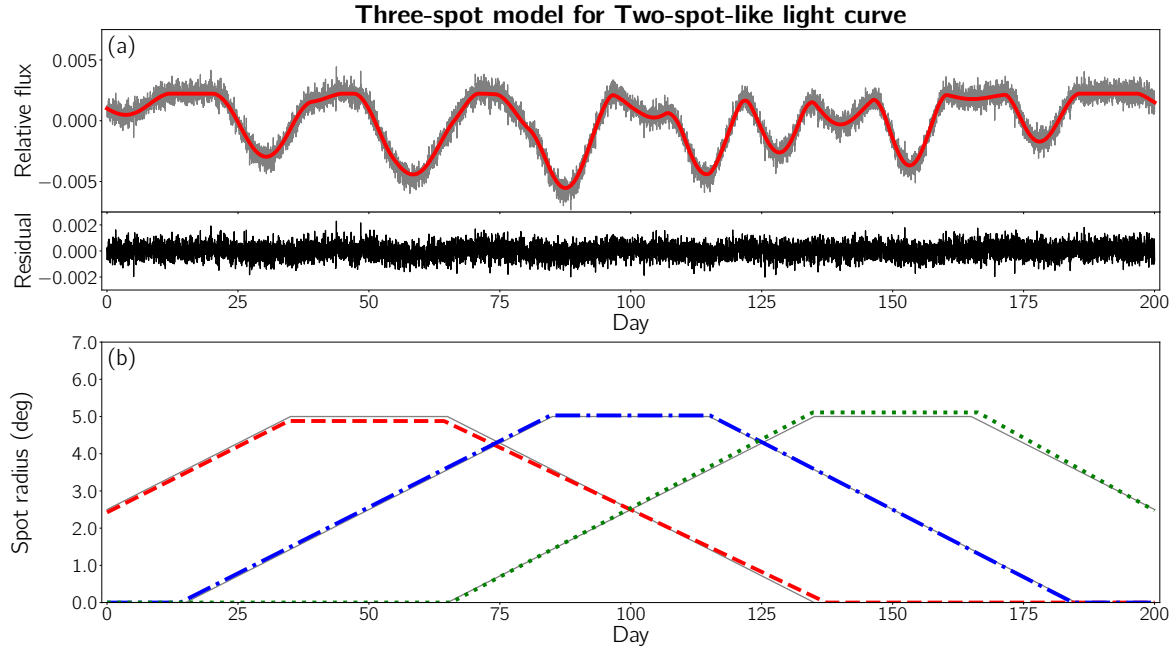


Figure 2.1: (a) Two-spot-like light curves produced with the input values of the parameters (gray), those reproduced with each mode of the deduced unimodal posterior distribution for the three-spot model (red), and their residuals (black). (b) Temporal radius variation of each spot produced with the input values of the parameters (gray), and that of the three-spot model (red, blue, and green).
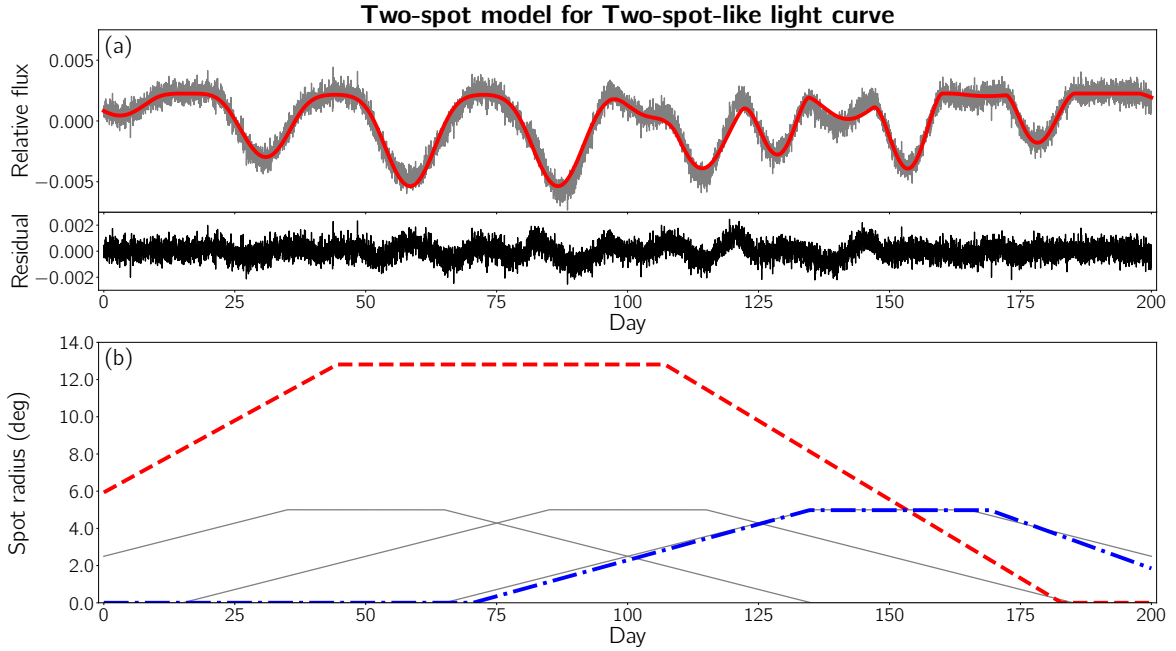
Figure 2.2: Same as Figure 2.1 but for the two-spot model.
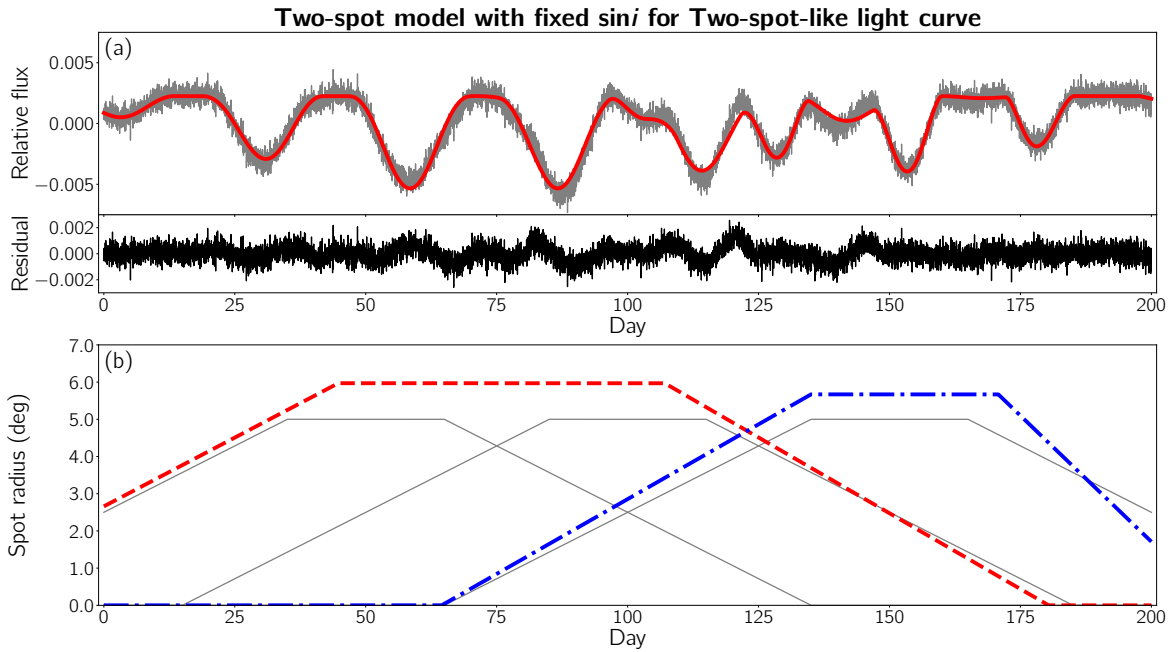


Figure 2.3: Same as Figure 2.1 but for the two-spot model with fixed $\sin i$.
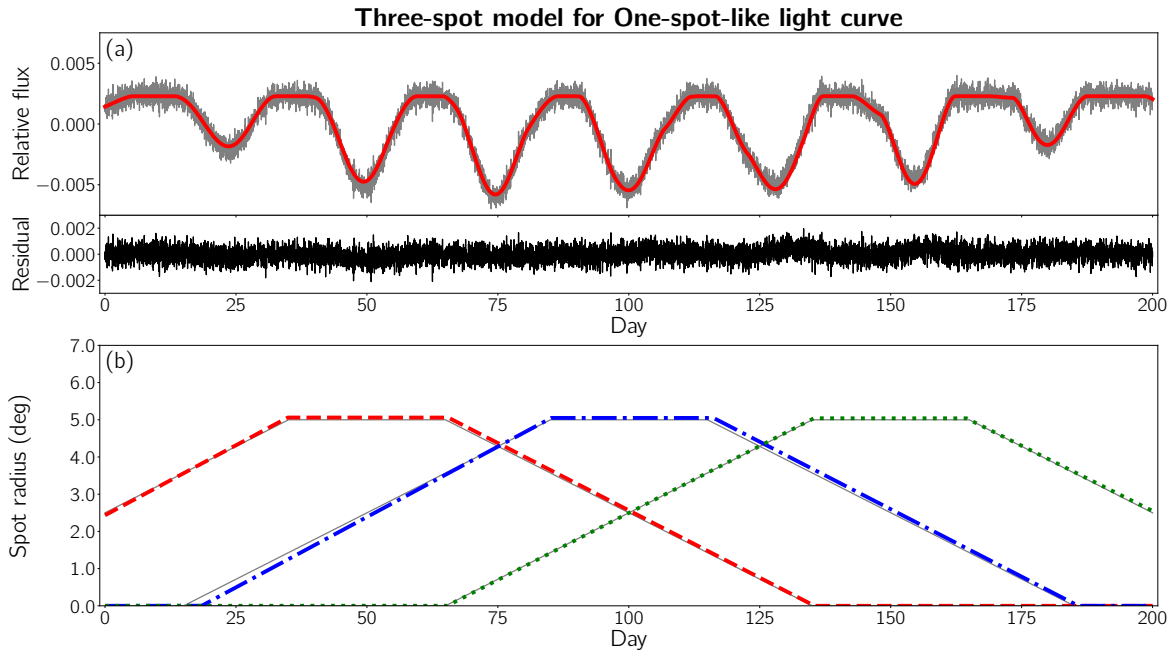
Figure 2.4: (a) One-spot-like light curves produced with the input values of the parameters (gray), those reproduced with each mode of the deduced unimodal posterior distribution for the three-spot model (red), and their residuals (black). (b) Temporal radius variation of each spot produced with the input values of the parameters (gray), and that of the three-spot model (red, blue, and green).
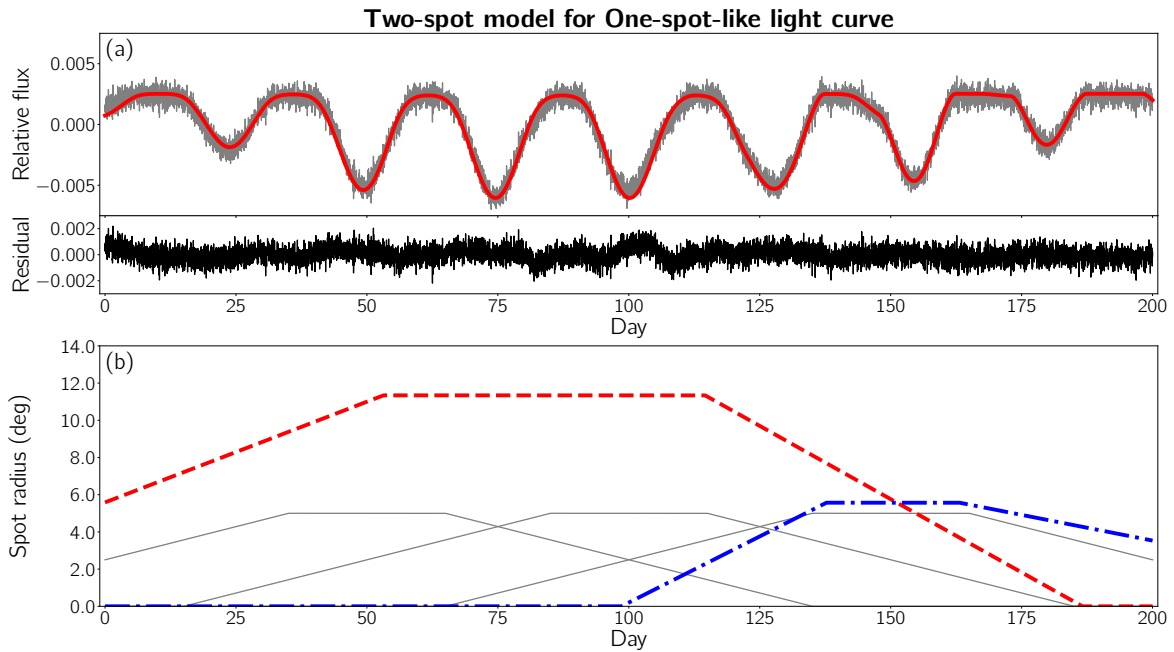


Figure 2.5: Same as Figure 2.4 but for the two-spot model.
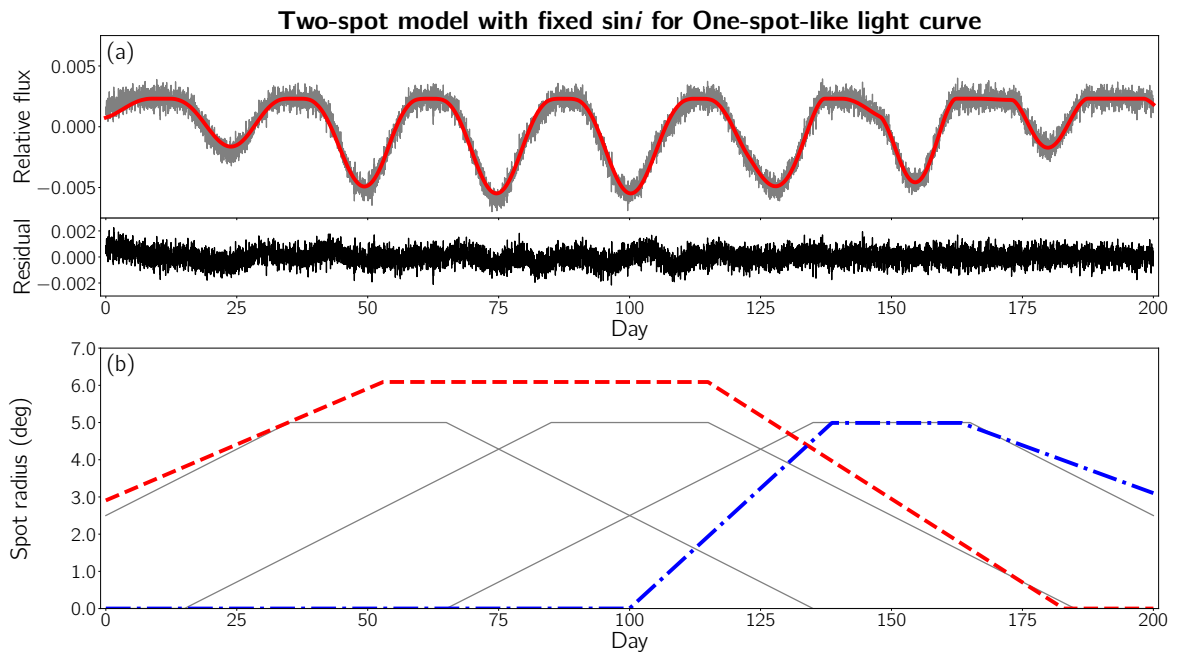
Figure 2.6: Same as Figure 2.4 but for the two-spot model with fixed $\sin i$.
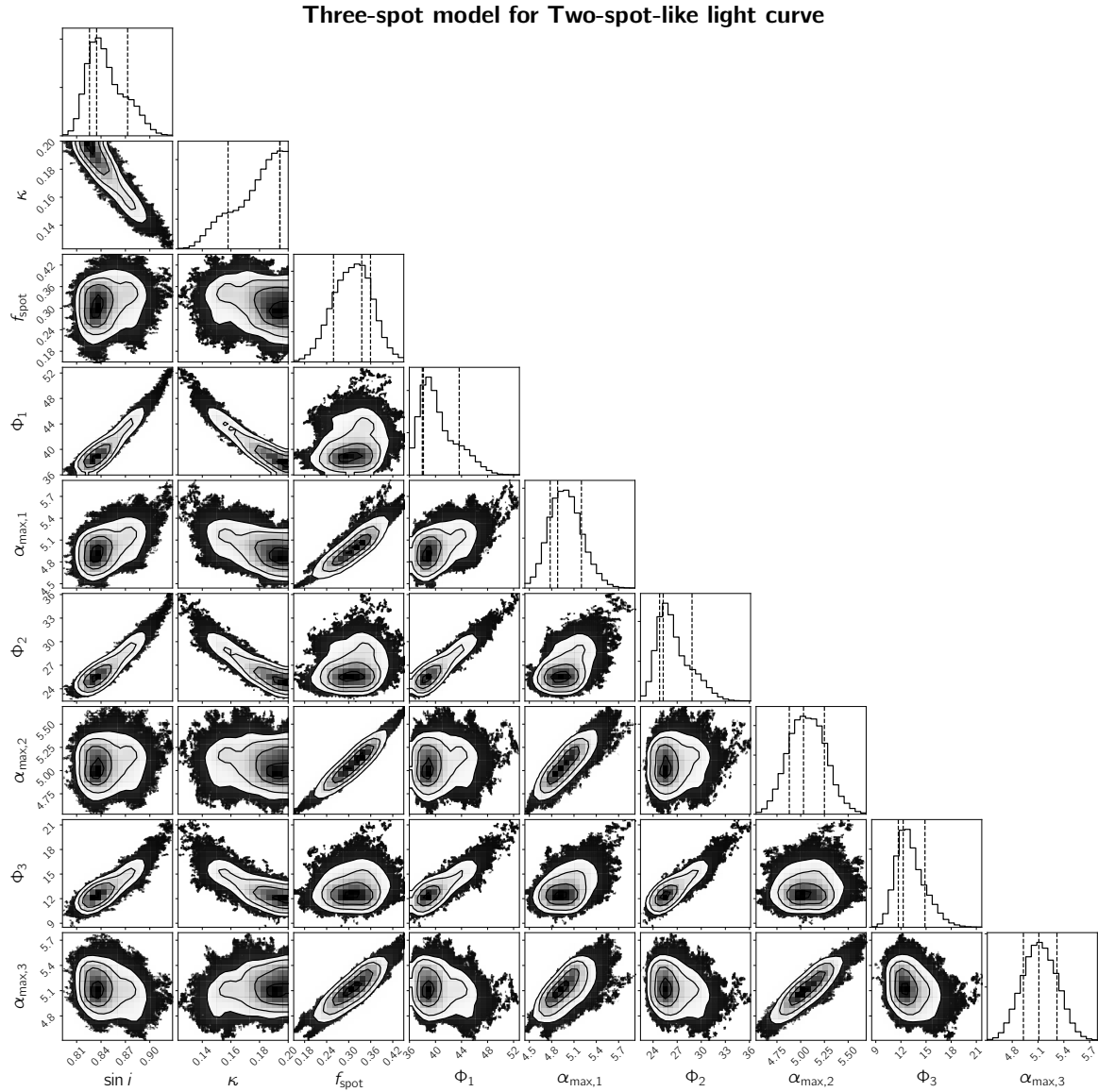
Figure 2.7: The joint posterior distribution of parameters with the degeneracies for two-spots-like light curve by the three-spot model. Each column represents the inclination angle $\sin i$, degree of differential rotation $\kappa$, relative intensity $f_{\rm spot}$, maximum radius $\alpha_{\rm max, k}$, and latitude $\Phi_k$.
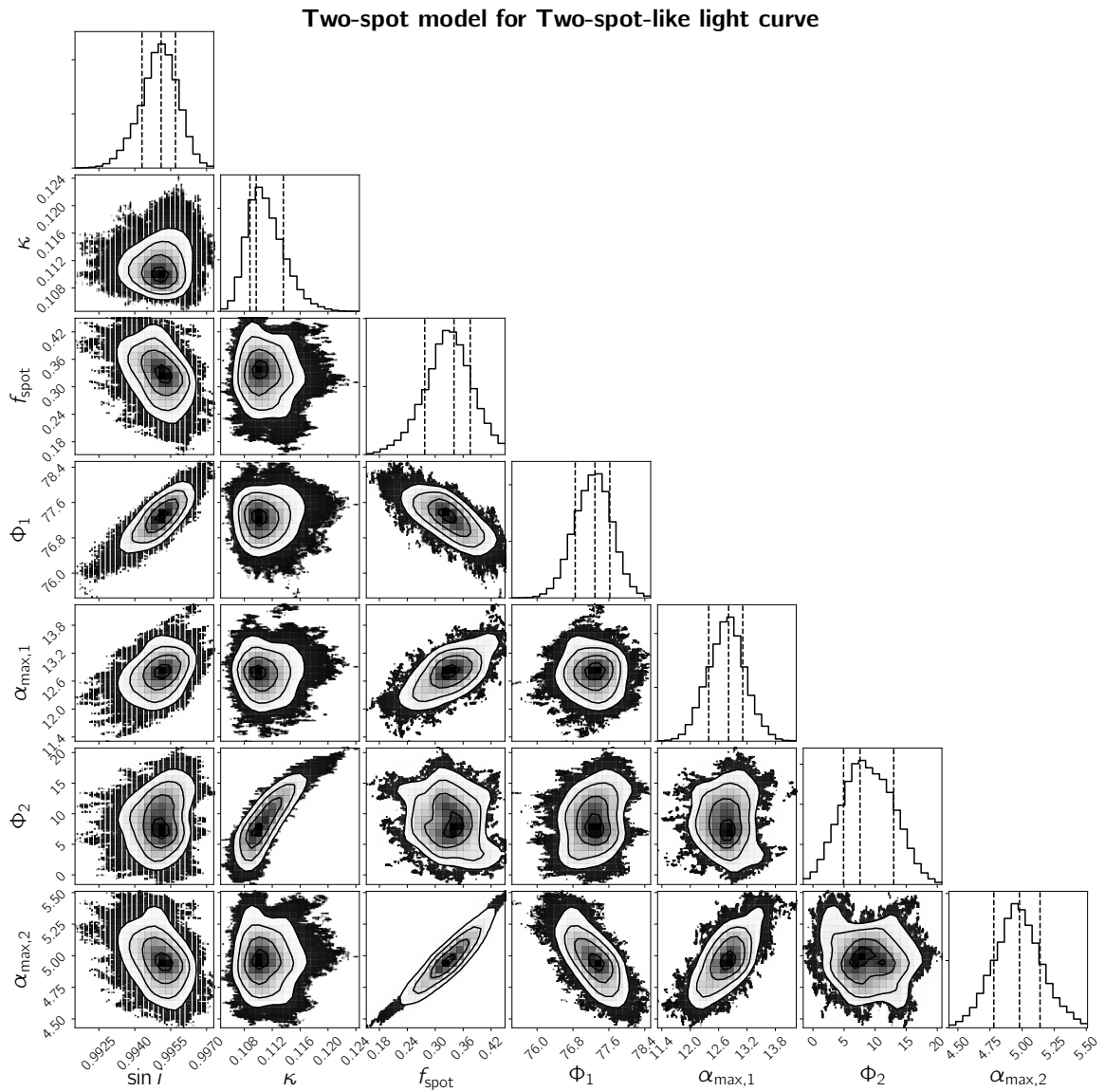
Figure 2.8: Same as Figure 2.7 but for the two-spot model.
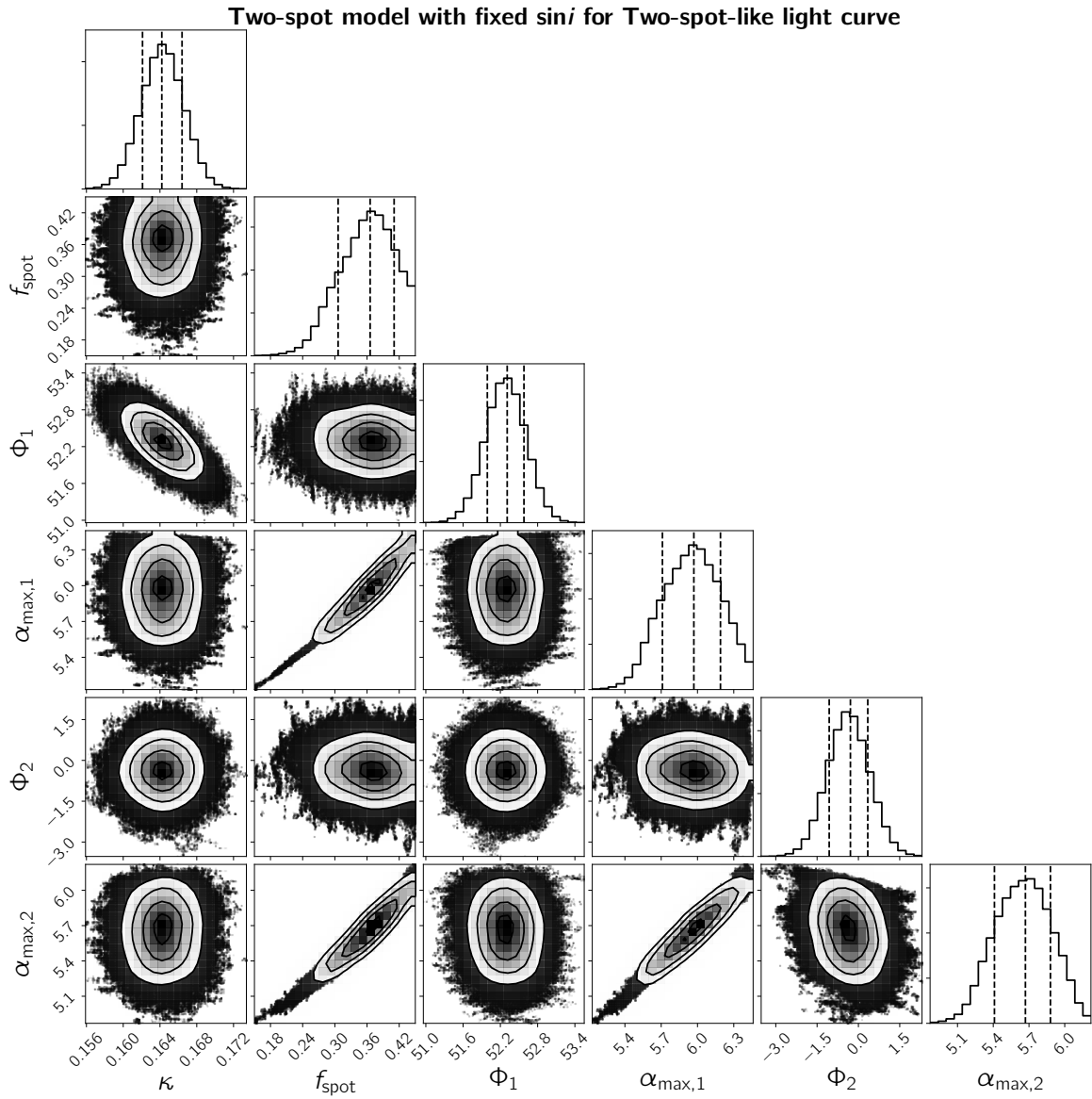
Figure 2.9: Same as Figure 2.7 but for the two-spot model with fixed $\sin i$.
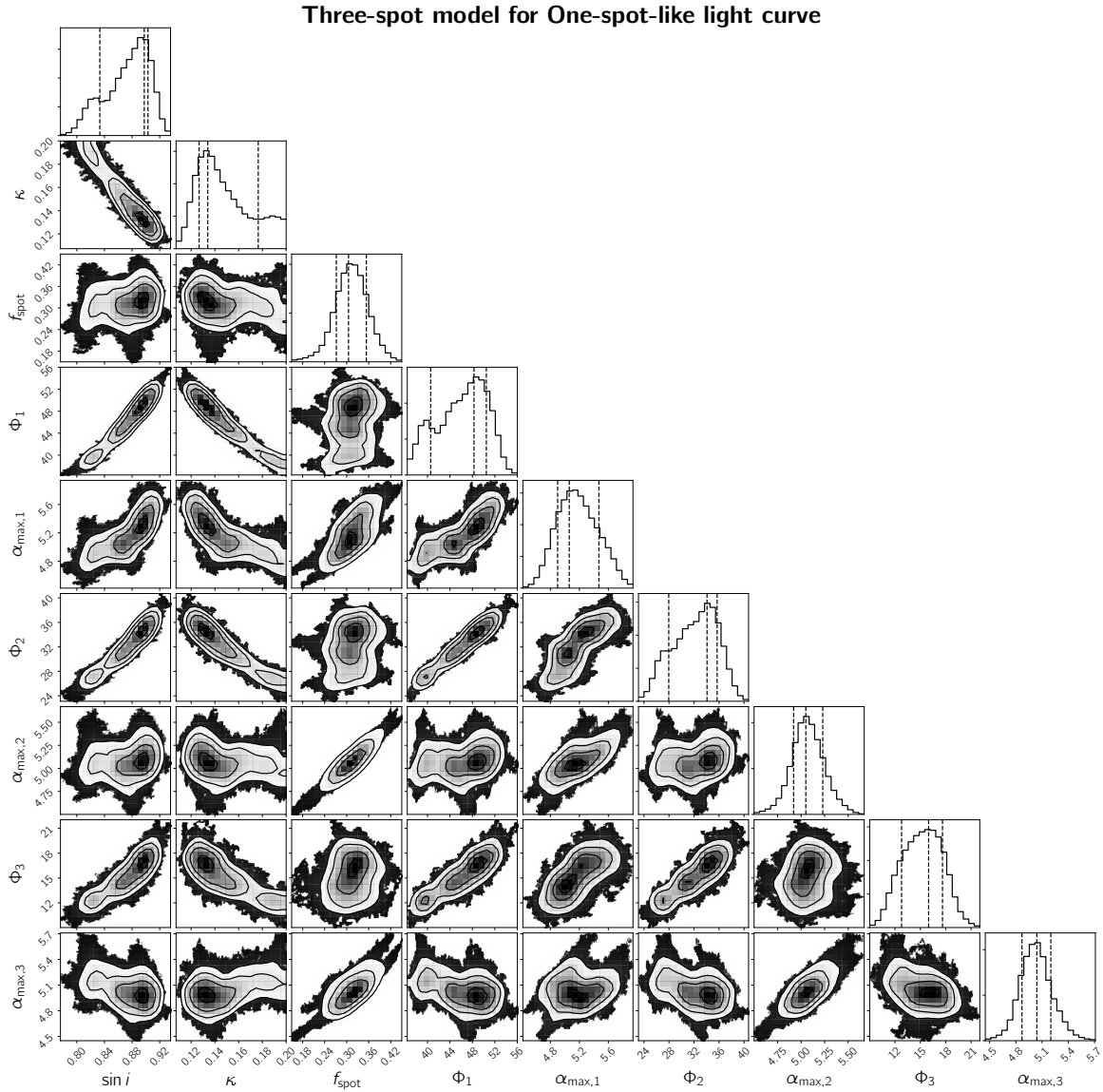
Figure 2.10: The joint posterior distribution of parameters with the degeneracies for one-spots-like light curve by the three-spot model. Each column represents the inclination angle $\sin i$, degree of differential rotation $\kappa$, relative intensity $f_{\mathrm{spot}}$, the maximum radius $\alpha_{\mathrm{max,k}}$, and latitude $\Phi_k$.

**Two-spot model for One-spot-like light curve**
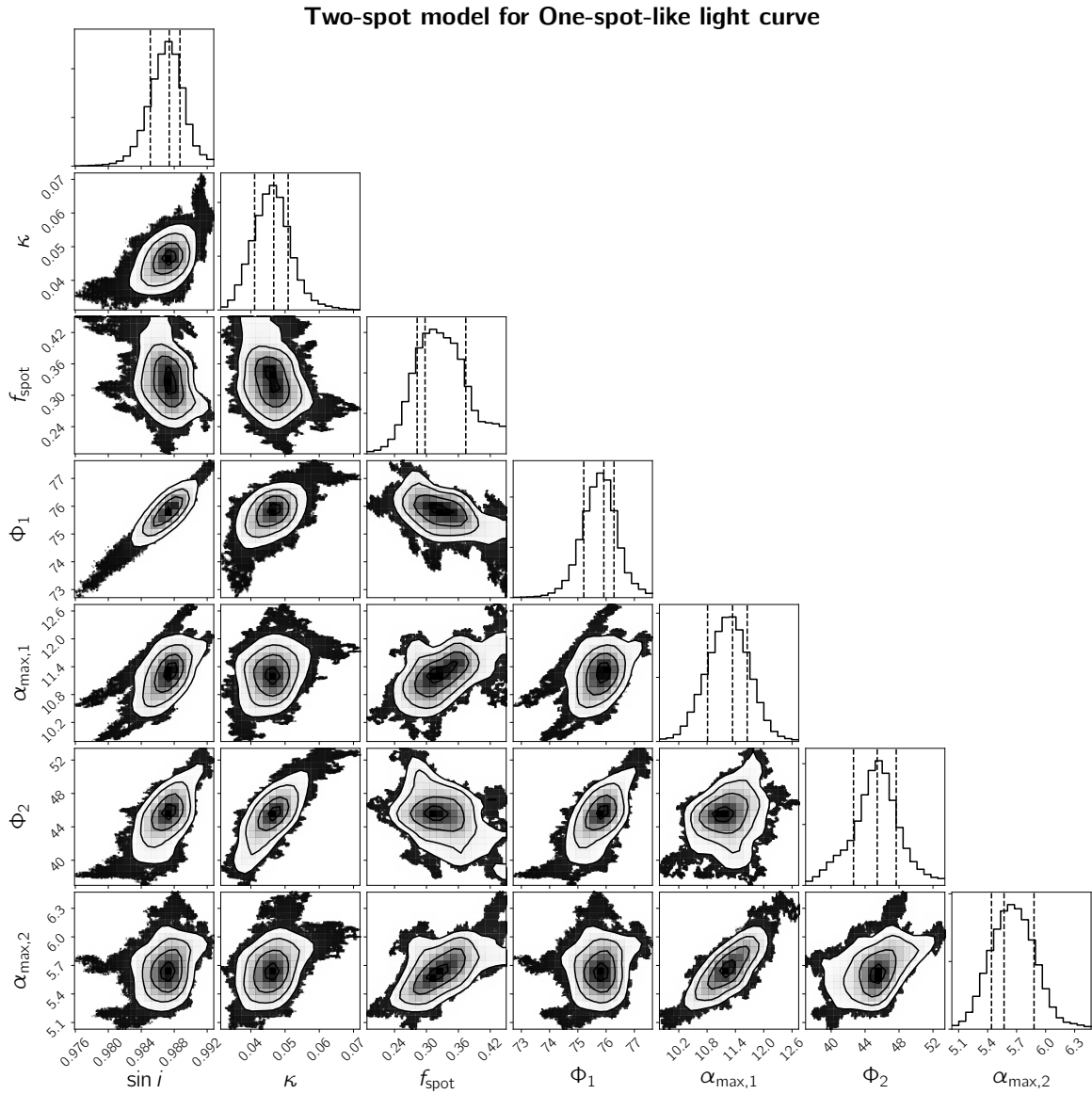


Figure 2.11: Same as Figure 2.10 but for the two-spot model.
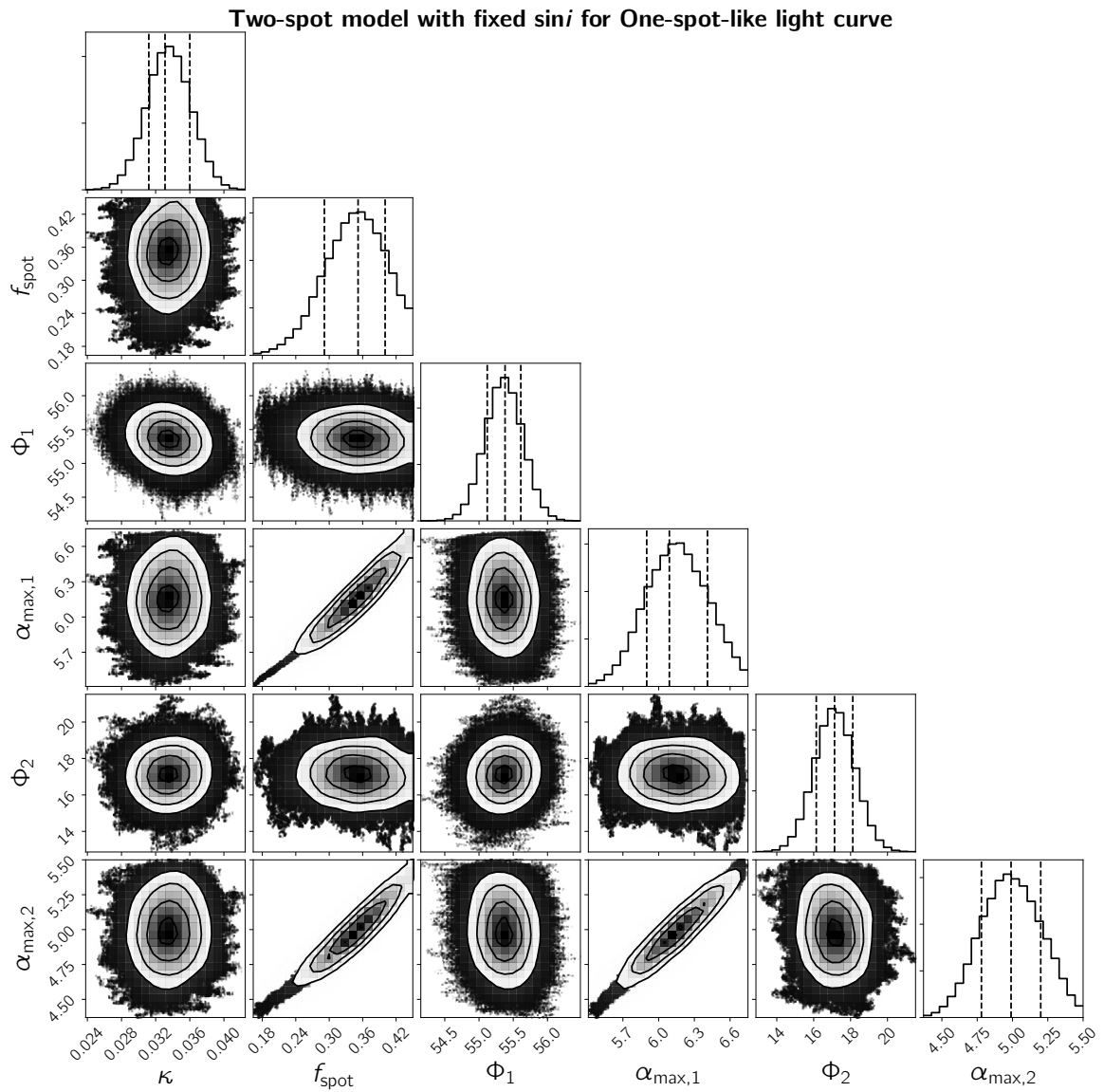
Figure 2.12: Same as Figure 2.10 but for the two-spot model with fixed $\sin i$.
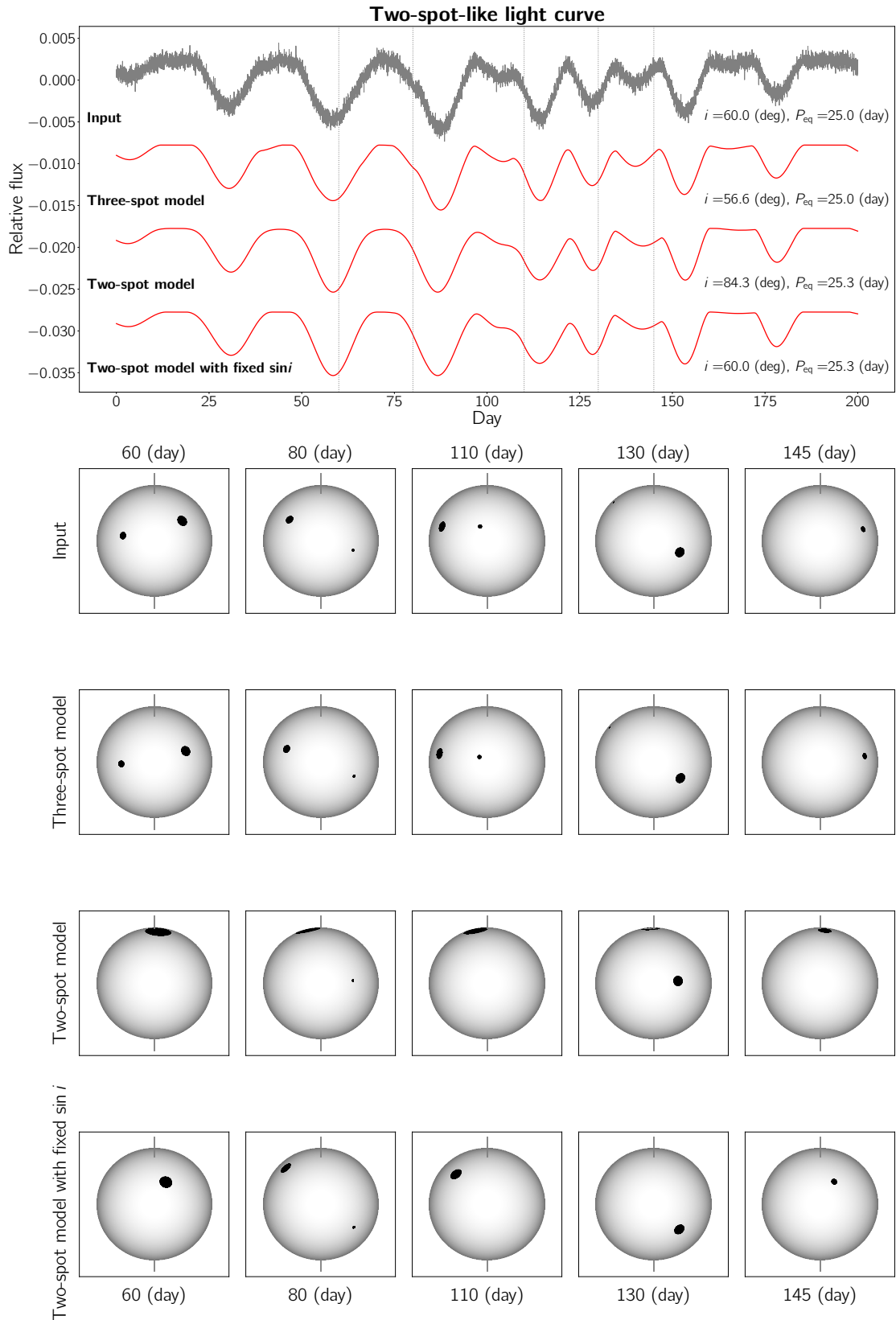
Figure 2.13: The input light curve (gray) and the ones reproduced by the optimum of each of the models (red) for the two-spot-like case. The values of the inclination angle and the equatorial period are also denoted for each of the models. The calculated spots on the stellar surface are visualized at five times (vertical dotted lines).
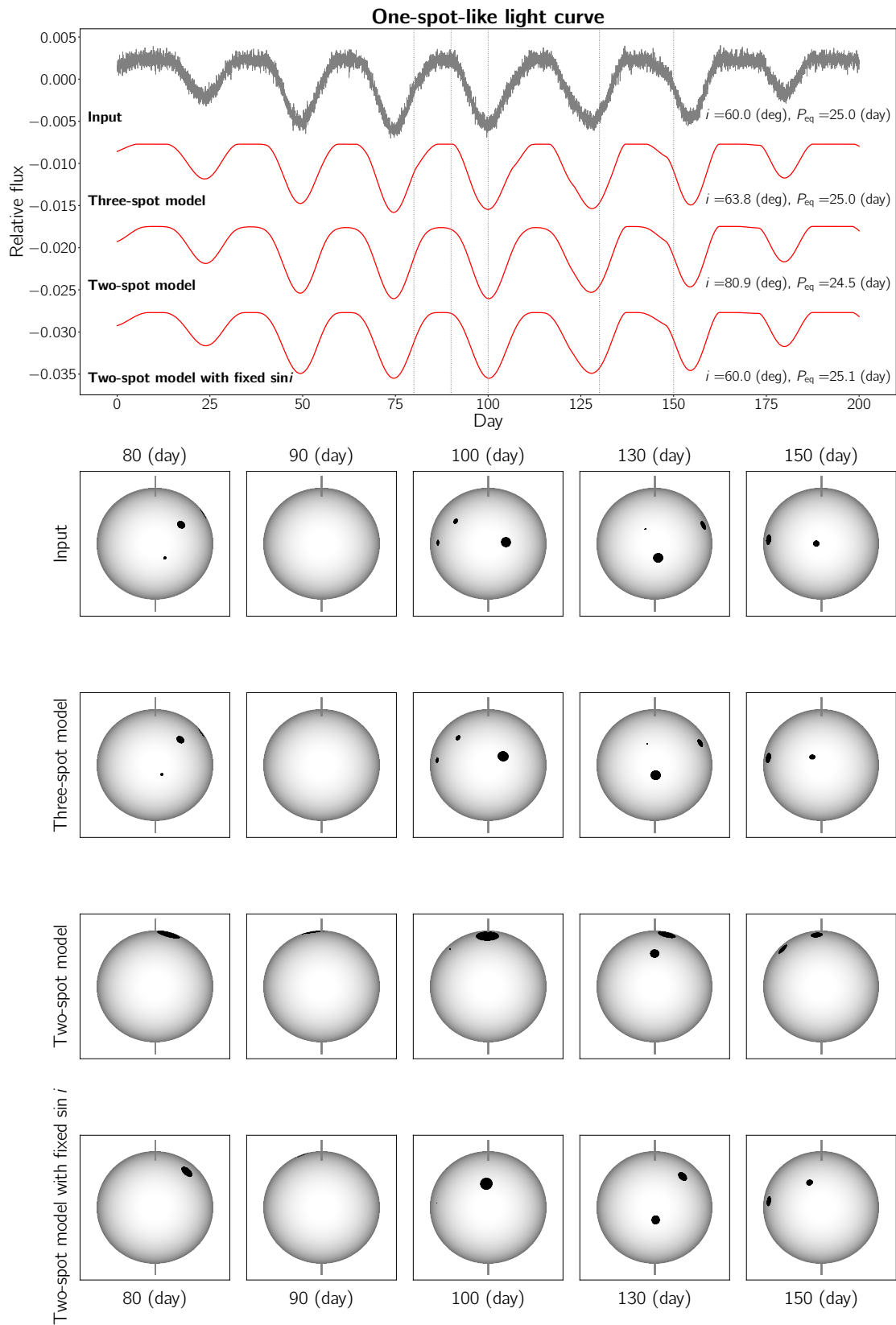
Figure 2.14: Same as Figure 2.13 but for the one-spot-like case.

# Chapter 3

# Starspot mapping with adaptive parallel tempering. II. Application to *TESS* data of M-dwarfs, AU Mic, EV Lac, and YZ CMi (Ikuta et al. 2021, in preparation)

## 3.1 Introduction

In this Section, we conduct starspot modeling for *TESS* light curves of renowned flare M-dwarfs, AU Mic, YZ CMi, and EV Lac, using the code implemented in Section 2 (Ikuta et al. 2020, hereinafter, referred to as Paper I). Concurrently, EV Lac and YZ CMi have been spectroscopically observed by the *Seimei* telescope in Kyoto University to investigate physical mechanisms of flares. AU Mic also have been followed up with observation by many stellar and exoplanetary researchers, including my collaborators because of harboring a exoplanet in the system. Therefore, it is meaningful to investigate spot properties of these three targets. The reminder of this Section is as follows. In Section 3.2, we describe the preprocessing of data and a numerical setup for the starspot modeling. In Section 3.3. we exhibit preliminary results in terms of comparing with the previous studies, determining the number of spots, and the validity of starspot modeling. In Section 3.4, we describe future

prospects to delve into comparing the previous photometric and Doppler Imaging studies and into the relation between spot parameters and flares detected in the light curves. In Section 3.5, we exhibit supplementary figures delineating the joint posterior distributions for each of the model.

Table 3.1: Stellar parameters

| Stellar parameter | YZ CMi | AU Mic | EV Lac |
|---|---|---|---|
| Effective temperature $T_{\mathrm{eff}}$ (K) | 3100 | 3700 | 3400 |
| Rotation period $P_{\mathrm{rot}}$ (day) | 2.776 | 4.863 | 4.376 |
| Surface gravity $\log g$ | 5.0 | 4.7 | 4.7 |
| Inclination angle $i$ (deg) | 36 | 75 | 85 |
| Reference | Baroch et al. (2020) | Martioli et al. (2020) | Morin et al. (2008) |
| Limb-darkening coefficients | (3.15, −4.62, | (2.87, −4.35, | (3.30, −5.15, |
| $(c_1, c_2, c_3, c_4)$ [a] | 4.01, −1.34) | 3.92, −1.32) | 4.55, −1.53) |
| Spot temperature $T_{\mathrm{spot}}$ (K)[b] | 2793 | 3097 | 2948 |
| Spot relative intensity $f_{\mathrm{spot}}$ [b] | 0.658 | 0.491 | 0.565 |

[a] The spot temperature is formulated by the stellar effective temperature (Maehara et al. 2017), and the spot relative intensity $f_{\mathrm{spot}}$ is given by $(T_{\mathrm{spot}}/T_{\mathrm{eff}})^4$.

[b] The stellar limb-darkening coefficients for *TESS* data in case of solar metalicity are listed in Claret (2018) and characterized by the effective temperature $T_{\mathrm{eff}}$ and surface gravity $\log g$.

## 3.2 Method

### 3.2.1 Dataset and preprocessing

YZ CMi and EV Lac were respectively observed in Sector 7 and 16 at 2-min cadence by *TESS* (Ricker et al. 2014). In addition, AU Mic was observed in Sector 1 and 27 with the interval of two *TESS* Cycle. We retrieve the PDC-SAP light curves from the MAST Portal webcite. We extract outliers of the modulations ascribed to spots from the light curves using low-pass filter with the cutoff frequency of $\sim 1/5.00$ day$^{-1}$ to conduct starspot modeling because many flares are observed in the light curves of the active stars (see Maehara et al. 2020, for YZ CMi). Nevertheless small flares remain in the light curves, but they do not affect the result of the starspot modeling since the number of the flare data points is much fewer than the that of total data points. In this study, since the modulation timescale ascribed to spots is much longer than

the cadence, we use a data point per 3 points ("6-min cadence") for computational efficiency.

## 3.2.2 Numerical setup

The stellar parameters and their references are described in Table 3.1 for conducting starspot modeling of AU Mic, EV Lac, and YZ CMi. Then, the stellar limb-darkening low is adopted as the following representation:

$$I(\mu)/I(1) = 1 - \Sigma_{k=1}^{4} c_k (1 - \mu^{k/2}), \tag{3.1}$$

and the coefficients based on the stellar parameters are deduced from Claret (2018). In an analytical spotted model (Kipping 2012), the spot parameters of the reference time $t_p$, emergence duration $\mathcal{I}$, decay duration $\mathcal{E}$, and stable duration $\mathcal{L}$ are thought to be unnecessary because the amplitudes of the light curves are approximately constant in a *TESS* Sector ($\sim 27$ days). Therefore, the light curves are specified in less stellar and spot parameters than those used in Paper I for simplicity (Table 3.2, 3.3, and 3.4). In fact, we ascertain that the posterior distribution do not converge to an unimodal distribution due to these unnecessary parameters by exploiting the test runs. Each of the spot is labeled by the range of the latitude, unlike the range of the reference time in Paper I.

The light curve of YZ CMi exhibits one-spot-like, and we optimized it by one-spot model and two-spot model (Table 3.2). As for one-spot model, the differential rotation parameter $\kappa$ is fixed to 0. Moreover, the light curves of AU Mic and EV Lac exhibit two-spot-like, and we optimized it by two-spot model and three-spot model (Table 3.3, 3.4). We note that the light curve of YZ CMi is one-spot-like possibly due to its low inclination angle (e.g., Basri and Shah 2020). We ascertained the posterior distributions of the inclination angle and spot intensity converge to unphysical modes (the edges of the parameter domain) by exploting test run because they respectively have degeneracies with the spot latitude and size as reported in Paper I. Therefore, the values of the inclination angle and spot intensity are fixed the value denoted in Table 3.1. In addition, we abbreviate the name followed by Paper I for each of the model: for instance, "three-spot model fixed $\sin i$ and $\kappa$" in the context of Paper I is simply renamed "three-spot model" thereafter.

Table 3.2: AU Mic case

| Deduced parameters | Two-spot model | Three-spot model | Prior distribution[a] |
|---|---|---|---|
| **(Stellar parameters)** | | | |
| 1. Equatorial period $P_{\mathrm{eq}}$ (day) | $4.8622^{+0.0000}_{-0.0005}$ | $4.8110^{+0.0005}_{-0.0010}$ | $\mathcal{U}_{\mathrm{log}}(4.0000, 5.5000)$ |
| 2. Degree of differential rotation $\kappa$ | $-0.0001^{+0.0001}_{-0.0002}$ | $0.1990^{+0.0009}_{-0.0012}$ | $\mathcal{U}(-0.2000, 0.2000)$ |
| **(Spot parameters)** | | | |
| (1st spot) | | | |
| 3. Latitude $\Phi_1$ (deg) | $-13.79^{+0.11}_{-0.12}$ | $-14.43^{+0.10}_{-0.10}$ | $\mathcal{U}(-90.00, \Phi_2)^{\mathrm{b}}$ |
| 4. Initial longitude $\Lambda_1$ (deg) | $-22.93^{+0.01}_{-0.04}$ | $-134.37^{+0.05}_{-0.07}$ | $\mathcal{U}(-180.00, 180.00)$ |
| 5. Maximum radius $\alpha_{\mathrm{max},1}$ (deg) | $16.61^{+0.01}_{-0.01}$ | $13.77^{+0.01}_{-0.02}$ | $\mathcal{U}(0.01, 20.00)$ |
| (2nd spot) | | | |
| 6. Latitude $\Phi_2$ (deg) | $39.18^{+0.07}_{-0.08}$ | $11.70^{+0.14}_{-0.10}$ | $\mathcal{U}(\Phi_1, \Phi_3)^{\mathrm{b}}$ |
| 7. Initial longitude $\Lambda_2$ (deg) | $-152.56^{+0.01}_{-0.03}$ | $178.61^{+0.08}_{-0.12}$ | $\mathcal{U}(-180.00, 180.00)$ |
| 8. Maximum radius $\alpha_{\mathrm{max},2}$ (deg) | $16.99^{+0.01}_{-0.01}$ | $11.47^{+0.01}_{-0.02}$ | $\mathcal{U}(0.01, 20.00)$ |
| (3rd spot) | | | |
| 9. Latitude $\Phi_3$ (deg) | - | $13.6^{+0.14}_{-0.06}$ | $\mathcal{U}(\Phi_2, 90.00)^{\mathrm{b}}$ |
| 10. Initial longitude $\Lambda_3$ (deg) | - | $-24.21^{+0.01}_{-0.03}$ | $\mathcal{U}(-180.00, 180.00)$ |
| 11. Maximum radius $\alpha_{\mathrm{max},3}$ (deg) | - | $15.38^{+0.01}_{-0.01}$ | $\mathcal{U}(0.01, 20.00)$ |
| Model evidence $\log \mathcal{Z}$ | -63316.025 | -41037.879 | |

[a] $\mathcal{U}_{\mathrm{log}}(a, b) = \log \theta / \log(b/a)$ and $\mathcal{U}(a, b) = 1/(b - a)$ represent bounded log-uniform distribution (Jeffey's prior) and bounded uniform distribution defined in $a \leq \theta \leq b$, respectively.

[b] We discern each spot by its latitude $\Phi_k$, not by its reference time $t_k$ in Ikuta et al. (2020), to improve the sampling efficiency of the PT. In case of the two-spot model, we set $\Phi_3 = 90.0$ (the upper limit of the latitude).

Table 3.3: EV Lac case

| Deduced parameters | Two-spot model | Three-spot model | Prior distribution[a] |
|---|---|---|---|
| **(Stellar parameters)** | | | |
| 1. Equatorial period $P_{\mathrm{eq}}$ (day) | $4.2110^{+0.0105}_{-0.0382}$ | $4.4053^{+0.0009}_{-0.0018}$ | $\mathcal{U}_{\log}(4.0000, 5.5000)$ |
| 2. Degree of differential rotation $\kappa$ | $0.0419^{+0.0102}_{-0.0034}$ | $-0.0128^{+0.0002}_{-0.0005}$ | $\mathcal{U}(-0.2000, 0.2000)$ |
| **(Spot parameters)** | | | |
| (1st spot) | | | |
| 3. Latitude $\Phi_1$ (deg) | $63.48^{+0.25}_{-0.21}$ | $-64.02^{+0.09}_{-0.13}$ | $\mathcal{U}(-90.00, \Phi_2)$[b] |
| 4. Initial longitude $\Lambda_1$ (deg) | $51.54^{+0.25}_{-0.19}$ | $91.68^{+0.21}_{-0.31}$ | $\mathcal{U}(-180.00, 180.00)$ |
| 5. Maximum radius $\alpha_{\mathrm{max},1}$ (deg) | $21.97^{+0.16}_{-0.11}$ | $27.10^{+0.34}_{-0.13}$ | $\mathcal{U}(0.01, 30.00)$ |
| (2nd spot) | | | |
| 6. Latitude $\Phi_2$ (deg) | $66.03^{+0.39}_{-0.16}$ | $58.75^{+0.25}_{-0.20}$ | $\mathcal{U}(\Phi_1, \Phi_3)$[b] |
| 7. Initial longitude $\Lambda_2$ (deg) | $-88.83^{+0.19}_{-0.20}$ | $-119.26^{+0.25}_{-0.28}$ | $\mathcal{U}(-180.00, 180.00)$ |
| 8. Maximum radius $\alpha_{\mathrm{max},2}$ (deg) | $22.16^{+0.23}_{-0.13}$ | $21.98^{+0.18}_{-0.25}$ | $\mathcal{U}(0.01, 30.00)$ |
| (3rd spot) | | | |
| 9. Latitude $\Phi_3$ (deg) | - | $72.33^{+0.23}_{-0.21}$ | $\mathcal{U}(\Phi_2, 90.00)$[b] |
| 10. Initial longitude $\Lambda_3$ (deg) | - | $-5.95^{+0.51}_{-0.56}$ | $\mathcal{U}(-180.00, 180.00)$ |
| 11. Maximum radius $\alpha_{\mathrm{max},3}$ (deg) | - | $29.93^{+0.05}_{-0.08}$ | $\mathcal{U}(0.01, 30.00)$ |
| Model evidence $\log \mathcal{Z}$ | -9317.863 | -5378.769 | |

[a] $\mathcal{U}_{\log}(a, b) = \log \theta / \log(b/a)$ and $\mathcal{U}(a, b) = 1/(b - a)$ represent bounded log-uniform distribution (Jeffey's prior) and bounded uniform distribution defined in $a \leq \theta \leq b$, respectively.

[b] We discern each spot by its latitude $\Phi_k$, not by its reference time $t_k$ in Ikuta et al. (2020), to improve the sampling efficiency of the PT. In case of the two-spot model, we set $\Phi_3 = 90.0$ (the upper limit of the latitude).

Table 3.4: YZ CMi case

| Deduced parameters | One-spot model | Two-spot model | Prior distribution[a] |
|---|---|---|---|
| **(Stellar parameters)** | | | |
| 1. Equatorial period $P_{eq}$ (day) | $2.7735^{+0.0003}_{-0.0003}$ | $2.7749^{+0.0003}_{-0.0003}$ | $\mathcal{U}_{\log}(2.0000, 3.5000)$ |
| 2. Degree of differential rotation $\kappa$ | $0.0000$ (*fixed*) | $-0.0007^{+0.0001}_{-0.0003}$ | $\mathcal{U}(-0.2000, 0.2000)$ |
| **(Spot parameters)** | | | |
| (1st spot) | | | |
| 3. Latitude $\Phi_1$ (deg) | $75.34^{+0.01}_{-0.01}$ | $-7.43^{+0.29}_{-0.18}$ | $\mathcal{U}(-90.00, \Phi_2)$[b] |
| 4. Initial longitude $\Lambda_1$ (deg) | $31.3^{+0.05}_{-0.06}$ | $113.33^{+0.23}_{-0.2}$ | $\mathcal{U}(-180.00, 180.00)$ |
| 5. Maximum radius $\alpha_{\max,1}$ (deg) | $29.98^{+0.01}_{-0.01}$ | $14.88^{+0.10}_{-0.11}$ | $\mathcal{U}(0.01, 30.00)$ |
| (2nd spot) | | | |
| 6. Latitude $\Phi_2$ (deg) | - | $41.53^{+0.35}_{-0.30}$ | $\mathcal{U}(\Phi_1, 90.00)$[b] |
| 7. Initial longitude $\Lambda_2$ (deg) | - | $17.03^{+0.18}_{-0.14}$ | $\mathcal{U}(-180.00, 180.00)$ |
| 8. Maximum radius $\alpha_{\max,2}$ (deg) | - | $18.31^{+0.01}_{-0.03}$ | $\mathcal{U}(0.01, 30.00)$ |
| Model evidence $\log \mathcal{Z}$ | 2767.723 | 15020.281 | |

[a] $\mathcal{U}_{\log}(a,b) = \log \theta / \log(b/a)$ and $\mathcal{U}(a,b) = 1/(b-a)$ represent bounded log-uniform distribution (Jeffey's prior) and bounded uniform distribution defined in $a \leq \theta \leq b$, respectively.

[b] We discern each spot by its latitude $\Phi_k$, not by its reference time $t_k$ in Ikuta et al. (2020), to improve the sampling efficiency of the PT. In case of the one-spot model, we set $\Phi_2 = 90.0$ (the upper limit of the latitude).

# 3.3 Result and discussion

We optimize the light curves of AU Mic and EV Lac by the three-spot model and two-spot model and the one of YZ CMi by the two-spot model and one-spot model. In each of the case, unimodal posterior distributions are deduced, and the joint posterior distributions are delineated in Section 3.5. Table 3.2, 3.3, and 3.4 show the modes of the deduced posterior distributions, their credible regions, and the model evidence for each model, together with their prior distributions for each of the parameter. Figure 3.1 and 3.2, 3.3 and 3.4, and 3.5 and 3.6 show the resultant cases of AU Mic, EV Lac, YZ CMi, respectively: (a) the *TESS* light curve (gray), that are reproduced with each mode of the deduced unimodal posterior distribution (red), and their residuals (black); and (b) The maximum radius for each of the model (red, blue, and green), respectively.

The calculated spots on the stellar surface and the light curves are visualized in Figure 3.7 and 3.8.

### 3.3.1   Comparing with the previous studies

**AU Mic**

The light curve of AU Mic in Sector 1 was conducted starspot modeling with two spots (Wisniewski et al. 2019) utilizing `STSP` code (Davenport et al. 2015). Their result show the values of the latitude are $44.8°$ and $9.6°$, although ours are $37.3°$ and $-14.5°$. This slight difference is due to the spot relative intensity and the size, and ours is deduced to 0.63, whereas theirs is fixed 0.7 because there are degeneracies between the spot latitude and size (Paper I). AU Mic have been investigated the magnetic fields by Zeeman Doppler Imaging (Martioli et al. 2020; Kochukhov and Reiners 2020; Klein et al. 2020). Their result show AU Mic have strong magnetic fields to the line of sight and is almost consistent with our results.

**EV Lac**

EV Lac have been investigated the magnetic fields by Zeeman Doppler Imaging (Morin et al. 2008). Their result show AU Mic have strong magnetic fields on the visible pole and near the equator and is almost consistent with our results.

**YZ CMi**

The light curve of YZ CMi obtained by ground-based observations and also conducted simple starspot modeling in the form of sinusoidal (Zboril 2003). In addition, the magnetic fields on YZ CMi was also investigated by Zeeman Doppler Imaging (Morin et al. 2008). These results are consistent with our result in that strong magnetic fields are near the visible pole, and the magnetic fields remain for more than a decade.

### 3.3.2   How many spots exist?

The light curves seem to be two-spot-like or one-spot-like, but not two spots or one spot is actually present on the stellar surface. Then, as well as Paper I, we determine the number of spots based on the model selection, comparing the value of model evidence(Kass and Raftery 1995). The values of the model evidence $\log \mathcal{Z}$ for AU Mic,

EV Lac, and YZ CMi are listed in Table 3.2, 3.3, and 3.4, respectively. In both cases of AU Mic and EV Lac, the three-spot model is much more decisive than the two-spot model by orders of magnitude: the evidences of the three-spot model relative to that of the two-spot model are $\Delta \log \mathcal{Z} = 22278.146$ and $3939.094$, respectively. In the case of YZ CMi, the two-spot model is much more decisive than the one-spot model by orders of magnitude: the evidence of the two-spot model relative to that of the one-spot model is $\Delta \log \mathcal{Z} = 12252.558$.

In all cases, it is suggested that each of the model with one more spot is preferable, and it is uncertain whether the number of spots can be correctly determined or not in the Bayesian framework. Therefore, it is absolutely essential to utilize more sophisticated method as mentioned in Section 3.3.3 and conduct spectroscopic observation of the targets for Doppler Imaging, concurrent with the photometry.

### 3.3.3    Validity of starspot modeling

The light curves are two-spot-like or one-spot-like produced any number of spots (Basri and Nguyen 2018; Basri 2018), and we qualitatively investigated the two-spot-like and one-spot-like synthetic light curves produced three spots (Paper I). Basri and Shah (2020) qualitatively examined to what extent properties can be deduced from the light curve, and we need to pay considerable attention to the interpretation of the properties from the light curve. It is usually impossible to determine how many spots are actually present on the stellar surface from only light curve. We can compare the number of spots by computing the model evidence only in the Bayesian framework. However, as described in Basri and Shah (2020), it is necessary to investigate the effect of the number of spots to the structures of light curve using machine learning method, such as deep convolutional neural networks (e.g., Shallue and Vanderburg 2018). It is also necessary to observe spotted stars in multi-band wavelengths to elucidate the active regions (Toriumi et al. 2020).

## 3.4    Future prospects

**Relation between spot location and flare**

We intend to investigate the relation between spot location and flares by detecting

flares from each of the light curve, such as whether spots causing flares are located near the stellar equator or pole, as in Maehara et al. (2020).

**Long-term variation of the light curve structure**

A flare M-dwarf GJ 1243 was observed by *Kepler* prime mission ($\sim$1500 days from 2009 to 2013) and *TESS* Sector 14, 15 ($\sim$50 days in mid-2019). Davenport et al. (2020) investigated the phase variation of the photometric modulation for a decade due to the stellar differential rotation. Similarly, we intend to investigate the structure variation of the light curves for AU Mic, EV Lac, and YZ CMi by delving into the past ones.

**Comparing with results by Doppler Imaging**

These bright stars have been investigated their magnetic structures by the Zeeman Doppler Imaging (Klein et al. 2020). We intend to compare their results with our results of the starspot modeling obtained only by the photometry.

**Additional Data of AU Mic in *TESS* Cycle 3 (Sector 27)**

As mentioned in Section 3.2.1, AU Mic was observed in Sector 1 and 27 with the interval of two *TESS* Cycle. We exhibit only the result of the light curve of Sector 1 in Section 3.3. We also conducted starspot modeling of the light curve in Sector 27 as well as that in Sector 1, but the PT sampling did not converged due to the amplitude variation (in other words, spot radius is not stable) during the observation (Figure 3.10). Therefore, it is necessary to include spot emergence and decay parameters to conduct starspot modeling of the light curve in Sector 27 as in Section 2. Then, it could become possible to investigate the variations of spot size and location for two years, similar to Davenport et al. (2020).

**Utilizing *TESS* Full Flame Images**

As described in Section , unspotted level of the spotted stars is unknown (e.g., Basri 2018). Therefore, we also need to conduct starspot modeling for data of *TESS* Full Flame Images (FFIs; 30-minutes cadence). The FFIs enable to conduct photometry on any target within the 24$\times$96 degree field-of-view, and to make the unspotted level evaluated.

**Comparing with optical and X-ray spectrum**

EV Lac have been spectroscopically observed in optical (including Balmer lines)

and X-ray wavelength (e.g., Honda et al. 2018). Then, these data enable to compare the result of starspot modeling for the photometry in terms of investigating an active regions in multi-band wavelength (Toriumi et al. 2020).

In addition to the above-mentioned future works described, my approach is significant in the following perspectives: light curves of solar-type flare stars are so complicated due to many starspots on the stellar surface, and my approach enables to conduct starspot modeling with many spot parameters. In particular, it could be effective to Sun-like stars which are not able to be resolved their magnetic fields with Zeeman Doppler Imaging technique.

## 3.5   Appendix

The joint posterior distributions of the equatorial period, degree of differential rotation, latitude, longitude, and radius are delineated in Figure 3.11 and 3.12 for AU Mic, Figure 3.13 and 3.14 for EV Lac, and 3.15 and 3.16 for YZ CMi, generated using open software `corner` (Foreman-Mackey 2016). It is shown that they are converged to an unimodal distribution.

Figure 3.1: (a) *TESS* light curve of AU Mic (gray), those reproduced with each mode of the deduced unimodal posterior distribution for the two-spot model (red), and their residuals (black). (b) The maximum radius for the two-spot model (red and blue).
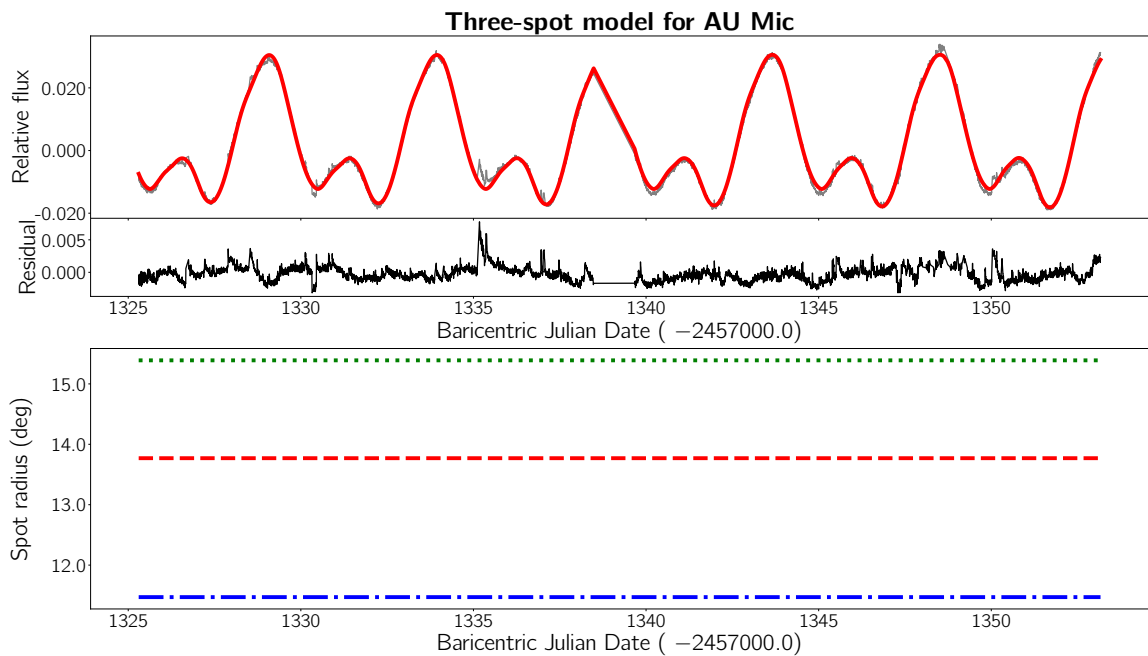


Figure 3.2: Same as Figure 3.1 but for the three-spot model.

Starspot mapping with adaptive parallel tempering. II. Application to *TESS* data of

**60** M-dwarfs, AU Mic, EV Lac, and YZ CMi (Ikuta et al. 2021, in preparation)
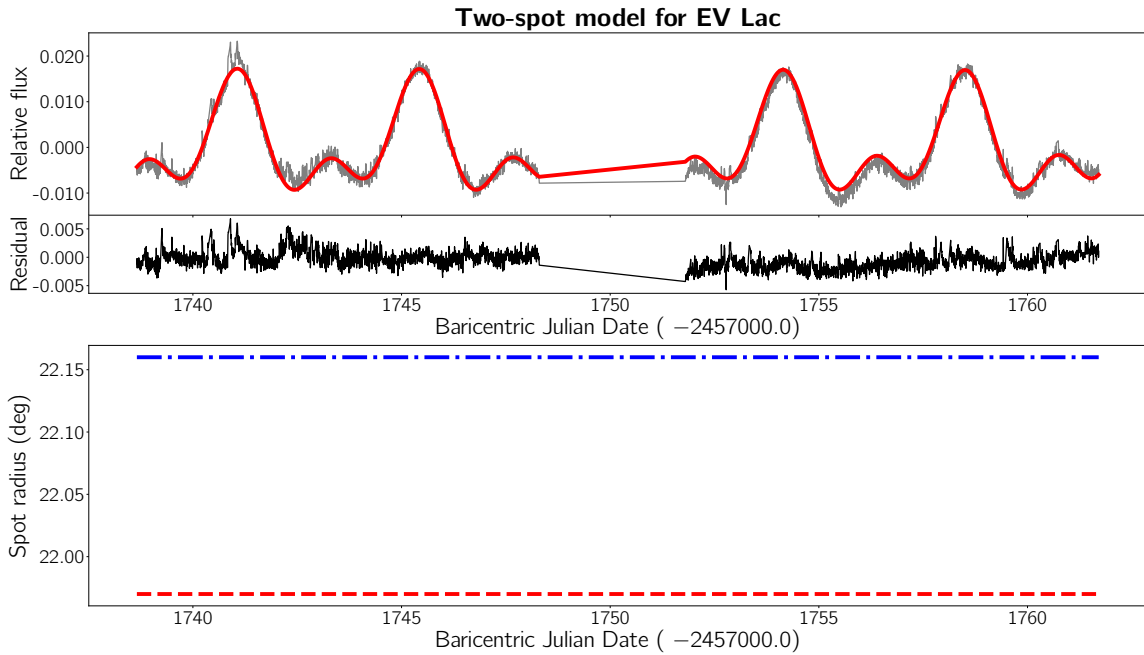


Figure 3.3: (a) *TESS* light curve of EV Lac (gray), those reproduced with each mode of the deduced unimodal posterior distribution for the two-spot model (red), and their residuals (black). (b) The maximum radius for the two-spot model (red and blue).



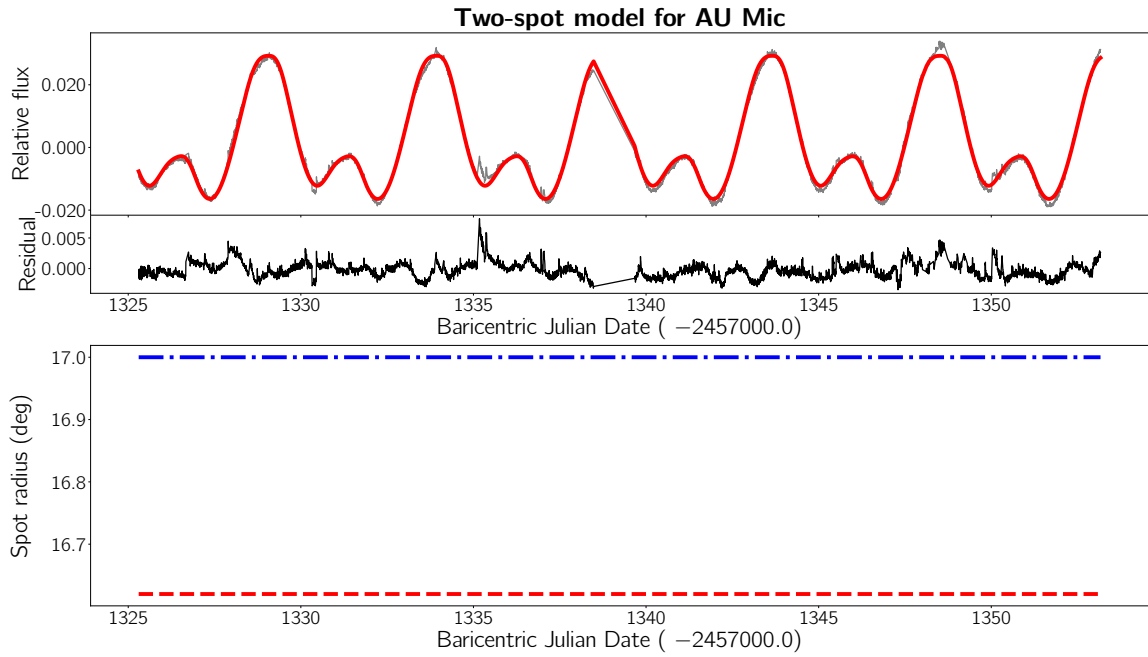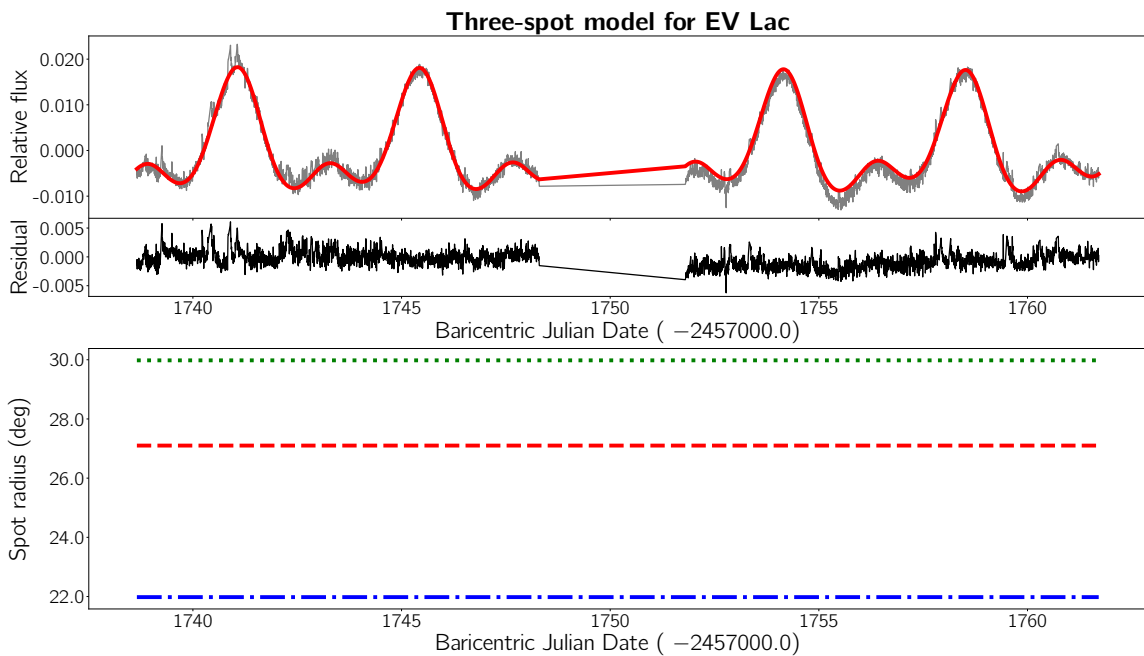Figure 3.4: Same as Figure 3.3 but for the three-spot model.
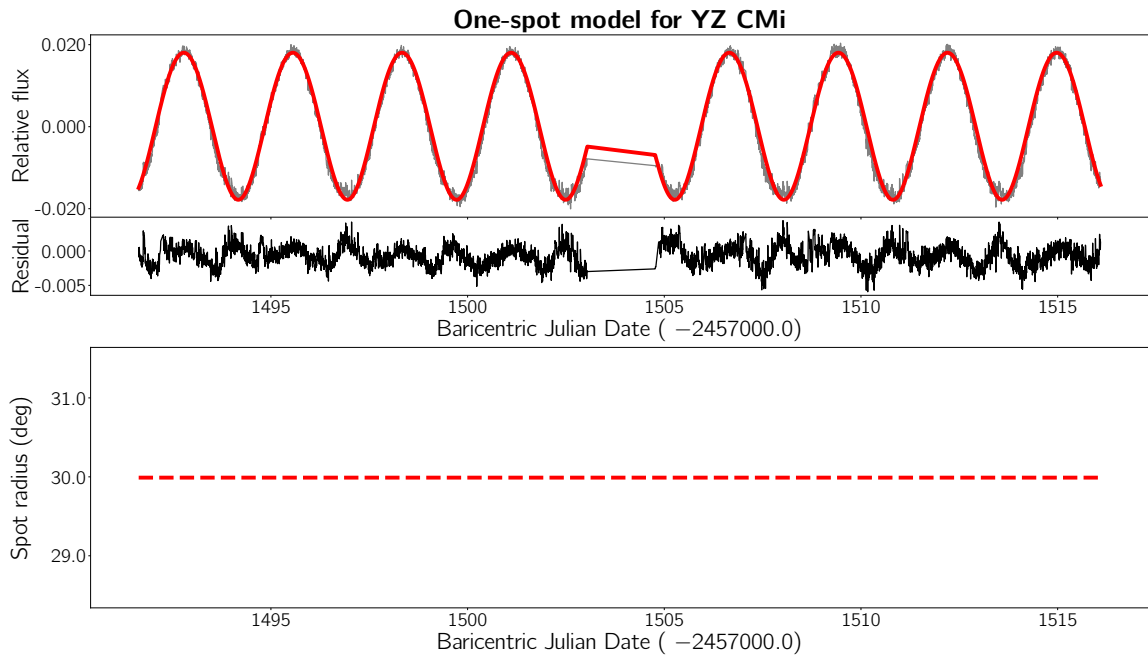
Figure 3.5: (a) *TESS* light curve of YZ CMi (gray), those reproduced with each mode of the deduced unimodal posterior distribution for the one-spot model (red), and their residuals (black). (b) The maximum radius for the one-spot model (red).
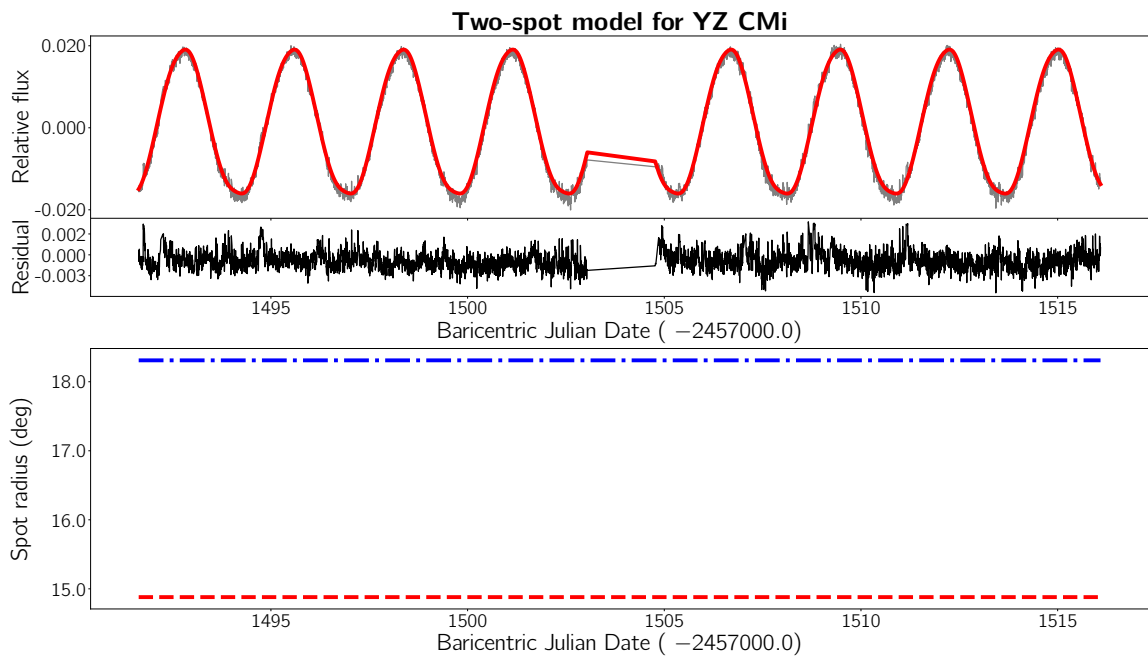


Figure 3.6: Same as Figure 3.5 but for the two-spot model.
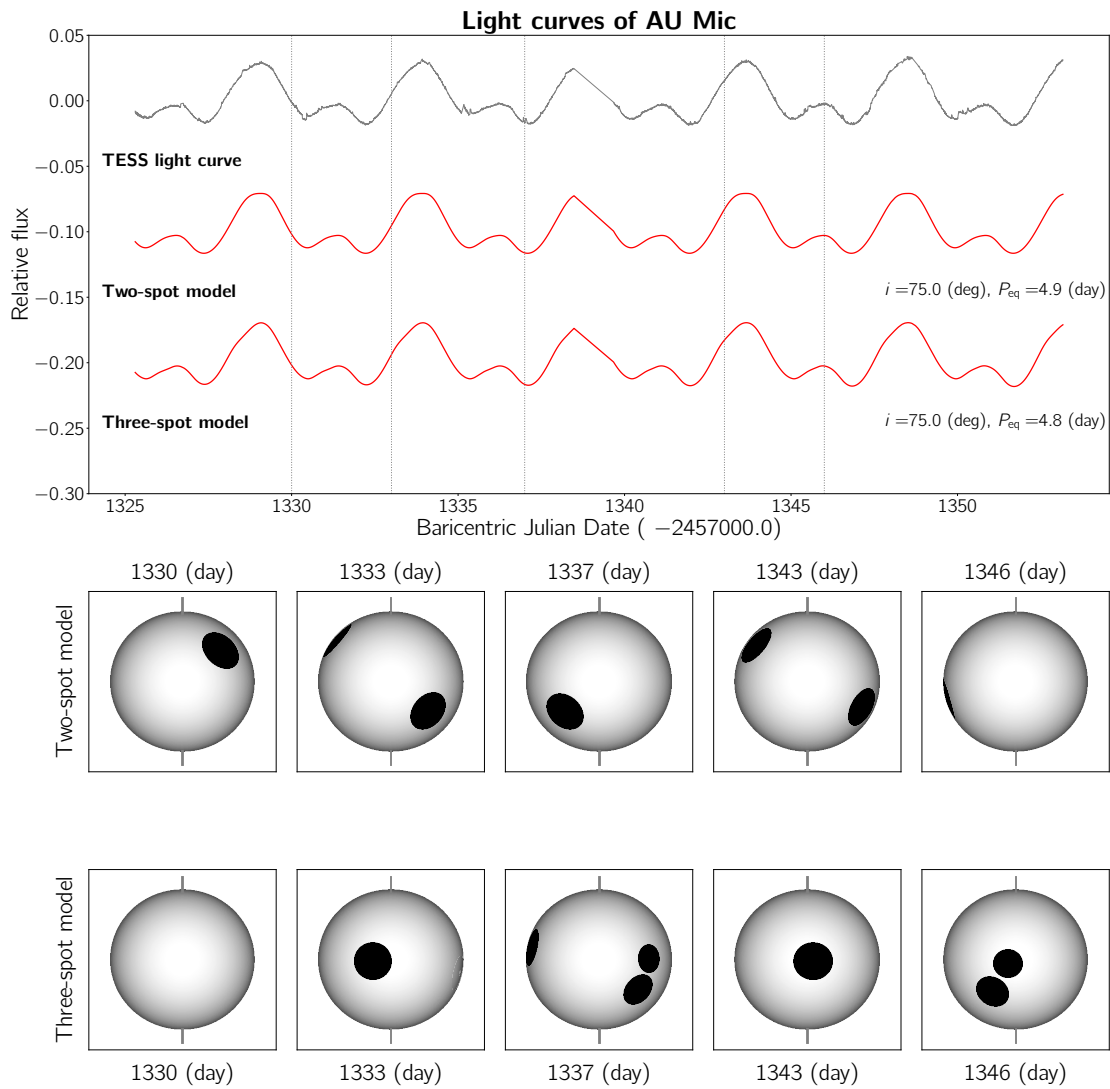
Figure 3.7: The light curves reproduced by the optimum of each of the model for AU Mic case (red). The values of the equatorial period are also denoted for each of the model. The calculated spots on the stellar surface are visualized at five times (vertical dotted lines).
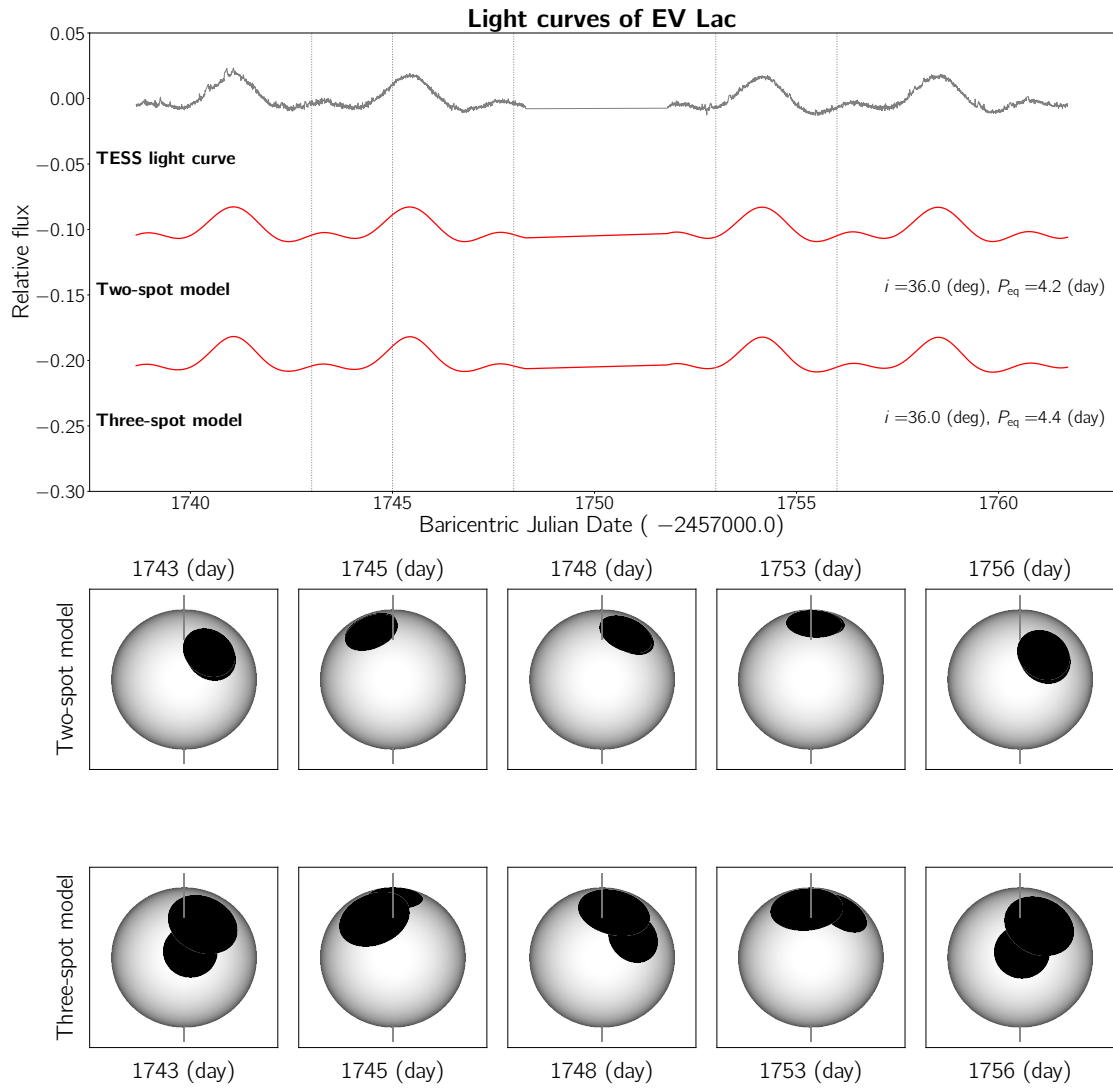
Figure 3.8: Same as Figure 3.7 but for EV Lac case.
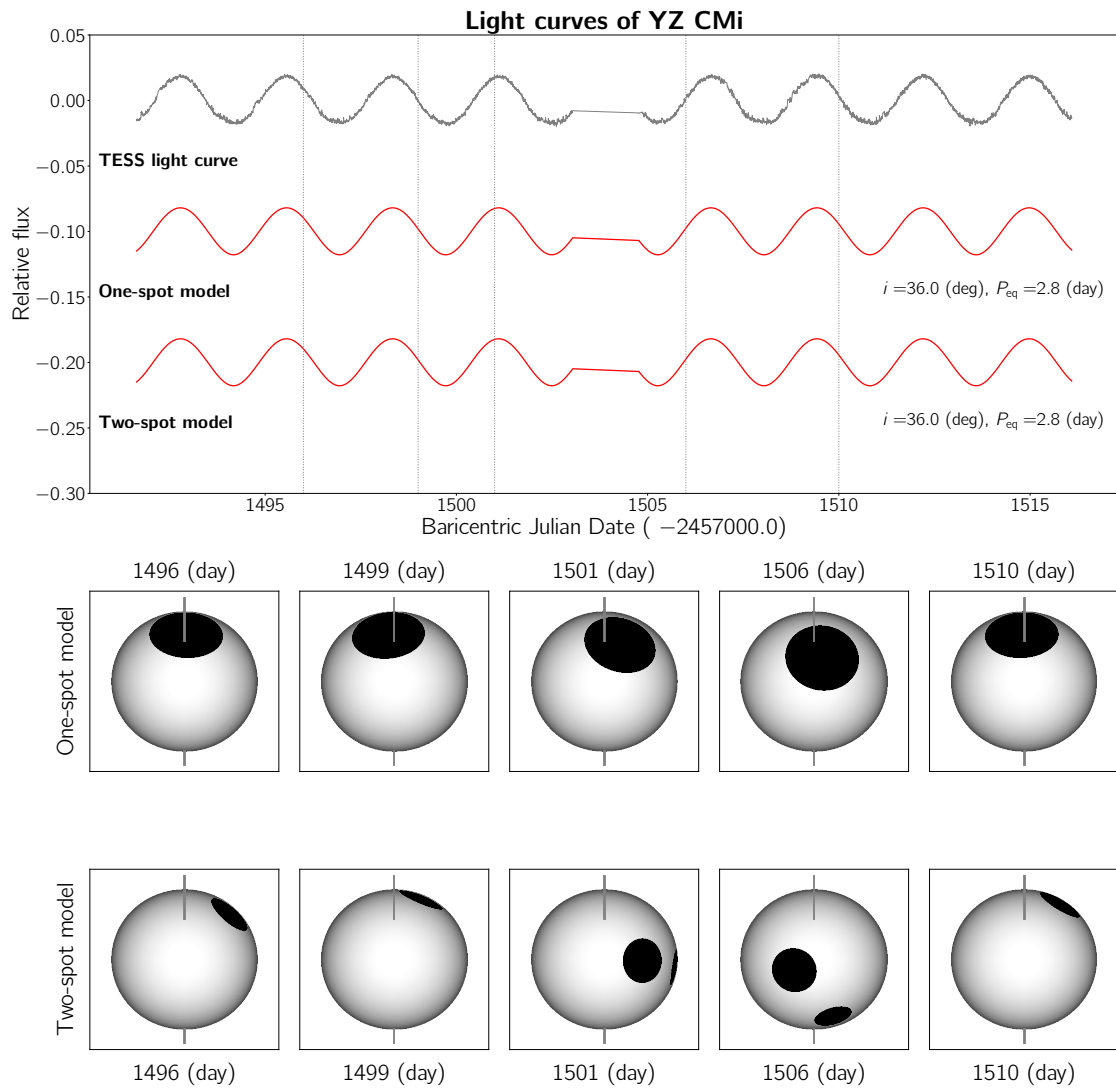
Figure 3.9: Same as Figure 3.7 but for YZ CMi case.
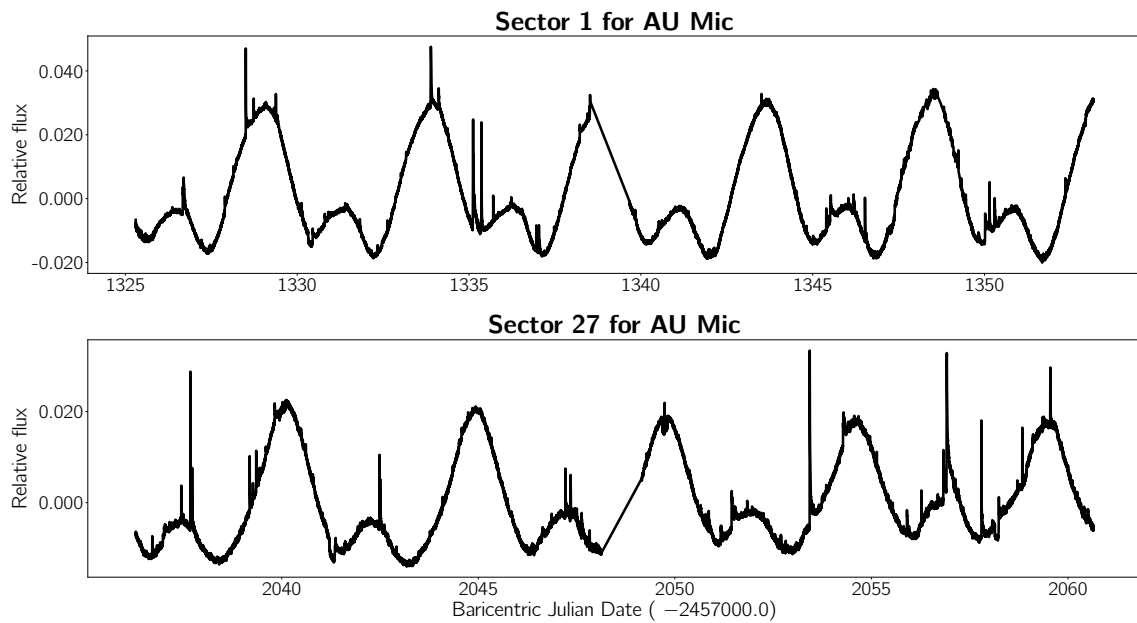
Figure 3.10: The PDC-SAP light curve of AU Mic in *TESS* Sector 1 (top) and 27 (bottom). The amplitude of that in Sector 27 varies during the observation possibly due to emerging or decaying spots.
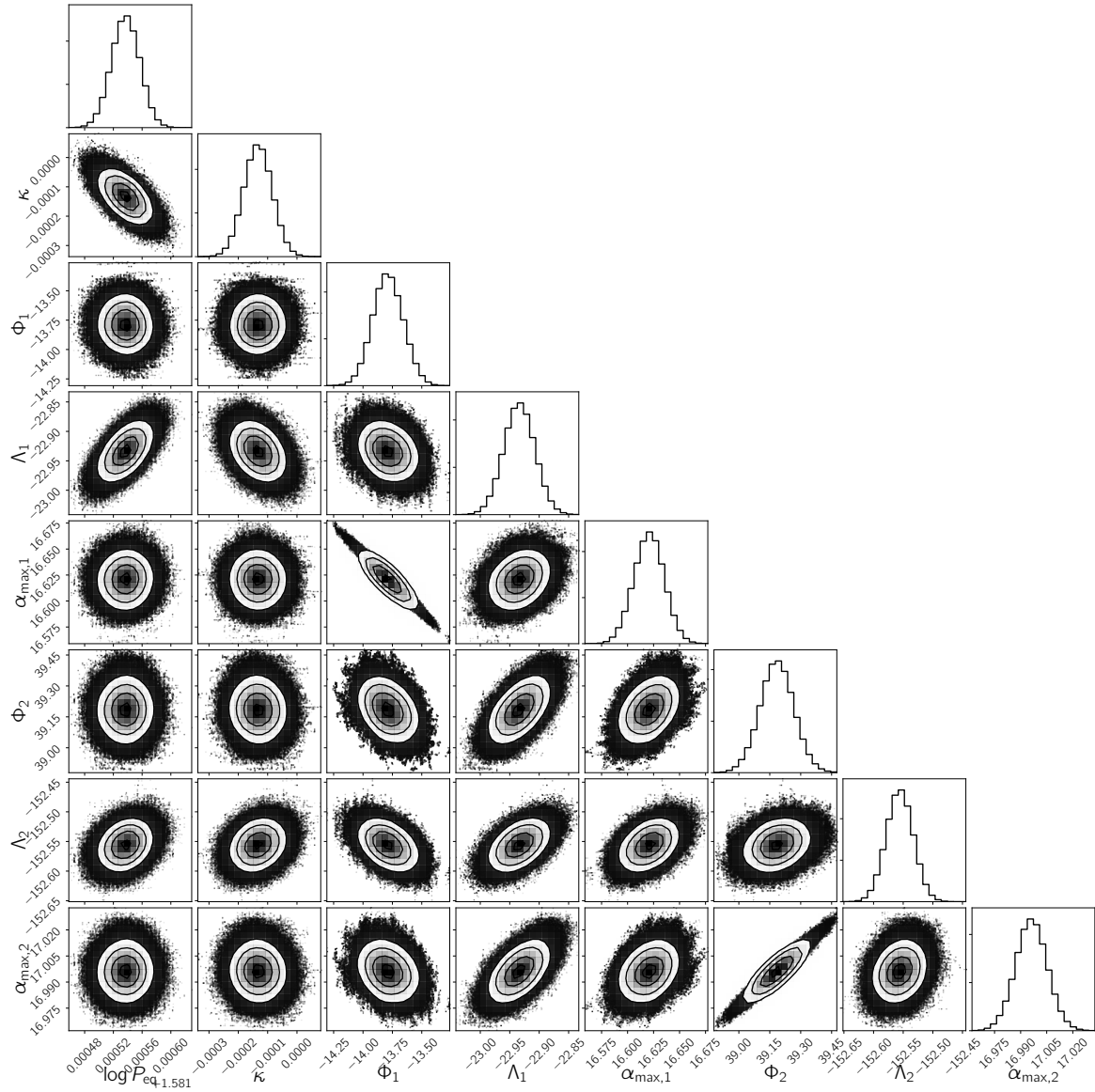
Figure 3.11: The joint posterior distribution of parameters for *TESS* light curve of AU
Mic by the two-spot model. Each column represents the equatorial period $P_{\rm eq}$, degree
of differential rotation $\kappa$, latitude $\Phi_k$, longitude $\Lambda_k$, and maximum radius $\alpha_{{\rm max},k}$.
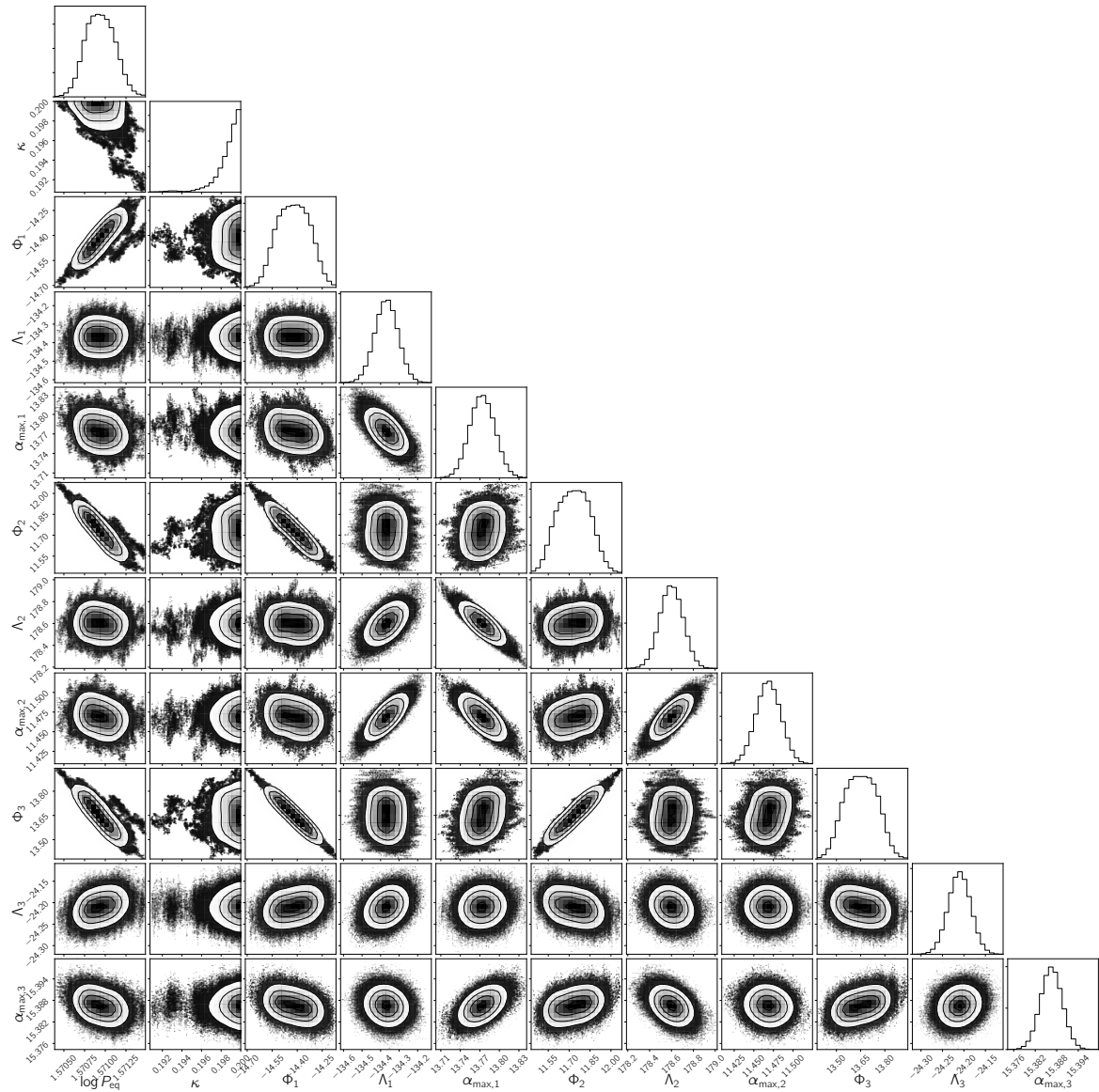
Figure 3.12: Same as Figure 3.11 but for the three-spot model.
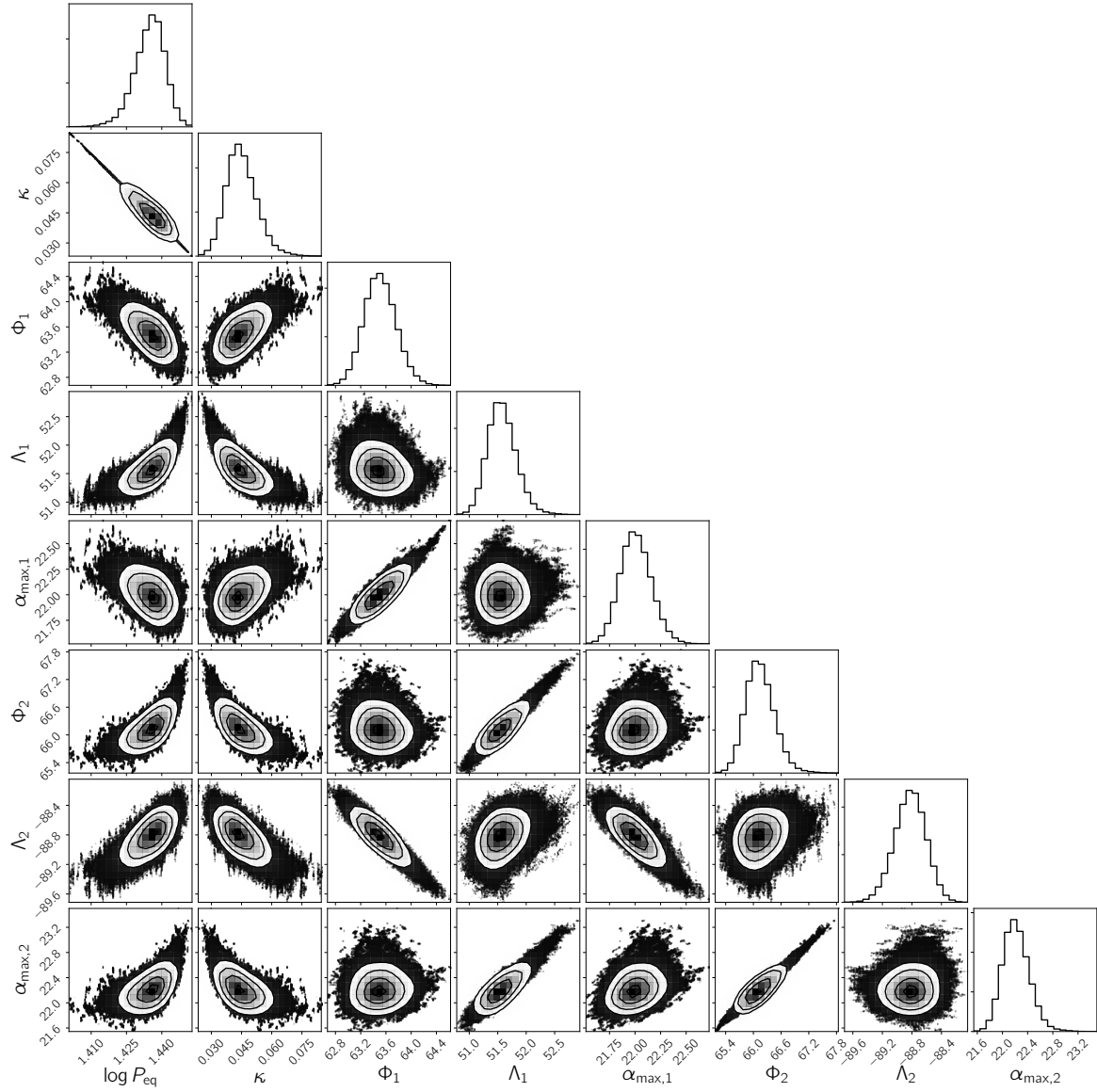
Figure 3.13: The joint posterior distribution of parameters for *TESS* light curve of EV Lac by the two-spot model. Each column represents the equatorial period $P_{\mathrm{eq}}$, degree of differential rotation $\kappa$, latitude $\Phi_k$, longitude $\Lambda_k$, and maximum radius $\alpha_{\mathrm{max},k}$.
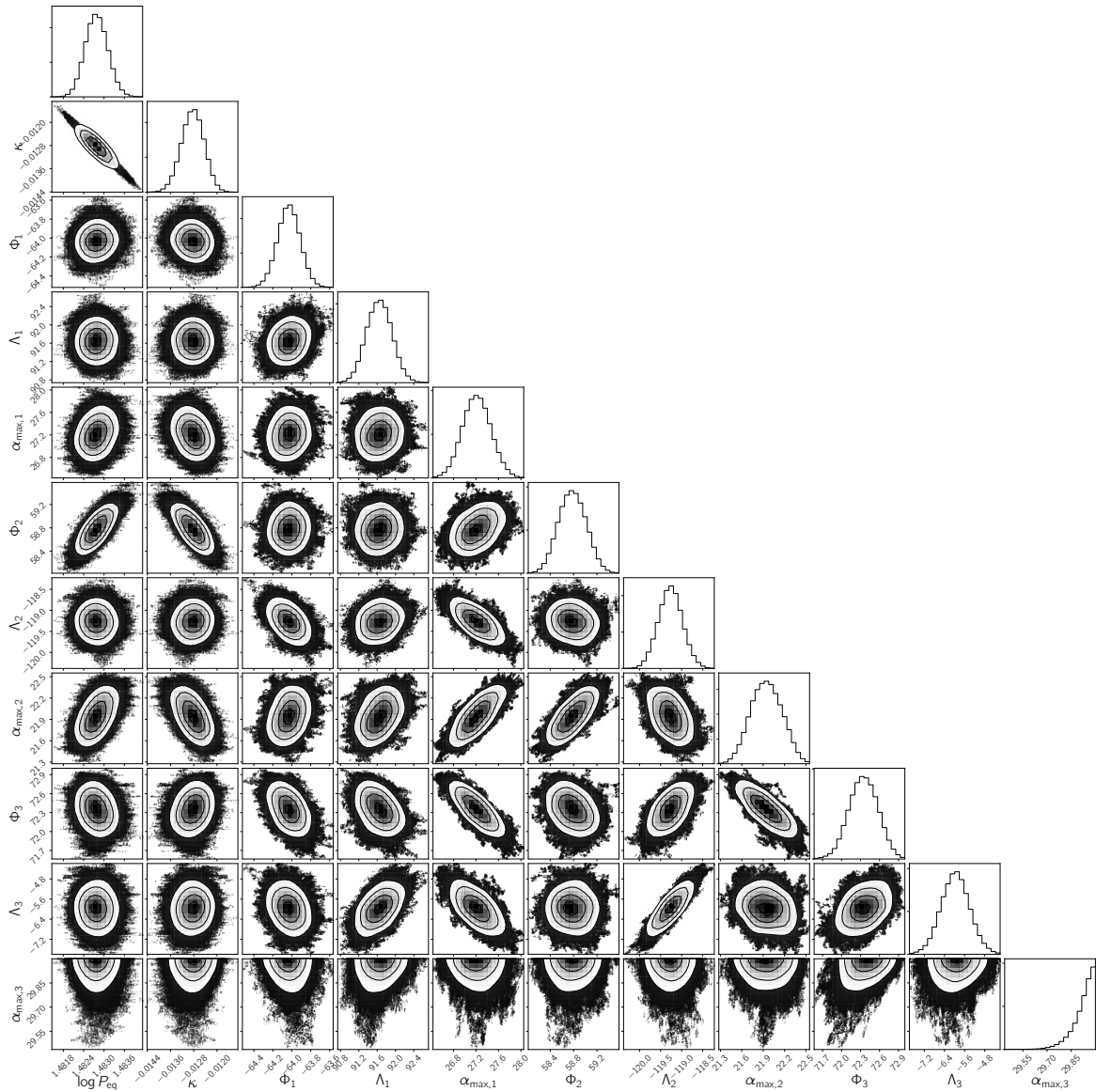
Figure 3.14: Same as Figure 3.13 but for the three-spot model.
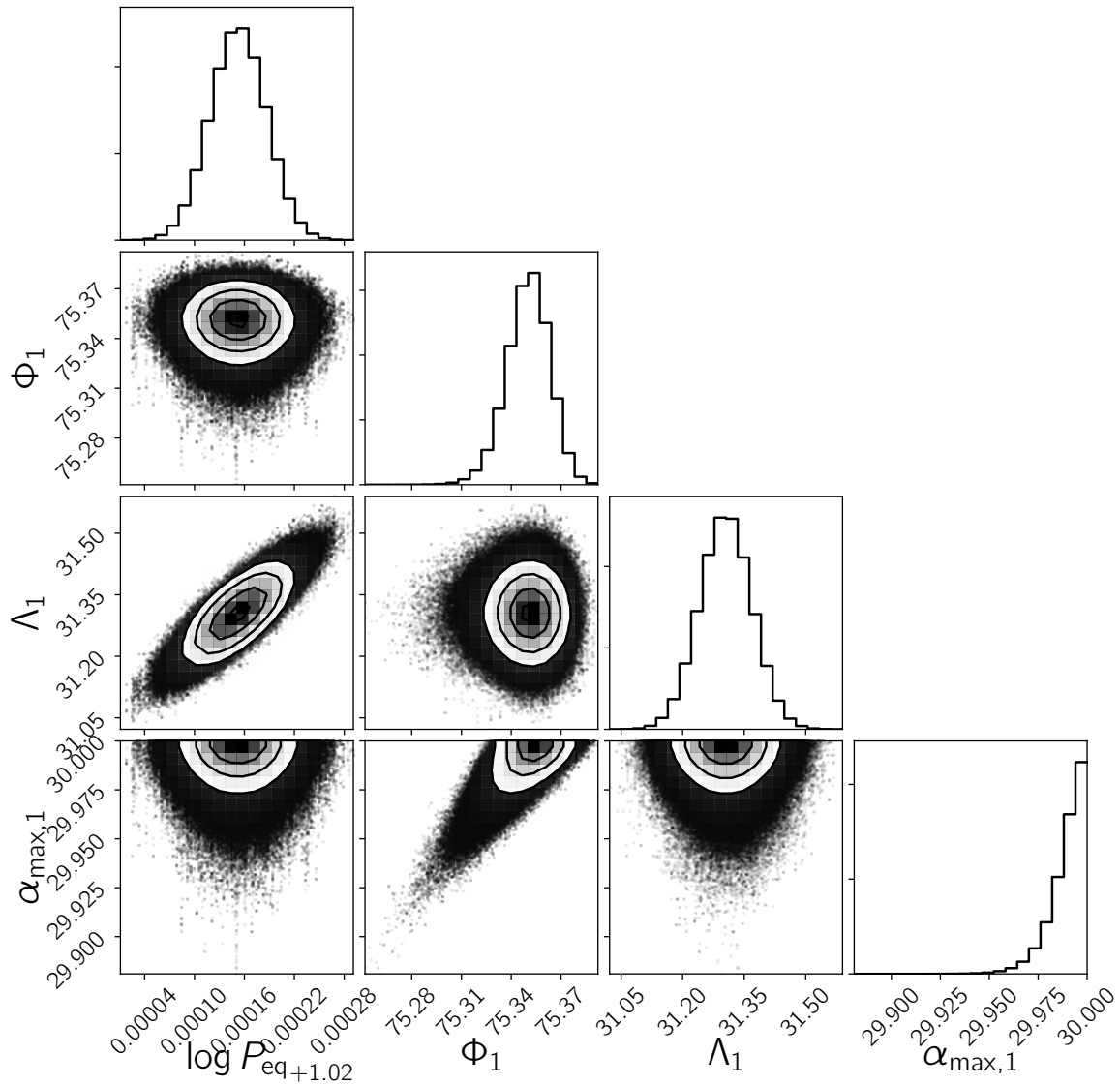
Figure 3.15: The joint posterior distribution of parameters for *TESS* light curve of YZ CMi by the one-spot model. Each column represents the equatorial period $P_{eq}$, degree of differential rotation $\kappa$, latitude $\Phi_k$, longitude $\Lambda_k$, and maximum radius $\alpha_{\max,k}$.
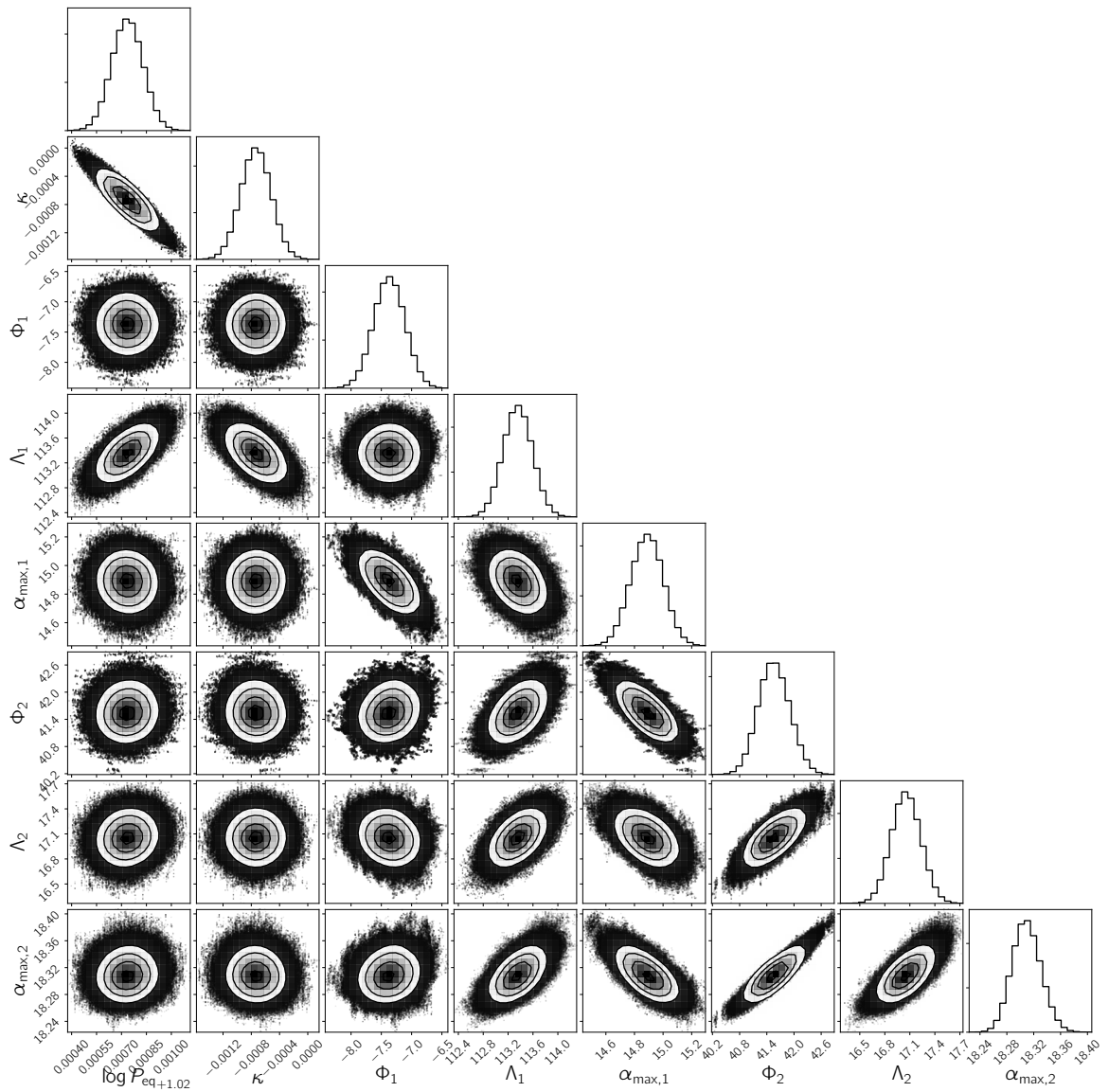
Figure 3.16: Same as Figure 3.15 but for the two-spot model.

# References

Almenara, J. M., Díaz, R. F., Dorn, C., Bonfils, X., and Udry, S. (2018). Absolute densities in exoplanetary systems: photodynamical modelling of Kepler-138. , 478(1):460–486.

Andrieu, C. and Thoms, J. (2008). A tutorial on adaptive mcmc. *Statistics and Computing*, 18:343–373.

Araki, T. and Ikeda, K. (2013). Adaptive markov chain monte carlo for auxiliary variable method and its application to parallel tempering. *Neural networks : the official journal of the International Neural Network Society*, 43:33–40.

Arkhypov, O. V., Khodachenko, M. L., Lammer, H., Güdel, M., Lüftinger, T., and Johnstone, C. P. (2018). Time-scales of stellar rotational variability and starspot diagnostics. , 473(1):L84–L88.

Auvergne, M., Bodin, P., Boisnard, L., Buey, J. T., Chaintreuil, S., Epstein, G., Jouret, M., Lam-Trong, T., Levacher, P., Magnan, A., Perez, R., Plasson, P., Plesseria, J., Peter, G., Steller, M., Tiphène, D., Baglin, A., Agogué, P., Appourchaux, T., Barbet, D., Beaufort, T., Bellenger, R., Berlin, R., Bernardi, P., Blouin, D., Boumier, P., Bonneau, F., Briet, R., Butler, B., Cautain, R., Chiavassa, F., Costes, V., Cuvilho, J., Cunha-Parro, V., de Oliveira Fialho, F., Decaudin, M., Defise, J. M., Djalal, S., Docclo, A., Drummond, R., Dupuis, O., Exil, G., Fauré, C., Gaboriaud, A., Gamet, P., Gavalda, P., Grolleau, E., Gueguen, L., Guivarc'h, V., Guterman, P., Hasiba, J., Huntzinger, G., Hustaix, H., Imbert, C., Jeanville, G., Johlander, B., Jorda, L., Journoud, P., Karioty, F., Kerjean, L., Lafond, L., Lapeyrere, V., Landiech, P., Larqué, T., Laudet, P., Le Merrer, J., Leporati, L., Leruyet, B., Levieuge, B., Llebaria, A., Martin, L., Mazy, E., Mesnager, J. M., Michel, J. P., Moalic, J. P., Monjoin, W., Naudet, D., Neukirchner, S., Nguyen-Kim, K., Ollivier, M., Orcesi, J. L., Ottacher, H.,

Oulali, A., Parisot, J., Perruchot, S., Piacentino, A., Pinheiro da Silva, L., Platzer, J., Pontet, B., Pradines, A., Quentin, C., Rohbeck, U., Rolland, G., Rollenhagen, F., Romagnan, R., Russ, N., Samadi, R., Schmidt, R., Schwartz, N., Sebbag, I., Smit, H., Sunter, W., Tello, M., Toulouse, P., Ulmer, B., Vandermarcq, O., Vergnault, E., Wallner, R., Waultier, G., and Zanatta, P. (2009). The CoRoT satellite in flight: description and performance. , 506(1):411–424.

Baroch, D., Morales, J. C., Ribas, I., Herrero, E., Rosich, A., Perger, M., Anglada-Escudé, G., Reiners, A., Caballero, J. A., Quirrenbach, A., Amado, P. J., Jeffers, S. V., Cifuentes, C., Passegger, V. M., Schweitzer, A., Lafarga, M., Bauer, F. F., Béjar, V. J. S., Colomé, J., Cortés-Contreras, M., Dreizler, S., Galadí-Enríquez, D., Hatzes, A. P., Henning, T., Kaminski, A., Kürster, M., Montes, D., Rodríguez-López, C., and Zechmeister, M. (2020). The CARMENES search for exoplanets around M dwarfs. Convective shift and starspot constraints from chromatic radial velocities. , 641:A69.

Basri, G. (2018). Calibration of Differential Light Curves for Physical Analysis of Starspots. , 865(2):142.

Basri, G. and Nguyen, H. T. (2018). Double Dipping: A New Relation between Stellar Rotation and Starspot Activity. , 863(2):190.

Basri, G. and Shah, R. (2020). The Information Content in Analytic Spot Models of Broadband Precision Light Curves. II. Spot Distributions and Lifetimes and Global and Differential Rotation. , 901(1):14.

Basri, G., Walkowicz, L. M., Batalha, N., Gilliland, R. L., Jenkins, J., Borucki, W. J., Koch, D., Caldwell, D., Dupree, A. K., Latham, D. W., Meibom, S., Howell, S., and Brown, T. (2010). Photometric Variability in Kepler Target Stars: The Sun Among Stars—a First Look. , 713(2):L155–L159.

Basri, G., Walkowicz, L. M., and Reiners, A. (2013). Comparison of Kepler Photometric Variability with the Sun on Different Timescales. , 769(1):37.

Benz, A. O. (2017). Flare Observations. *Living Reviews in Solar Physics*, 14(1):2.

Benz, A. O. and Güdel, M. (2010). Physical Processes in Magnetically Driven Flares on the Sun, Stars, and Young Stellar Objects. , 48:241–287.

Berdyugina, S. V. (2005). Starspots: A Key to the Stellar Dynamo. *Living Reviews in Solar Physics*, 2(1):8.

Berger, T. A., Huber, D., Gaidos, E., and van Saders, J. L. (2018). Revised Radii of Kepler Stars and Planets Using Gaia Data Release 2. , 866(2):99.

Bradshaw, S. J. and Hartigan, P. (2014). On Sunspot and Starspot Lifetimes. , 795(1):79.

Brooks, S. and Gelman, A. (1998). General methods for monitoring convergence of iterative simulations. *Journal of Computational and Graphical Statistics*, 7:434–455.

Brun, A. S. and Browning, M. K. (2017). Magnetism, dynamo action and the solar-stellar connection. *Living Reviews in Solar Physics*, 14(1):4.

Carrington, R. C. (1858). Cyril C. Jackson, Esq., Grand Cairo. *Monthly Notices of the Royal Astronomical Society*, 19(1):1–1.

Carrington, R. C. (1859). Description of a Singular Appearance seen in the Sun on September 1, 1859. *Monthly Notices of the Royal Astronomical Society*, 20(1):13–15.

Claret, A. (2018). A new method to compute limb-darkening coefficients for stellar atmosphere models with spherical symmetry: the space missions TESS, Kepler, CoRoT, and MOST. , 618:A20.

Cox, A. N. (2000). *Allen's astrophysical quantities.*

Croll, B. (2006). Markov Chain Monte Carlo Methods Applied to Photometric Spot Modeling. , 118(847):1351–1359.

Croll, B., Walker, G. A. H., Kuschnig, R., Matthews, J. M., Rowe, J. F., Walker, A., Rucinski, S. M., Hatzes, A. P., Cochran, W. D., Robb, R. M., Guenther, D. B., Moffat, A. F. J., Sasselov, D., and Weiss, W. W. (2006). Differential Rotation of ∈ Eridani Detected by MOST. , 648(1):607–613.

Davenport, J. (2015). *Spots and Flares: Stellar Activity in the Time Domain Era.* PhD thesis, University of Washington.

Davenport, J. R. A., Hebb, L., and Hawley, S. L. (2015). Detecting Differential Rotation and Starspot Evolution on the M Dwarf GJ 1243 with Kepler. , 806(2):212.

Davenport, J. R. A., Mendoza, G. T., and Hawley, S. L. (2020). 10 Years of Stellar Activity for GJ 1243. , 160(1):36.

Díaz, R. F., Almenara, J. M., Santerne, A., Moutou, C., Lethuillier, A., and Deleuil, M. (2014). PASTIS: Bayesian extrasolar planet validation - I. General framework, models, and performance. , 441(2):983–1004.

Eker, Z. (1994). Modeling Light Curves of Spotted Stars. , 420:373.

Eker, Z. (1996). Synthetic Light Curves of Spotted Stars: Unique or Not Unique? , 473:388.

Ford, E. B. (2005). Quantifying the Uncertainty in the Orbits of Extrasolar Planets. , 129(3):1706–1717.

Ford, E. B. (2006). Improving the Efficiency of Markov Chain Monte Carlo for Analyzing the Orbits of Extrasolar Planets. , 642(1):505–522.

Foreman-Mackey, D. (2016). corner.py: Scatterplot matrices in Python. *The Journal of Open Source Software*, 1:24.

Foreman-Mackey, D., Hogg, D. W., Lang, D., and Goodman, J. (2013). emcee: The MCMC Hammer. , 125(925):306.

Frasca, A., Fröhlich, H. E., Bonanno, A., Catanzaro, G., Biazzo, K., and Molenda-Żakowicz, J. (2011). Magnetic activity and differential rotation in the very young star KIC 8429280. , 532:A81.

Fröhlich, H. E., Frasca, A., Catanzaro, G., Bonanno, A., Corsaro, E., Molenda-Żakowicz, J., Klutsch, A., and Montes, D. (2012). Magnetic activity and differential rotation in the young Sun-like stars KIC 7985370 and KIC 7765135. , 543:A146.

Gelman, A. and Rubin, D. B. (1992). Inference from Iterative Simulation Using Multiple Sequences. *Statistical Science*, 7:457–472.

Giles, H. A. C., Collier Cameron, A., and Haywood, R. D. (2017). A Kepler study of starspot lifetimes with respect to light-curve amplitude and spectral type. , 472(2):1618–1627.

Gray, D. F. (2008). *The Observation and Analysis of Stellar Photospheres.*

Gregory, P. C. (2005a). A Bayesian Analysis of Extrasolar Planet Data for HD 73526. , 631(2):1198–1214.

Gregory, P. C. (2005b). *Bayesian Logical Data Analysis for the Physical Sciences: A Comparative Approach with 'Mathematica' Support.*

Güdel, M. (2007). The Sun in Time: Activity and Environment. *Living Reviews in Solar Physics*, 4(1):3.

Haario, H., Saksman, E., and Tamminen, J. (2001). An adaptive metropolis algorithm. *Bernoulli*, 7:223–242.

Hale, G. E. (1908). On the Probable Existence of a Magnetic Field in Sun-Spots. , 28:315.

Hale, G. E., Ellerman, F., Nicholson, S. B., and Joy, A. H. (1919). The Magnetic Polarity of Sun-Spots. , 49:153.

Hale, G. E. and Nicholson, S. B. (1925). The Law of Sun-Spot Polarity. , 62:270.

Hastings, W. (1970). Monte carlo sampling methods using markov chains and their applications. *Biometrika*, 57:97–109.

Hathaway, D. H. (2015). The Solar Cycle. *Living Reviews in Solar Physics*, 12(1):4.

Hawley, S. L. and Pettersen, B. R. (1991). The Great Flare of 1985 April 12 on AD Leonis. , 378:725.

Henry, G. W., Eaton, J. A., Hamer, J., and Hall, D. S. (1995). Starspot Evolution, Differential Rotation, and Magnetic Cycles in the Chromospherically Active Binaries lambda Andromedae, sigma Geminorum, II Pegasi, and V711 Tauri. , 97:513.

Hogg, D. W. and Foreman-Mackey, D. (2018). Data Analysis Recipes: Using Markov Chain Monte Carlo. , 236(1):11.

Honda, S., Notsu, Y., Namekata, K., Notsu, S., Maehara, H., Ikuta, K., Nogami, D., and Shibata, K. (2018). Time-resolved spectroscopic observations of an M-dwarf flare star EV Lacertae during a flare. , 70(4):62.

Hukushima, K. and Nemoto, K. (1996). Exchange Monte Carlo Method and Application to Spin Glass Simulations. *Journal of the Physical Society of Japan*, 65(6):1604.

Ikuta, K., Maehara, H., Notsu, Y., Namekata, K., Kato, T., Notsu, S., Okamoto, S., Honda, S., Nogami, D., and Shibata, K. (2020). Starspot Mapping with Adaptive Parallel Tempering. I. Implementation of Computational Code. , 902(1):73.

Kane, S. R. (1974). Impulsive (flash) Phase of Solar Flares: Hard X-Ray Microwave, EUV and Optical Observations. In Newkirk, G. A., editor, *Coronal Disturbances*, volume 57, page 105.

Karoff, C., Knudsen, M. F., De Cat, P., Bonanno, A., Fogtmann-Schulz, A., Fu, J., Frasca, A., Inceoglu, F., Olsen, J., Zhang, Y., Hou, Y., Wang, Y., Shi, J., and Zhang, W. (2016). Observational evidence for enhanced magnetic activity of superflare stars. *Nature Communications*, 7:11058.

Kass, R. E. and Raftery, A. E. (1995). Bayes factors. *Journal of the American Statistical Association*, 90(430):773–795.

Kipping, D. M. (2012). An analytic model for rotational modulations in the photometry of spotted stars. , 427(3):2487–2511.

Klein, B., Donati, J.-F., Moutou, C., Delfosse, X., Bonfils, X., Martioli, E., Fouqué, P., Cloutier, R., Artigau, É., Doyon, R., Hébrard, G., Morin, J., Rameau, J., Plavchan, P., and Gaidos, E. (2020). Investigating the young AUsystem with SPIRou: large-scale stellar magnetic field and close-in planet mass. *arXiv e-prints*, page arXiv:2011.13357.

Koch, D. G., Borucki, W. J., Basri, G., Batalha, N. M., Brown, T. M., Caldwell, D., Christensen-Dalsgaard, J., Cochran, W. D., DeVore, E., Dunham, E. W., Gautier, Thomas N., I., Geary, J. C., Gilliland, R. L., Gould, A., Jenkins, J., Kondo, Y., Latham, D. W., Lissauer, J. J., Marcy, G., Monet, D., Sasselov, D., Boss, A., Brownlee, D., Caldwell, J., Dupree, A. K., Howell, S. B., Kjeldsen, H., Meibom, S., Morrison, D., Owen, T., Reitsema, H., Tarter, J., Bryson, S. T., Dotson, J. L., Gazis, P., Haas, M. R., Kolodziejczak, J., Rowe, J. F., Van Cleve, J. E., Allen, C., Chandrasekaran, H., Clarke, B. D., Li, J., Quintana, E. V., Tenenbaum, P., Twicken, J. D., and Wu, H. (2010). Kepler Mission Design, Realized Photometric Performance, and Early Science. , 713(2):L79–L86.

Kochukhov, O. and Reiners, A. (2020). The Magnetic Field of the Active Planet-hosting M Dwarf AU Mic. , 902(1):43.

Kurita, M., Kino, M., Iwamuro, F., Ohta, K., Nogami, D., Izumiura, H., Yoshida, M., Matsubayashi, K., Kuroda, D., Nakatani, Y., Yamamoto, K., Tsutsui, H., Iribe, M., Jikuya, I., Ohtani, H., Shibata, K., Takahashi, K., Tokoro, H., Maihara, T., and Nagata, T. (2020). The Seimei telescope project and technical developments. , 72(3):48.

Lanza, A. F., Bonomo, A. S., Moutou, C., Pagano, I., Messina, S., Leto, G., Cutispoto, G., Aigrain, S., Alonso, R., Barge, P., Deleuil, M., Auvergne, M., Baglin, A., and Collier Cameron, A. (2010). Photospheric activity, rotation, and radial velocity variations of the planet-hosting star CoRoT-7. , 520:A53.

Lanza, A. F., Das Chagas, M. L., and De Medeiros, J. R. (2014). Measuring stellar differential rotation with high-precision space-borne photometry. , 564:A50.

Maehara, H., Notsu, Y., Namekata, K., Honda, S., Kowalski, A. F., Katoh, N., Ohshima, T., Iida, K., Oeda, M., Murata, K. L., Yamanaka, M., Takagi, K., Sasada, M., Akitaya, H., Ikuta, K., Okamoto, S., Nogami, D., and Shibata, K. (2020). Time-resolved spectroscopy and photometry

of M dwarf flare star YZ Canis Minoris with OISTER and TESS: Blue asymmetry in the Hα line during the non-white light flare. .

Maehara, H., Notsu, Y., Notsu, S., Namekata, K., Honda, S., Ishii, T. T., Nogami, D., and Shibata, K. (2017). Starspot activity and superflares on solar-type stars. , 69(3):41.

Maehara, H., Shibayama, T., Notsu, S., Notsu, Y., Nagao, T., Kusaba, S., Honda, S., Nogami, D., and Shibata, K. (2012). Superflares on solar-type stars. , 485(7399):478–481.

Martioli, E., Hébrard, G., Moutou, C., Donati, J. F., Artigau, É., Cale, B., Cook, N. J., Dalal, S., Delfosse, X., Forveille, T., Gaidos, E., Plavchan, P., Berberian, J., Carmona, A., Cloutier, R., Doyon, R., Fouqué, P., Klein, B., Lecavelier des Etangs, A., Manset, N., Morin, J., Tanner, A., Teske, J., and Wang, S. (2020). Spin-orbit alignment and magnetic activity in the young planetary system AU Mic. , 641:L1.

McQuillan, A., Mazeh, T., and Aigrain, S. (2014). Rotation Periods of 34,030 Kepler Main-sequence Stars: The Full Autocorrelation Sample. , 211(2):24.

Metropolis, N., Rosenbluth, A. W., Rosenbluth, M. N., Teller, A. H., and Teller, E. (1953). Equation of State Calculations by Fast Computing Machines. , 21(6):1087–1092.

Montet, B. T., Tovar, G., and Foreman-Mackey, D. (2017). Long-term Photometric Variability in Kepler Full-frame Images: Magnetic Cycles of Sun-like Stars. , 851(2):116.

Morin, J., Donati, J. F., Petit, P., Delfosse, X., Forveille, T., Albert, L., Aurière, M., Cabanac, R., Dintrans, B., Fares, R., Gastine, T., Jardine, M. M., Lignières, F., Paletou, F., Ramirez Velez, J. C., and Théado, S. (2008). Large-scale magnetic topologies of mid M dwarfs. , 390(2):567–581.

Morris, B. M., Hebb, L., Davenport, J. R. A., Rohn, G., and Hawley, S. L. (2017). The Starspots of HAT-P-11: Evidence for a Solar-like Dynamo. , 846(2):99.

Mosser, B., Baudin, F., Lanza, A. F., Hulot, J. C., Catala, C., Baglin, A., and Auvergne, M. (2009). Short-lived spots in solar-like stars as observed by CoRoT. , 506(1):245–254.

Namekata, K., Davenport, J. R. A., Morris, B. M., Hawley, S. L., Maehara, H., Notsu, Y., Toriumi, S., Ikuta, K., Notsu, S., Honda, S., Nogami,

D., and Shibata, K. (2020). Temporal Evolution of Spatially Resolved Individual Star Spots on a Planet-hosting Solar-type Star: Kepler-17. , 891(2):103.

Namekata, K., Maehara, H., Notsu, Y., Toriumi, S., Hayakawa, H., Ikuta, K., Notsu, S., Honda, S., Nogami, D., and Shibata, K. (2019). Lifetimes and Emergence/Decay Rates of Star Spots on Solar-type Stars Estimated by Kepler Data in Comparison with Those of Sunspots. , 871(2):187.

Neal, R. (1996). Sampling from multimodal distributions using tempered transitions. *Statistics and Computing*, 6:353–366.

Neal, R. (2001). Annealed importance sampling. *Statistics and Computing*, 11:125–139.

Nelson, B., Ford, E. B., and Payne, M. J. (2014). RUN DMC: An Efficient, Parallel Code for Analyzing Radial Velocity Observations Using N-body Integrations and Differential Evolution Markov Chain Monte Carlo. , 210(1):11.

Nogami, D., Notsu, Y., Honda, S., Maehara, H., Notsu, S., Shibayama, T., and Shibata, K. (2014). Two sun-like superflare stars rotating as slow as the Sun*. , 66(2):L4.

Notsu, S., Honda, S., Notsu, Y., Nagao, T., Shibayama, T., Maehara, H., Nogami, D., and Shibata, K. (2013a). High-Dispersion Spectroscopy of the Superflare Star KIC 6934317. , 65:112.

Notsu, Y., Honda, S., Maehara, H., Notsu, S., Shibayama, T., Nogami, D., and Shibata, K. (2015a). High dispersion spectroscopy of solar-type superflare stars. I. Temperature, surface gravity, metallicity, and vsin i. , 67(3):32.

Notsu, Y., Honda, S., Maehara, H., Notsu, S., Shibayama, T., Nogami, D., and Shibata, K. (2015b). High dispersion spectroscopy of solar-type superflare stars. II. Stellar rotation, starspots, and chromospheric activities. , 67(3):33.

Notsu, Y., Maehara, H., Honda, S., Hawley, S. L., Davenport, J. R. A., Namekata, K., Notsu, S., Ikuta, K., Nogami, D., and Shibata, K. (2019). Do Kepler Superflare Stars Really Include Slowly Rotating Sun-like Stars?—Results Using APO 3.5 m Telescope Spectroscopic Observations and Gaia-DR2 Data. , 876(1):58.

Notsu, Y., Shibayama, T., Maehara, H., Notsu, S., Nagao, T., Honda, S., Ishii, T. T., Nogami, D., and Shibata, K. (2013b). Superflares on Solar-type Stars Observed with Kepler II. Photometric Variability of Superflare-generating Stars: A Signature of Stellar Rotation and Starspots. , 771(2):127.

Okamoto, S., Notsu, Y., Maehara, H., Namekata, K., Honda, S., Ikuta, K., Nogami, D., and Shibata, K. (2020). Statistical Properties of Superflares on Solar-type Stars: Results Using All of the Kepler Primary Mission Data. *arXiv e-prints*, page arXiv:2011.02117.

Osten, R. A., Kowalski, A., Drake, S. A., Krimm, H., Page, K., Gazeas, K., Kennea, J., Oates, S., Page, M., de Miguel, E., Novák, R., Apeltauer, T., and Gehrels, N. (2016). A Very Bright, Very Hot, and Very Long Flaring Event from the M Dwarf Binary System DG CVn. , 832(2):174.

Parker, E. N. (1955). Hydromagnetic Dynamo Models. , 122:293.

Reinhold, T., Reiners, A., and Basri, G. (2013). Rotation and differential rotation of active Kepler stars. , 560:A4.

Ricker, G. R., Winn, J. N., Vanderspek, R., Latham, D. W., Bakos, G. Á., Bean, J. L., Berta-Thompson, Z. K., Brown, T. M., Buchhave, L., Butler, N. R., Butler, R. P., Chaplin, W. J., Charbonneau, D., Christensen-Dalsgaard, J., Clampin, M., Deming, D., Doty, J., De Lee, N., Dressing, C., Dunham, E. W., Endl, M., Fressin, F., Ge, J., Henning, T., Holman, M. J., Howard, A. W., Ida, S., Jenkins, J., Jernigan, G., Johnson, J. A., Kaltenegger, L., Kawai, N., Kjeldsen, H., Laughlin, G., Levine, A. M., Lin, D., Lissauer, J. J., MacQueen, P., Marcy, G., McCullough, P. R., Morton, T. D., Narita, N., Paegert, M., Palle, E., Pepe, F., Pepper, J., Quirrenbach, A., Rinehart, S. A., Sasselov, D., Sato, B., Seager, S., Sozzetti, A., Stassun, K. G., Sullivan, P., Szentgyorgyi, A., Torres, G., Udry, S., and Villasenor, J. (2014). Transiting Exoplanet Survey Satellite (TESS). In Oschmann, Jacobus M., J., Clampin, M., Fazio, G. G., and MacEwen, H. A., editors, *Space Telescopes and Instrumentation 2014: Optical, Infrared, and Millimeter Wave*, volume 9143 of *Society of Photo-Optical Instrumentation Engineers (SPIE) Conference Series*, page 914320.

Robbins, H. and Monro, S. (1951). A stochastic approximation method. *Ann. Math. Statist.*, 22(3):400–407.

Roberts, G., Gelman, A., and Gilks, W. R. (1997). Weak convergence and optimal scaling of random walk metropolis algorithms. *Annals of Applied Probability*, 7:110–120.

Roberts, G. O. and Rosenthal, J. S. (1998). Markov-chain monte carlo: Some practical implications of theoretical results. *Canadian Journal of Statistics*, 26(1):5–20.

Sammis, I., Tang, F., and Zirin, H. (2000). The Dependence of Large Flare Occurrence on the Magnetic Structure of Sunspots. , 540(1):583–587.

Savanov, I. S. and Strassmeier, K. G. (2008). Light-curve inversions with truncated least-squares principal components: Tests and application to HD 291095 = V1355 Orionis. *Astronomische Nachrichten*, 329(4):364.

Schaefer, B. E., King, J. R., and Deliyannis, C. P. (2000). Superflares on Ordinary Solar-Type Stars. , 529(2):1026–1030.

Shallue, C. J. and Vanderburg, A. (2018). Identifying Exoplanets with Deep Learning: A Five-planet Resonant Chain around Kepler-80 and an Eighth Planet around Kepler-90. , 155(2):94.

Sharma, S. (2017). Markov Chain Monte Carlo Methods for Bayesian Data Analysis in Astronomy. , 55(1):213–259.

Shibata, K., Isobe, H., Hillier, A., Choudhuri, A. R., Maehara, H., Ishii, T. T., Shibayama, T., Notsu, S., Notsu, Y., Nagao, T., Honda, S., and Nogami, D. (2013). Can Superflares Occur on Our Sun? , 65:49.

Shibata, K. and Magara, T. (2011). Solar Flares: Magnetohydrodynamic Processes. *Living Reviews in Solar Physics*, 8(1):6.

Shibayama, T., Maehara, H., Notsu, S., Notsu, Y., Nagao, T., Honda, S., Ishii, T. T., Nogami, D., and Shibata, K. (2013). Superflares on Solar-type Stars Observed with Kepler. I. Statistical Properties of Superflares. , 209(1):5.

Sing, D. K. (2010). Stellar limb-darkening coefficients for CoRot and Kepler. , 510:A21.

Strassmeier, K. G. (1999). Doppler imaging of stellar surface structure. XI. The super starspots on the K0 giant HD 12545: larger than the entire Sun. , 347:225–234.

Strassmeier, K. G. (2009). Starspots. , 17(3):251–308.

Strassmeier, K. G. and Bopp, B. W. (1992). Time-series photometric SPOT modeling. I. Parameter study and applicationto HD 17433 = VY

Arietis. , 259:183–197.

Strassmeier, K. G., Hall, D. S., and Henry, G. W. (1994). Time-series photometric SPOT modeling. II. Fifteen years of photometry of the bright RS CVN binary HR 7275. , 282:535–546.

Strassmeier, K. G. and Rice, J. B. (1998). Doppler imaging of stellar surface structure. VI. HD 129333 = EK Draconis: a stellar analog of the active young Sun. , 330:685–695.

Toriumi, S., Airapetian, V. S., Hudson, H. S., Schrijver, C. J., Cheung, M. C. M., and DeRosa, M. L. (2020). Sun-as-a-star Spectral Irradiance Observations of Transiting Active Regions. , 902(1):36.

Toriumi, S. and Wang, H. (2019). Flare-productive active regions. *Living Reviews in Solar Physics*, 16(1):3.

Tu, Z.-L., Yang, M., Zhang, Z. J., and Wang, F. Y. (2020). Superflares on Solar-type Stars from the First Year Observation of TESS. , 890(1):46.

Vousden, W. D., Farr, W. M., and Mandel, I. (2016). Dynamic temperature selection for parallel tempering in Markov chain Monte Carlo simulations. , 455(2):1919–1937.

Walker, G. A. H., Croll, B., Kuschnig, R., Walker, A., Rucinski, S. M., Matthews, J. M., Guenther, D. B., Moffat, A. F. J., Sasselov, D., and Weiss, W. W. (2007). The Differential Rotation of $\kappa^1$ Ceti as Observed by MOST. , 659(2):1611–1622.

Walkowicz, L. M., Basri, G., and Valenti, J. A. (2013). The Information Content in Analytic Spot Models of Broadband Precision Light Curves. , 205(2):17.

Walter, F. M. and Bowyer, S. (1981). On the coronae of rapidly rotating stars. I. The relation between rotation and coronal activity in RS CVn systems. , 245:671–676.

Wisniewski, J. P., Kowalski, A. F., Davenport, J. R. A., Schneider, G., Grady, C. A., Hebb, L., Lawson, K. D., Augereau, J.-C., Boccaletti, A., Brown, A., Debes, J. H., Gaspar, A., Henning, T. K., Hines, D. C., Kuchner, M. J., Lagrange, A.-M., Milli, J., Sezestre, E., Stark, C. C., and Thalmann, C. (2019). High-fidelity Imaging of the Inner AU Mic Debris Disk: Evidence of Differential Wind Sculpting? , 883(1):L8.

Yamada, Y., Uemura, M., Itoh, R., Fukazawa, Y., Ohno, M., and Imazato, F. (2020). Variations of the physical parameters of the blazar Mrk 421

based on analysis of the spectral energy distributions. , 72(3):42.

Zboril, M. (2003). Spot modelling of the flare M4.5 dwarf YZ CMi. *Astronomische Nachrichten*, 324(6):527–531.

# Appendix A

# Supplementary of Section 2

In this section, for the three-spot model and two-spot models in Section 2, we exhibit the joint posterior distribution of all the parameters. We can ascertain that the posterior distributions converge to unimodal distributions.
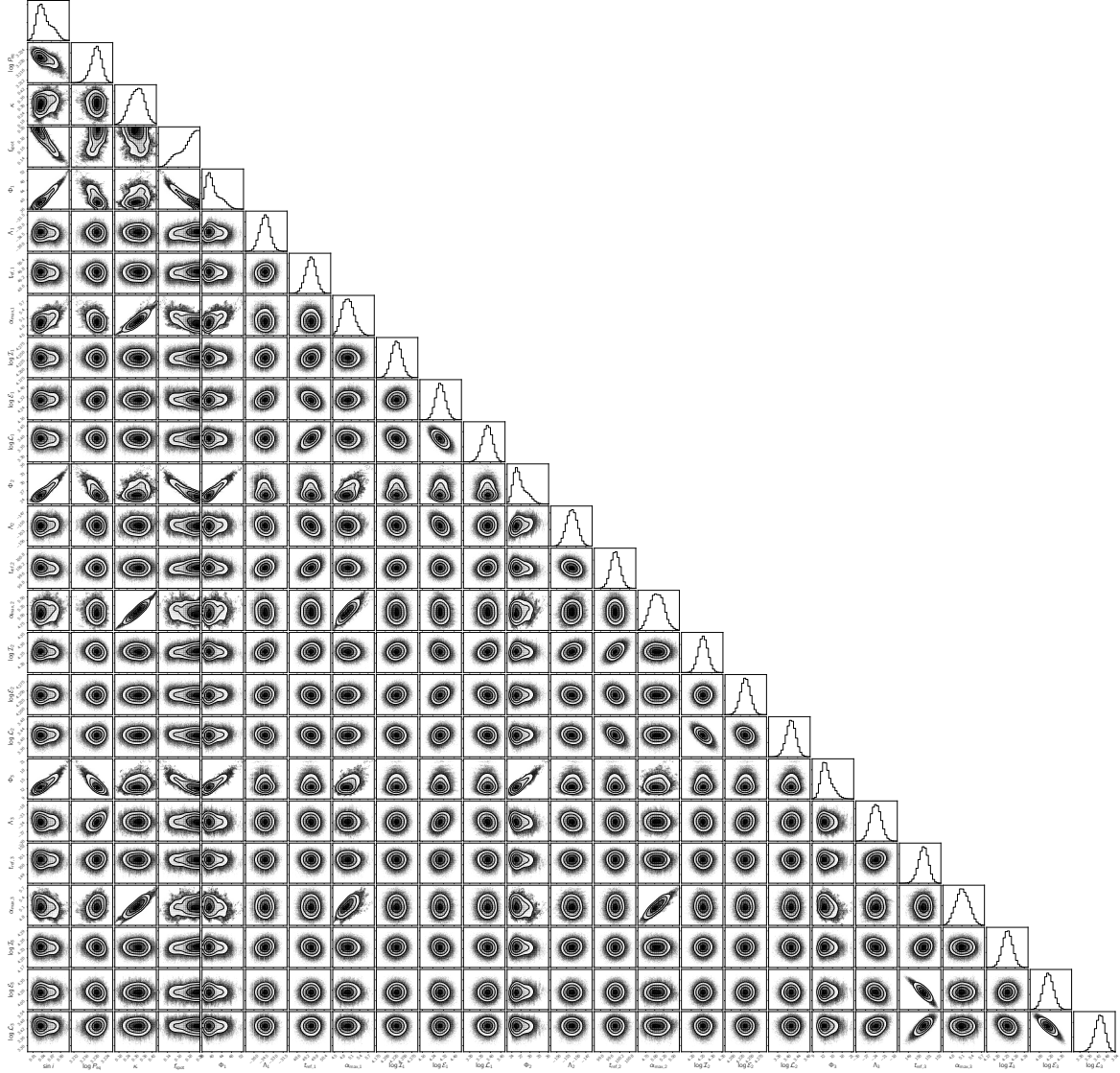
**Three-spot model for Two-spot-like light curve**



Figure A.1: The joint posterior distribution of all parameters for two-spots-like light curve by the three-spot model. Each column represents the inclination angle $\sin i$, equatorial period $P_{\mathrm{eq}}$, degree of differential rotation $\kappa$, relative intensity $f_{\mathrm{spot}}$, latitude $\Phi_k$, initial longitude $\Lambda_k$, reference time $t_k$, maximum radius $\alpha_{\mathrm{max},k}$, emergence duration $\mathcal{I}_k$, decay duration $\mathcal{E}_k$, and stable duration $\mathcal{L}_k$, in order of the parameters in Table 2.1.
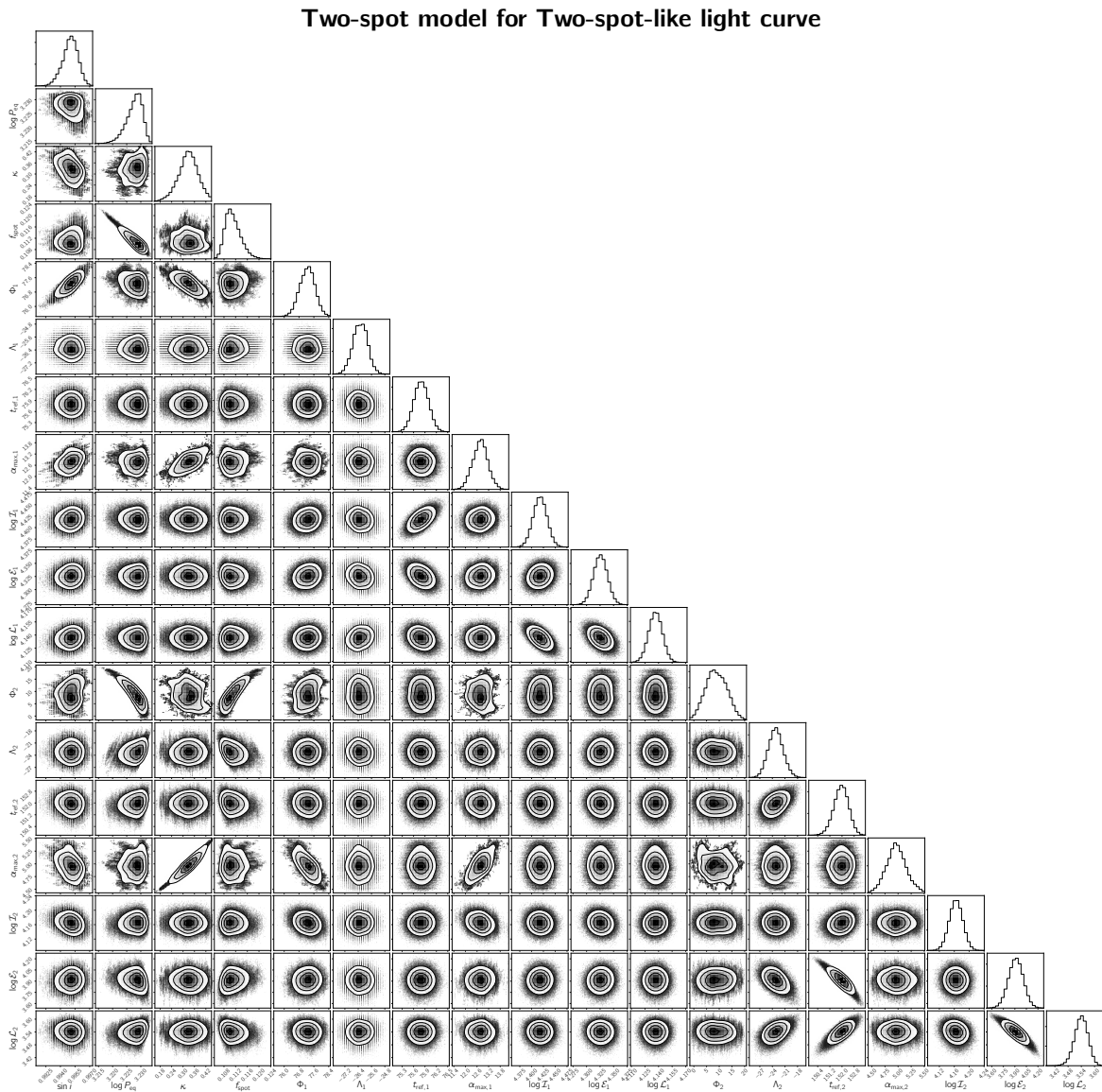
**Two-spot model for Two-spot-like light curve**



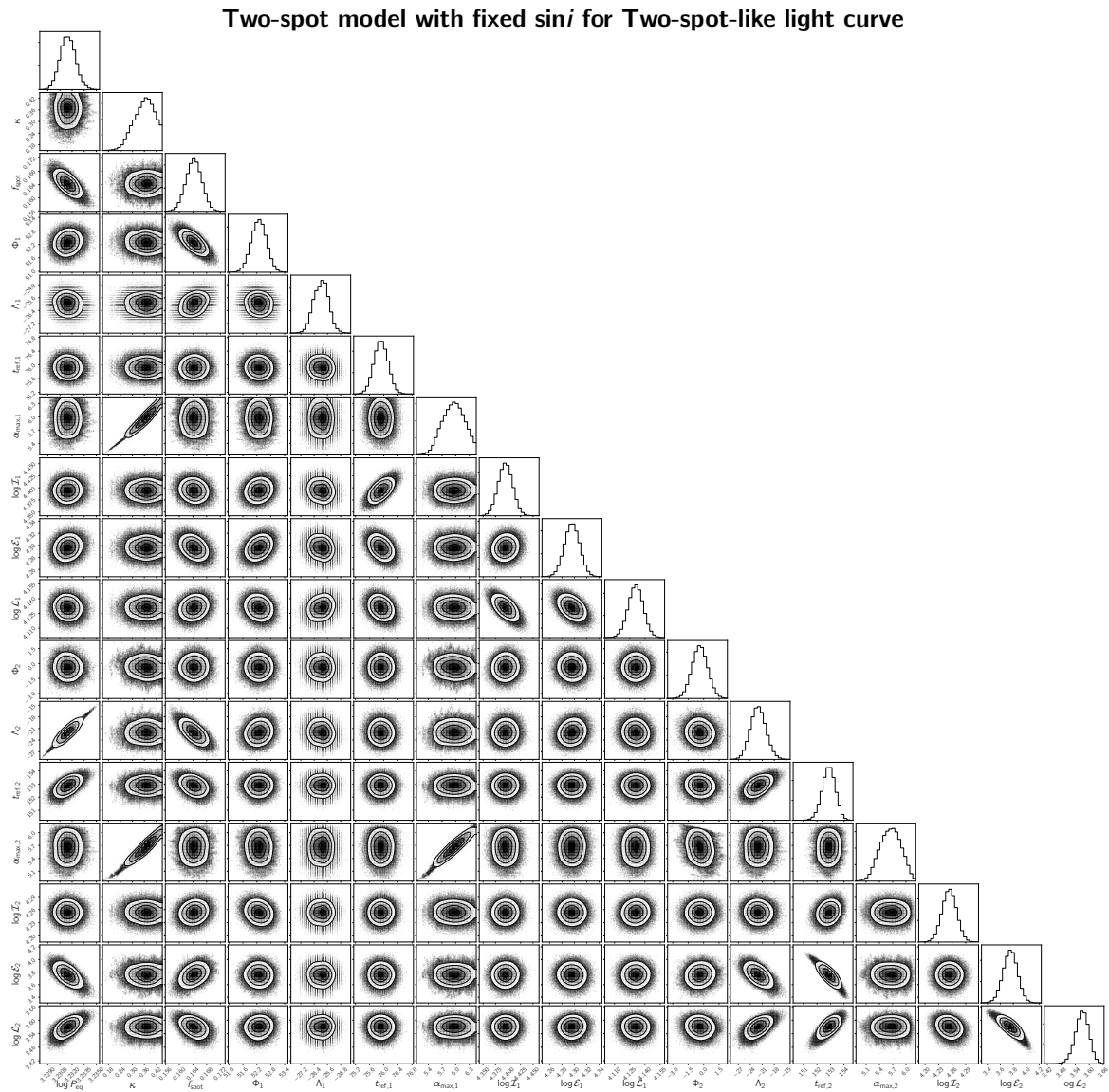Figure A.2: Same as Figure A.1 but for the two-spot model.

Figure A.3: Same as Figure A.1 but for the two-spot model with fixed $\sin i$.

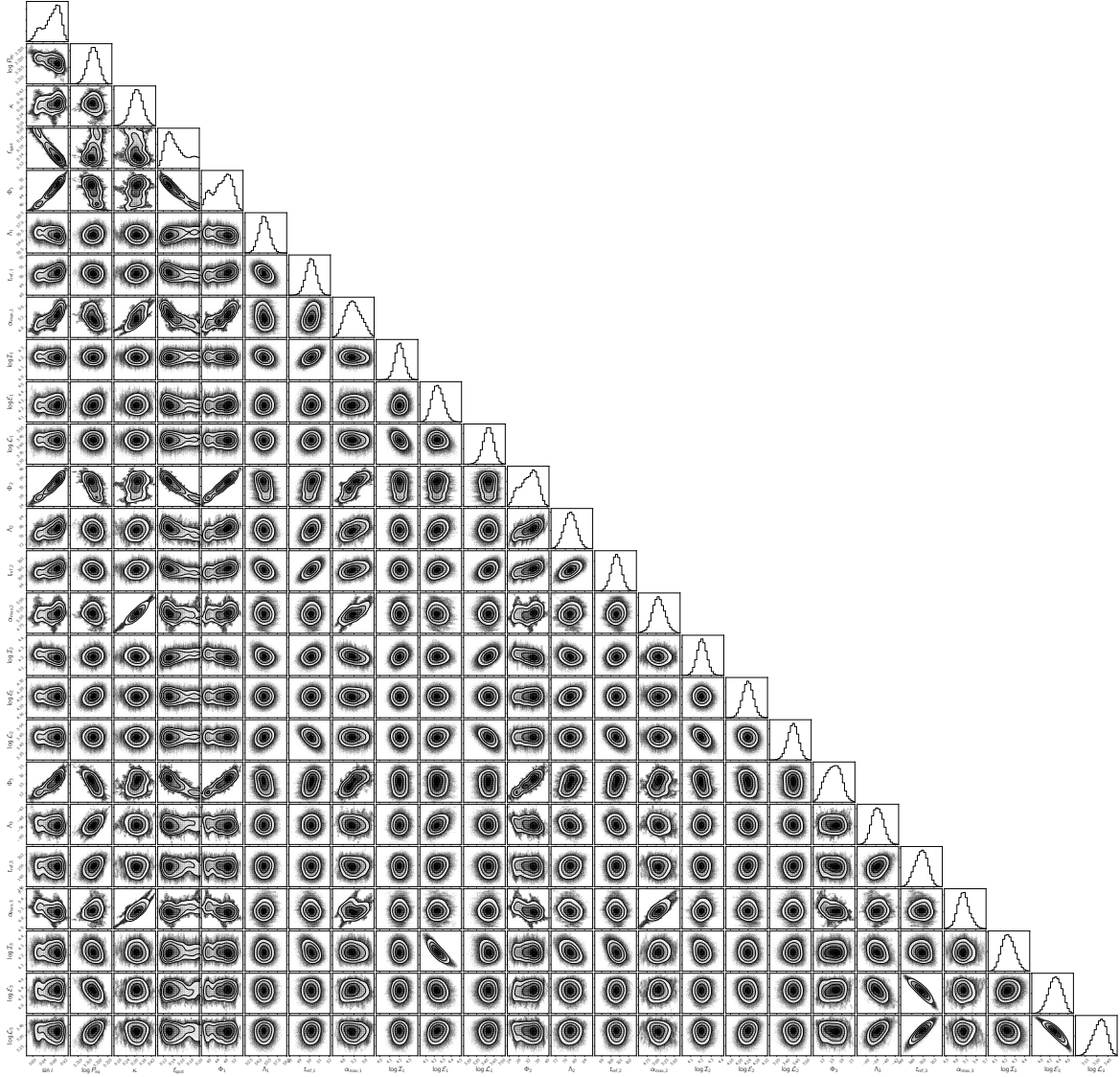**Three-spot model for One-spot-like light curve**



Figure A.4: The joint posterior distribution of all parameters for one-spots-like light curve by the three-spot model. Each column represents the inclination angle $\sin i$, equatorial period $P_{\mathrm{eq}}$, degree of differential rotation $\kappa$, relative intensity $f_{\mathrm{spot}}$, latitude $\Phi_k$, initial longitude $\Lambda_k$, reference time $t_k$, maximum radius $\alpha_{\mathrm{max},k}$, emergence duration $\mathcal{I}_k$, decay duration $\mathcal{E}_k$, and stable duration $\mathcal{L}_k$, in order of the parameters in Table 2.2.
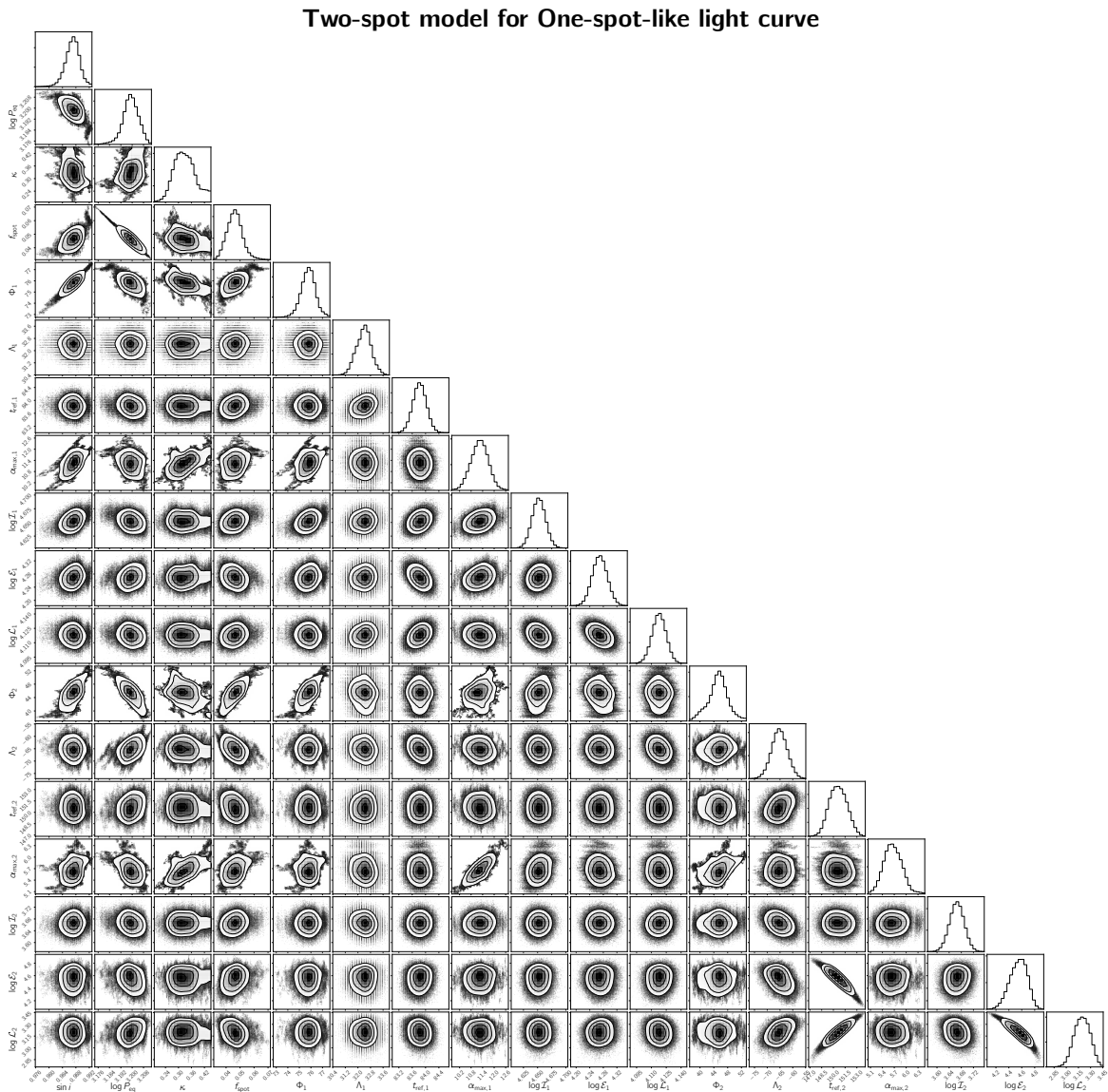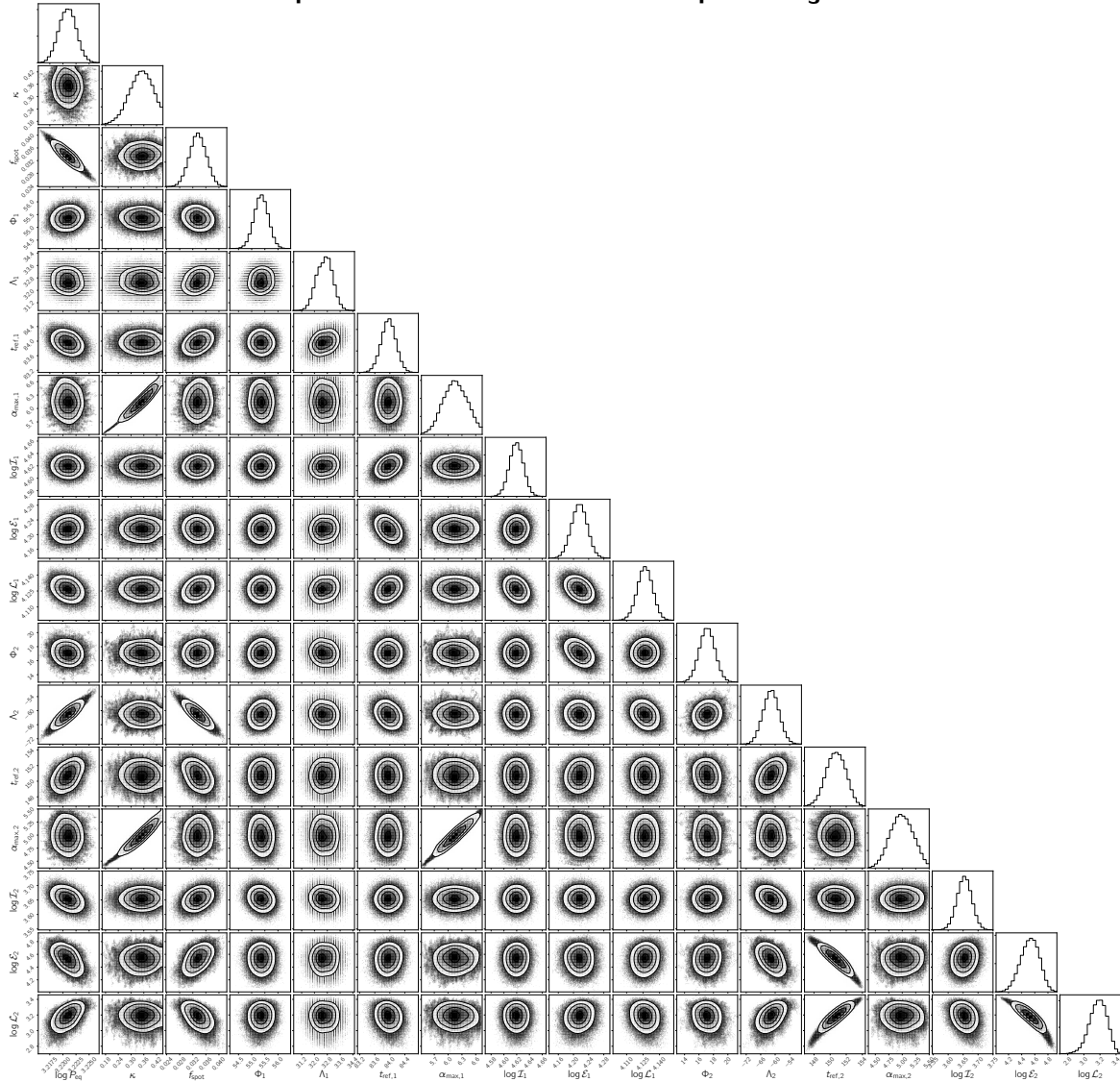
**Two-spot model for One-spot-like light curve**



Figure A.5: Same as Figure A.4 but for the two-spot model.

Figure A.6: Same as Figure A.4 but for the two-spot model with fixed sin $i$.